

Date : 29 September

HST-GOALS: The Nature of Optically-Luminous Stellar Clusters in Nearby Cluster-Rich Luminous Infrared Galaxies

T. Vavilkin¹, A. S. Evans^{2,1}, J. M. Mazzarella³, J. A. Surace⁴, D.-C. Kim⁵, J. H. Howell⁴,
L. Armus⁴, the GOALS team

ABSTRACT

High-resolution ($\sim 0.1''$), wide-field ($202'' \times 202''$) *Hubble Space Telescope* (HST) ACS/WFC observations of a sample of 15 most cluster-rich Luminous Infrared Galaxies (LIRGs: $L_{\text{IR}}[8 - 1000\mu\text{m}] \geq 10^{11} L_{\odot}$) from the Great Observatory All-sky LIRG Survey (GOALS) sample are presented. These observations, obtained at both $0.4\mu\text{m}$ (F435W) and $0.9\mu\text{m}$ (F814W), have made it possible to assess the nature of luminous optically-visible star clusters and star cluster complexes in a large sample of nearby ($z < 0.035$), high luminosity starburst galaxies. Over 7000 luminous star cluster were detected in the present LIRGs sample; these LIRGs contain some of the most luminous clusters ($M_{F435W} \approx -17$ mag) observed thus far. A large fraction of cluster population ($\gtrsim 30\%$) is younger than 10 Myr, but also a population with an age distribution up to few hundred Myr is likely present. The range of specific frequencies T_N for star clusters is $0.67 - 1.73$, with the range of values being higher than that observed in nearby spiral galaxies. These optically-visible star clusters contribute about 4% to F435W and 2% to F814W total fluxes. The cluster luminosity function exponents have median values of $\alpha = -1.91 \pm 0.22$ and -1.88 ± 0.20 as measured in

¹Department of Physics & Astronomy, Stony Brook University, Stony Brook, NY, 11794-3800: vavilkin@grad.physics.sunysb.edu; aevans@virginia.edu

² Department of Astronomy, University of Virginia, 530 McCormick Road, Charlottesville, VA 22904 and National Radio Astronomy Observatory, 520 Edgemont Road, Charlottesville, VA 22903

³Infrared Processing and Analysis Center, California Institute of Technology, MS 100-22, Pasadena, CA 91125: mazz@ipac.caltech.edu

⁴Spitzer Science Center, Pasadena, CA 91125: jhhowell@ipac.caltech.edu; jason@ipac.caltech.edu; lee@ipac.caltech.edu

⁵Department of Astronomy, University of Virginia, 530 McCormick Road, Charlottesville, VA 22904

F435W and F814W images, respectively. Autocorrelation functions of the spatial distribution of star clusters were calculated; they exhibit a power-law behavior on scales of 1 kpc with the median index of -0.77 ± 0.13 . ~~The visual impression of early merger stage systems conveys a large degree of “clustering” of star clusters, while in late merger stages clusters are dispersed through-out the galaxy. The visual impression is also confirmed by a difference in median indexes: for early merger stages the median power law index is -0.84 ± 0.07 and the median power-law index for mid-merger and late merger stages is -0.62 ± 0.10 .~~ Ancillary *Spitzer* IRAC and *GALEX* near-UV imaging data are also presented to examine correlations between locations of young optical stellar clusters with PAH and UV emission regions. While near-UV emission traces well the distribution of optically visible clusters, no correlation is found with PAH emission and embedded star formation. Thus, optically visible star clusters and UV emission represent un-obscured star formation which appears to be unassociated with the bulk of the star formation that takes place in dusty central regions of LIRGs. This work is part of the Great Observatories All-sky LIRG Survey (GOALS).



Subject headings: galaxies: active — galaxies: interacting — infrared: galaxies —

1. Introduction

Luminous star clusters are dense aggregations of a few hundred to about a million coeval stars; they have ages of few Myr to 1 Gyr and are gravitationally bound at least at the time of their formation. Some of the densest, most massive star clusters (SC) survive for prolonged time and, being very luminous, can be observed at great distances, providing insights into massive star formation in a wide variety of galaxy types and environments. Star clusters are closely connected to the origin of stellar field population; a large fraction of stars form in clusters, the majority of which dissolve over time, dispersing stars throughout their host galaxies. Star clusters also reveal star formation histories of galaxies and shed light on star formation processes in mergers since star and cluster formation is most intense during mergers and dynamical interactions. Finally, SCs are interesting in their own right as fundamental building blocks of galaxies, and studies of SCs provide an understanding of the physical processes involved in their formation and dynamical evolution.

Luminous star clusters are found in a wide variety of environments: normal spiral galaxies (Larsen & Richtler 1999), dwarf starburst galaxies (Adamo et al. 2011), nuclear star bursts, barred galaxies, tidal tails (Knierman et al. 2003) and most notably in merging

and starburst galaxies (e.g., Whitmore & Schweizer 1995; Surace et al. 1998). The present *HST* study is an investigation of the properties of optically luminous star clusters in the latter of these classes of galaxies, specifically the Luminous Infrared Galaxies (LIRGs: i.e., $L_{\text{IR}} \geq 10^{11} L_{\odot}$), which are observed to be interacting or merging spiral galaxies which derive their high infrared luminosities through varying contributions of star formation and activity galactic nuclei (AGN) emission reprocessed by dust. As will be seen, although LIRGs are, by definition, very dusty systems in which most of the light is enshrouded in dust, these *HST* observations show LIRGs to be very rich in optically-visible star clusters. In the process of analyzing the optical properties of these galaxies using traditional metrics, the *HST* data will also be compared with *GALEX* ultraviolet and *Spitzer* $8\mu\text{m}$ imaging data to assess the correlation of optically-luminous clusters with both unextinguished and extinguished (i.e., embedded star formation) emission in each of these LIRGs.

This paper is organized as follows: the sample selection criteria are described in §2, observations and data reduction are presented in §3, detection algorithm is described in §4, results are reported in §5, the analysis and discussion is in §6, section §7 is the summary.

The cosmology adopted throughout this paper is consistent with Armus et al. (2009). The systemic heliocentric recession velocities were corrected according to the flow model of Mould et al. (2000a, b) that accounts for the three major attractors in the local universe (Virgo supercluster, Great Attractor, Shapley Supercluster) (3-attractor flow model) and adopting $H_0 = 70 \text{ km s}^{-1} \text{ Mpc}^{-1}$, $\Omega_{\text{M}} = 0.28$, and $\Omega_{\Lambda} = 0.72$ based on the five-year WMAP results (Hinshaw et al. 2009), as provided by the NASA/IPAC Extragalactic Database (NED).

2. Sample Selection

The present sample of LIRGs is selected from the *HST* optical survey (Evans et al., in prep.) of a complete sample of 87 $L_{\text{IR}} > 10^{11.4} L_{\odot}$ LIRGs in the Great Observatories All-Sky LIRG Survey (GOALS; Armus et al. 2009). GOALS consists of all LIRGs in the flux limited (i.e., $f_{60\mu\text{m}} > 5.24 \text{ Jy}$) *IRAS* Revised Bright Galaxy Sample (RBGS; Sanders et al. 2003), and contains 202 objects with $L_{\text{IR}} \geq 10^{11} L_{\odot}$ out to a maximum redshift of $z = 0.088$ (median $z = 0.008$). The LIRGs imaged at F435W and F814W with *HST* exhibit a wealth of point-like luminous sources associated with galaxies – these are luminous star clusters and cluster associations. Using the detection procedure described in §4.1, we have extracted SC in the complete sample of all 87 galaxies imaged with *HST*.

The primary goal of the present paper is to study the nature of luminous star clusters

in a large sample of LIRGs. To achieve this, the following are required: (i) The LIRGs in the sample must contain a sufficient number of clusters visible per galaxy to build up robust statistics and (ii) the LIRGs must be at a low enough redshift to allow for comparisons to be made between the spatial distribution of the detected clusters and the lower resolution *GALEX* near-UV and *Spitzer* mid-IR images. As a result, the selection criteria are naturally biased towards relatively nearby, well-resolved LIRGs with large angular size. The sample selection was chosen as follows:



The distribution of the number of star clusters per system (i.e. galaxy pairs were counted as one system) is shown in the histogram in Figure 1. Three LIRGs (NGC 3256, NGC 3690, NGC 5257) are absent from this histogram due to very large (>800) number of clusters. The first and highest bin of the histogram contains 19 galaxies ($\approx 22\%$ of the complete HST-GOALS sample) with less than 20 clusters. The distribution falls off gradually until the 120 – 140 bin and rises slightly again in consequent bins. This second “peak”, comprised of systems with 140 – 220 detected clusters, and a tail with systems containing > 220 clusters constitute the cluster-rich LIRGs sample that is the focus of this article (20 systems $\approx 23\%$ of the HST-GOALS sample).

In Figure 2, the number of clusters per system is plotted versus redshift for the GOALS *HST* sample. The systems in the cluster-rich sample are designated with triangle symbols and are located in the upper left corner (> 150 and $z < 0.033$). There is a moderate correlation (Spearman rank correlation coefficient $r_s = -0.60$ with significance 7.2×10^{-10}) between the number of SCs and the redshift of the galaxy. This is expected due to the decreasing metric resolution and the decreasing sensitivity to faint cluster detection as a function of increasing redshift.



A presence of a “break” at ~ 140 clusters in both figures reflects a transition in appearance of galaxies; i.e., from large, well resolved galaxies to smaller and mostly more distant galaxies with less details. For this reason, we choose a limit of 140 clusters as the main selection criterion for the sample. While this criterion only selects a small fraction of the total *HST* GOALS sample, it allows for a more robust statistical analysis of the optically-visible cluster population in each galaxy. This criterion also naturally limits the redshift range of the systems in a manner that allows detailed morphological analysis and multi-wavelength comparisons. Specifically, the redshift range of this sample is $0.009 \leq z \leq 0.034$ (NGC 3256 being the closest and VV 340 the most distant), corresponding to a luminosity distance range of $D_L \sim 38.9 \text{ Mpc} - 157 \text{ Mpc}$ and a median redshift of $z = 0.02$ (85.5 Mpc). The analysis of SC in the complete GOALS *HST* sample will be presented in a follow-up paper.



For LIRGs comprised of two or more galaxies, at least one of the galaxies has to fulfill the selection criterion of more than 140 clusters. Two systems, NGC 5331 and CGCG 448-

020, have more than 140 clusters in total, but the individual galaxies contain less than 100 clusters. Three LIRGs, NGC 6240, IC 4686/7/9 and IRAS 20351+2521 that also fulfill the selection criterion (175, 243 and 174 clusters, respectively) are located in a crowded star field (i.e. $\sim 20\%$ of detected clusters could be foreground Galactic stars, see §4.3), and therefore are not included in this analysis.

The resultant sample of 15 LIRGs analyzed in the present paper is presented in Table 1. For LIRGs containing two or more distinct galaxies, the galaxies have been individually tabulated. Of the present sample, six LIRGs are galaxy pairs, resulting in a total of 21 individual galaxies. Two galaxies within a galaxy pair, VV340a and NGC 7674A, contain too few clusters, 14 and 0, respectively, therefore cluster analysis is performed only on 19 galaxies.

Note that a cluster analysis of NGC 2623 and IC 883 have been presented previous publications, i.e., Evans et al. (2008) and Modica et al. (2011), respectively.

3. Observations and Data Reduction

3.1. Observations

The *HST* observations of 15 LIRGs in this paper were obtained as part of an imaging campaign of a complete sample of 88 GOALS LIRGs with $L_{\text{IR}} > 10^{11.4} L_{\odot}$ (PID #10592, PI A. Evans). The galaxies were imaged with the Advanced Camera for Surveys (ACS) Wide Field Channel (WFC). The large field of view of the Wide Field Channel ($202'' \times 202''$) allows the extended tidal features and galaxies pairs to be imaged at high resolution of $\sim 0.1''$. One galaxy was observed per orbit in the ACCUM mode with three 420 sec integrations in F435W filter and two 360 sec integrations in F814W filter using the LINE dither pattern. The observations are summarized in Table 2.

3.2. Data Reduction

The data products available from the Multimission Archive at STScI (MAST) were initially reduced using the standard STScI calibration pipeline that removes instrumental signatures, subtracts dark image, performs flat-fielding, removes cosmic rays when combining associated images, removes geometric distortion and calibrates the images. Due to the small number of exposures, the cosmic ray removal in the standard STScI pipeline was ineffective; a significant number of cosmic ray-affected pixels remained. The visible bias level offsets

between the four quadrants of the images presented an additional concern.

In order to address these issues, the following steps were taken:

- 1) Our reprocessing begins with the FLT files downloaded from the *HST* archive. The FLT files are the dark image subtracted, flat-fielded, calibrated individual exposures that are the end product of the CALACS package of the STScI pipeline.
- 2) As a first step to removing cosmic rays, the routine `lacos_im` (van Dokkum 2001) was executed on the FLT files. This algorithm uses the Laplacian edge detection method to identify cosmic rays due to the sharpness of their edges. The routine is more effective on non-drizzled images, since drizzling smooths the edges. Pixels adjacent to cosmic rays were also flagged in order to remove residual halos. All the flagged pixels were replaced with a median value calculated in a 10×10 pixel box surrounding the flagged pixel.
- 3) In order to remove bias level offsets between the four quadrants of an image, the sky was estimated and subtracted separately for each quadrant.
- 4) The reprocessed individual exposure files were then passed on to the MULTIDRIZZLE task (Koekemoer et al. 2002; Fruchter & Hook 2002) in PyRAF/STSDAS package that removes geometric distortion and combines the dithered individual exposures into a final calibrated image. The same set of parameters as in STScI pipeline was used, except that no sky subtraction was performed (see step 3).
- 5) Further cosmic ray removal was performed with `jerrej2.cl` task in IRAF as described in Rhoads (2000). This routine convolves the image with a spatial filter consisting of a Gaussian (approximating the point spread function) minus a delta function. Strongly negative pixels in the convolved image are flagged as cosmic ray hits. The few remaining cosmic rays were removed by eye using `imedit` in IRAF.
- 6) As the final step, the *HST* images were rotated such that North is up and East left, F435W and F814W images aligned, and the 2MASS catalogue positions of several bright stars in each LIRG field were used to apply WCS corrections to each image. The typical WCS correction was about $1''$ and the resultant average astrometric precision is $0.1''$.

4. Cluster Detection Procedure

4.1. Detection

The detection of star clusters was performed on images prior to rotation (before step 6 in §3.2) in order to eliminate possible effects of rotation on counts in pixels and thus on photometry.


Due to the large FOV of ACS, the images cover not only the entire galaxy and its


extended features, but also contain a good deal of foreground stars and background galaxies. The foreground stars are used to create a PSF model, make precise WCS corrections (§3.2) and to determine the expected percentage of contamination of foreground stars to the number of detected clusters (§4.3).


The large FOV makes it also a necessary first step to mask the portion of the image over which the galaxy subtends and the cluster detection will be performed. Masks were created to outline the galaxy to ~ 24.5 mag/arcsec² surface brightness in the F814W images. This is approximately the surface brightness level that can be traced “by eye” and encloses essentially all of the visible galaxy features.

Masks were created by first median smoothing the F814W image using 40×40 pixels box (in order to remove small-scale features), then by boxcar smoothing (50×50 pixels box). The IRAF routine IMREPLACE was used to set pixel values below the chosen cut-off to 0 (i.e., the sky portion of the image) and above to 1 (the galaxy). The few remaining bright stars outside of the galaxy were removed by hand with IRAF imedit. The mask image was then multiplied by the science image, leaving only the galaxy area above 0. For each galaxy, the F814W mask was applied to both the F435W and F814W science images.

Once the masks were applied, the routine Source Extractor (Bertin & Arnouts 1996) was executed to identify potential clusters in each image. The parameters for SExtractor were set rather generously in order to find as many candidate sources as possible. Source Extractor was also used to fit and subtract the non-uniform background, i.e. the underlying galaxy (see §4.2). Weight maps created by MultiDrizzle were also used for detection purposes.

All sources detected with SExtractor were passed on to IDL routines to apply a set of selection criteria. To be deemed viable, a cluster candidate had to (i) be detected in both F435W and F814W  (ii) have full width at half the maximum intensity, FWHM, in the range of 1.7 – 4 pixels and (iii) have a signal-to-noise, S/N, greater than 5.

Centroids of the SExtractor positions were computed with IDL procedure CNTRD. The FWHM of each candidate was calculated with procedure RADPROF that fits a Gaussian in a 5×5 pixel box. While the objects with high S/N have FWHM of about 2-3 pixels, the FWHM of low S/N objects exhibit a lot of scatter. The range of FWHM between 1.7 and 4 includes also faint sources that appear point-like while  excluding fuzzy extended sources.

An example of the detected clusters is shown in  Figure 3. The left panel shows the original F435W image. In the right panel, the underlying galaxy is subtracted and clusters are marked with circles. The images were inspected by eye to ensure that the detected sources were indeed point-like and located within the galaxy. Obvious stars and galaxy nuclei were removed.

4.2. Cluster and Galaxy Photometry

Accurate cluster photometry is complicated by the non-uniform light distribution of the underlying galaxy. Source Extractor was used to map and subtract the background (i.e., the underlying galaxy) by computing a bi-cubic-spline interpolation over background values estimated in a 9×9 pixel grid. The mesh size was chosen to be large enough not to be affected by clusters but small enough to reproduce the small scale variations of the underlying galaxy. Such a mesh size did an efficient job of removing the galaxy and minimizing the creation of holes surrounding clusters during the extraction. In order to minimize the flux contribution from clusters to the galaxy map, detected clusters were masked out before fitting the background with SExtractor.

Cluster photometry was performed with the IDL routine APER in a $0.3''$ (6 pixels) diameter aperture after the underlying galaxy was subtracted by Source Extractor. Sky uncertainty was measured in an annulus $0.25'' - 0.5''$ (5 - 10 pixels) and used to calculate signal-to-noise and photometric uncertainty for clusters. Aperture corrections, applied to each cluster, were determined for each image by following the procedure outlined in Sirianni et al. (2005). Bright stars in each image were used to create a PSF and to calculate the fraction of encircled flux in a $0.15''$ radius aperture as compared to $0.5''$ aperture. The derived aperture corrections are in good agreement with the measured values listed in Table 3 of Sirianni et al. (2005). Since the FWHM of high S/N clusters are comparable or only marginally larger than the ACS PSF (~ 2 pixels, depending on the filter), all clusters were treated as unresolved and PSF aperture corrections were uniformly applied. Even in two of the nearest galaxies (NGC 3256 and NGC 3690), clusters are only very slightly resolved and the above procedure for aperture corrections produces less than 0.1 mag difference.

All magnitudes are in VEGAMAG magnitude system – ACS/WFC zero points are 25.793 mag for F435W and 25.536 mag for F814W filter¹. Absolute magnitudes and colors of the clusters were calculated taking into account the effect of foreground Galactic extinction (see Table 2) using the values calculated following Schlegel et al. (1998) and provided by the NASA/IPAC Extragalactic Database (NED).

The accuracy of our photometric measurements was tested while assessing the efficiency of detection algorithm (see §4.4). Artificial stars of known magnitudes were added to the image, and the detection procedure and photometry measurements were performed and compared to the original values. For clusters brighter than an apparent magnitude of 25, the average photometric error was determined to be less than 0.10 magnitudes.

¹For revised ACS zero-points posted on 2009 May 19 see <http://www.stsci.edu/hst/acs/analysis/zeropoints>

To measure total fluxes of each galaxy, the masks described in §4.1 were used. The flux inside the mask was calculated. The background level was measured outside of the masked galaxy and its contribution was subtracted. The flux of foreground stars, present inside the masked region in several galaxies, was also measured and subtracted. Photometric uncertainties were calculated taking into account the error from the count rate and sky variance.

4.3. Contamination by Foreground Stars

Foreground galactic stars and distant galaxies are present throughout the ACS images. In order to account for the level of contamination, the assumption was made that foreground stars in each magnitude range are evenly distributed throughout each ACS/WFC image. Thus, one can account for the contamination along the line-of-sight to the galaxy by measuring the magnitudes of objects in the “sky portion” of each image. To this end, the cluster detection procedure (§4.1) was applied to the sky portion of each image. The number of detected sources per magnitude bin was then normalized by the ratio of the image area covered by the galaxy and the sky. For this sample, the degree of contamination is between 3% and 10% with a median of 6%.

4.4. Completeness

The efficiency of the detection algorithm was tested using IRAF ADDSTAR routine. This routine adds artificial stars to the image with uniform distribution in positions and magnitudes. The apparent magnitude range was chosen between 18 and 27 mag, and a PSF created from bright stars in the image was used. In order to avoid overcrowding, the number of artificial stars added to the image did not exceed 10% of the detected clusters (only 10% of the number of detected objects was added to the image). The detection procedure described in §4.1 and photometry (§4.2) were then performed on the images with added stars, and the number and magnitudes of recovered objects were recorded. This procedure was repeated 100 times per galaxy in order to build up good statistics. A completeness function, i.e. the fraction of recovered objects as a function of apparent magnitude, was calculated for each galaxy; an example of the completeness function is shown in Figure 4. The cluster detection for F435W and F814W images is found to be complete at the 50% level at apparent magnitudes of ~ 25.5 and ~ 25.0 , respectively.

The images were not subdivided into areas with different surface brightness / background

levels, as is sometimes done for nearby, large galaxies like NGC 4038/4039 (e.g., Whitmore et al. 1999). Since artificial stars were distributed randomly, and the detection of artificial stars was performed over the same area of the image as cluster detection, the completeness function reflects the overall cluster detection efficiency in a given galaxy, and will therefore be appropriate for all but the relatively small regions of very high background.

5. Results

5.1. Optical Galaxy Morphology and Photometry

As stated in §2, the 15 LIRG systems discussed in this paper consist of 21 individual galaxies, 19 of which contain a sufficient number of clusters to meet the selection criteria. Host galaxy photometry in F435W and F814W filters was measured following the procedure outlined in §4.2, and the results are listed in Table 3.2. The absolute magnitudes range between -19.62 mag to -21.79 mag in the F435W filter and -21.56 mag to -23.40 mag in F814W, with median values of -21.20 mag and -22.76 mag, respectively. The optically brightest galaxy in this sample is NGC 0695.

Figure 5 shows the ACS/WFC F435W images of the sample; the galaxies are arranged in an approximate merger stage sequence. It should be noted that an exact order is difficult to establish. The sample encompasses objects in different interaction stages: from an apparently undisturbed disk of NGC 0695, through widely separated galaxy pairs with either intact disks (VV 340, NGC 7674, NGC 6786 / UGC 11415) or asymmetric disks and tidal tails (NGC 7469, NGC 5257/8, Arp 256), to systems with two distinguishable bodies in a common envelope (NGC 3690, IC 1623) and advanced mergers with disturbed morphology and long prominent tails (IC 0883, NGC 1614, NGC 2623, NGC 3256, NGC 0034, Arp 220). In this article, VV 340, NGC 7674, NGC 6786, NGC 7469, NGC 5257, Arp 256 are referred to as early merger stage systems; NGC 3690, IC 1623, IC 0883, NGC 1614, NGC 2623 are mid-merger stage systems; and NGC 3256, NGC 0034, Arp 220 are late merger stage systems. The early merger stage systems in this sample are dominated by face-on spirals, the mid-merger stage systems have irregular amorphous bodies and long tails, while the late merger stage systems have somewhat more regular and symmetrical appearance but still display clear signs of a merger event.

The infrared luminosity of LIRGs in this sample is $L_{\text{IR}} = 10^{11.48-12.28} L_{\odot}$, with ARP 256 being the least luminous LIRG and ARP 220 being the most luminous. The median luminous of the sample is $L_{\text{IR}} = 10^{11.65} L_{\odot}$. The sample includes only one ultraluminous infrared galaxy (ULIRG: defined as $L_{\text{IR}} \geq 10^{12} L_{\odot}$), ARP 220; other ULIRGs in GOALS

sample have fewer detected clusters due to their large distance. In four galaxy pairs (VV340, NGC 7674, NGC 7469, ARP 256), most of the IR flux is attributed to only one galaxy. In the case of VV340 and ARP 256, the IR bright galaxy contains less detected clusters than the companion. In NGC 6786 and NGC 5257, the IR fluxes are approximately equally divided between both galaxies (see also Mazzarella et al. 2011).

5.2. Cluster Properties

5.2.1. Number of Clusters

The number of detected clusters per galaxy shows a variation of an order of magnitude, between ~ 150 and ~ 1700 , with the median of 296 (Table 4, Column 2). In NGC 3256 and NGC 3690, the closest galaxies in the sample, the number of clusters exceeds by far the rest of the sample.

The number of detected clusters may not reflect the intrinsic cluster population of a galaxy. Several observational factors such as distance, angular size of the galaxy, orientation and possibly the amount of dust obscuration affect our ability to detect SC. For obvious reasons, the number of detected clusters strongly depends on the distance of a galaxy (see also §2, Figure 2). The lower limit on the cluster number as selection criterion favors nearby well-resolved galaxies with large angular size. The median angular size (measured in masks described in §4.1) of LIRG systems in this sample is about double the size of the other systems in the HST-GOALS sample: $\sim 1 \text{ arcmin}^2$ versus $\sim 0.4 \text{ arcmin}^2$ (median of the complete HST-GOALS sample, excluding the 15 cluster-rich systems). Orientation affects angular size and extinction, with face-on galaxies having larger sizes and also less dust obscuration, therefore most galaxies in the sample are viewed face-on. The amount of dust obscuration seems also important, for example in the highly reddened ULIRG ARP 220 relatively few clusters are detected.

There is no straight-forward correlation between the number of clusters and the merger stage, L_{IR} or optical magnitude of the galaxy.

5.2.2. Luminosity Distribution

Figures 6 and 7 show the distribution of absolute F435W and F814W magnitudes of clusters in each LIRG. The absolute magnitudes of detected clusters range typically between about -8 and -16 magnitudes in both the F435W and F814W filters.

The faint end of the brightness distribution is a consequence of the detection limit of the algorithm and the distance of the sample. Given the redshift range $0.009 \leq z \leq 0.034$, the distance modulus is $32.95 \leq (m-M) \leq 35.98$ magnitudes with a median $(m-M)_{\text{med}} = 35.07$ magnitudes. At the detection limit of ~ 26 apparent magnitudes, the absolute magnitudes of clusters are expected to be limited to about -7 and -9 magnitudes, which is in good agreement with the measurements. The decrease of cluster counts at the faint end of the brightness distribution is caused by the decreased efficiency of detection algorithm; when corrected for, as best as possible, with the completeness function (§6.4), the distribution keeps rising.

The most luminous clusters are found in NGC 7469 ($M_{\text{F435W}} = -17.0$ mag) in a circum-nuclear ring and NGC 6786 ($M_{\text{F435W}} = -16.7$ mag) in a spiral arm close to the nucleus. The least luminous clusters are found in ARP 220; the brightness cluster member in ARP 220 has an absolute magnitude of $M_{\text{F435W}} = -12.2$ mag. The magnitudes of brightest cluster in each galaxy is listed in Table 5. Particular care was taken to remove galactic nuclei and obvious stars. Although stars posing as bright clusters cannot be completely excluded, all bright clusters have colors $(m_{\text{F435W}} - m_{\text{F814W}}) < 1.5$, consistent with them being young clusters. The largest number of bright ($M_{\text{F435W}} < -12$ mag) clusters is found in NGC 0695, and they constitute 35% of the complete cluster population in this galaxy. ARP 220 has the least number of bright clusters, only 0.5% of its cluster population are $M_{\text{F435W}} < -12$ magnitude.

In galaxies in early merger stages (i.e., the face-on spirals NGC 0695, NGC 5257, Arp 256, NGC 7674) bright clusters are located in spiral arms in high surface brightness regions and are often grouped in star cluster complexes. In mid-merger stages (NGC 3690, IC 1623) SCs are also located in high surface brightness regions. In late mergers stages (NGC 0034, IC 0883, NGC 2623) bright clusters are found dispersed through-out the main body of the galaxy.

5.2.3. Cluster Colors

Figure 8 shows histograms of the number of clusters versus the $(\text{F435W} - \text{F814W})$ colors of clusters. The cluster colors are in the range $-0.5 < (\text{F435W} - \text{F814W}) < 3$ mag with the highest bin between 0.5 to 1 mag. Clusters with $(\text{F435W} - \text{F814W}) > 2.0$ are either heavily extinguished or foreground stars (see §6.5).

A median $(\text{F435W} - \text{F814W})$ color of all clusters in each galaxy was calculated; the color range is between 0.43 and 1.13 mag; the values are listed in Table 4. The galaxies with

the reddest median cluster color are ARP 220 and IC 5283 , while ARP 256 and IC 1623 have the most blue median cluster colors. The median cluster color for the entire sample is 0.72 ± 0.19 mag.

6. Analysis and Discussion

6.1. Specific Frequency

In order to compare the richness of cluster population of a galaxy, it is useful to have a quantity that relates the number of clusters with the luminosity of the galaxy. For old globular clusters specific frequency is defined as

$$S_N = N_{cl} \times 10^{0.4(M_V+15)} \quad (1)$$

(Harris & van den Bergh 1981), with N_{cl} total number of globular clusters and M_V absolute visual magnitude of the galaxy. Unlike old globular clusters that have a Gaussian distribution and therefore a well defined total number of clusters, young clusters have an exponential distribution and the number of clusters counted in a galaxy depends on the sensitivity/detection limit. Larsen & Richtler (1999) define T_N , a quantity equivalent to specific frequency S_N , for young clusters

$$T_N = N_{cl} \times 10^{0.4(M_B+15)}, \quad (2)$$

where M_B is the B-band absolute magnitude and N_{cl} is the number of young clusters above a certain limiting magnitude. Following this definition, we calculate T_N of young clusters in our sample, limiting to clusters brighter than -9 mag in F435W. The F435W filter matches closely the Johnson B-band; an absolute magnitude of $M_{F435W} = -9$ mag corresponds roughly to the 50% completeness and is also a brightness threshold for individual stars. If the completeness correction is applied to the number of clusters (see §4.4), the resultant corrected T_N values are as listed in Table 4. The errors were calculated using the Poisson statistics of cluster counts and photometric errors in galaxy magnitudes.

The distribution of T_N values is shown in Figure 9. The T_N values range between 0.67 in NGC 0034 and 1.73 in NGC 3690 with a median of 1.14 ± 0.30 . The highest bin is 1.0 - 1.2 and contains 5 galaxies (= 25%). While the number of clusters in NGC 3256 (~ 1700) exceeds the other galaxies in the sample by almost a factor of 10, the T_N of 1.30 is just slightly above the median of the sample.



Table 1 of Larsen & Richtler (2000) lists T_N values for a sample of 21 nearby spiral galaxies. While the limiting magnitude is somewhat comparable to ours ($M_V < -8.5$ and $M_V < -9.5$ for “red” and “blue” population of clusters) Larsen & Richtler (2000) use ground based observations that cover only the central parts of the galaxies and the number of clusters was not corrected for completeness. The highest T_N value in Larsen & Richtler (2000) sample is 1.77 (NGC 5236) and is consistent with the highest value of 1.73 (NGC 3690) in the present sample. The median T_N value in Larsen & Richtler (2000) is 0.45 ± 0.53 and is smaller than in our sample (1.14 ± 0.30). While 60% of galaxies in Larsen & Richtler (2000) sample have T_N values less than 0.5, all galaxies in our sample have values above 0.5. Even keeping in mind the shortcomings of the comparison, it appears that the specific frequency T_N is enhanced in this sample of LIRGs as compared to local spirals.

Elliptical galaxies have much higher specific frequency S_N of old globular clusters; i.e., in the range of $S_N \sim 2 - 6$ (Harris 1991, Elmegreen 1999) as compared to spiral galaxies ($T_N < 1$). Schweizer (1987) and Ashman & Zepf (1992) suggest that a large number of SC forms during a merger process of two gas-rich disk galaxies that will lead to a high S_N elliptical galaxy. The T_N values for young clusters discussed in this section cannot be compared directly to S_N of old globular clusters for various reasons: the majority of young clusters may disperse with time, and additional clusters may continuously be forming during the merger process. Further, the M_V of the galaxy will change with time due to fading of the underlying stellar population with age. Although merging LIRGs show higher T_N values as compared to local spirals, the infant mortality of young clusters is very high, roughly 80 - 90% are expected to dissolve each logarithmic decade of time, meaning that only about 1 in 1,000 clusters with mass greater than $10^4 M_\odot$ will survive to become an old globular cluster (Whitmore 2004). As T_N values at the present stage suggest, more clusters need to be formed in order to account for high S_N of an elliptical galaxy .

6.2. Specific Luminosity

Specific luminosity T_L , a measure of the percentage of flux contributed by clusters, is written in the form

$$T_L = 100 \times \frac{L_{clusters}}{L_{Galaxy}}, \quad (3)$$

(Harris 1991 ; Larsen & Richter 2000), where $L_{clusters}$ is the total luminosity of clusters and L_{Galaxy} the total luminosity of the galaxy.

The specific luminosity is independent of the distance modulus. It is also relatively insensitive to incompleteness at the faint end of cluster luminosity distribution because most of the cluster flux originates from a handful of the brightest clusters. On average, only the brightest 12% of SCs in the entire SC population are responsible for 80% of F435W flux from clusters, with the two extremes being observed in NGC 7469 (the brightest 1.7% of SCs) and Arp 220 (the brightest 52% of SCs).

The specific luminosities are listed in Table 4. Errors were calculated by taking into account uncertainties in both cluster and galaxy photometry. The contribution of visible clusters to total flux in F435W filter varies between 0.5% (ARP 220) and 7.3% (NGC 7469), with a median of $3.4 \pm 2.0\%$. For the F814W images these numbers are 0.3% (ARP 220) to 3.5% (IC 1623), with a median of $1.9 \pm 0.9\%$. ARP 220 has the least contribution of flux from clusters, possibly due to high amount of dust extinction. The specific luminosity distribution for F435W and F814W is plotted in Figure 10. The histogram of $T_L(\text{F435W})$, specific luminosity T_L for F435W images, shows a rather uniform distribution with a small peak in 3-4% bin, while the $T_L(\text{F814W})$ values have a smaller range and peak in 1-2% bin.

Table 1 of Larsen & Richtler (2000) lists T_L values for U and V filters for nearby spiral galaxies and starburst/mergers. Our T_L values are significantly higher than Larsen & Richtler (2000) values for spiral galaxies (median for U is 0.5 and for V is 0.3) and are in starburst/merger galaxies range.

Larsen & Richtler (2000) find an upward trend of specific luminosity $T_L(\text{U})$ with SFR calculated using FIR *IRAS* fluxes and a correlation between $T_L(\text{U})$ and Σ_{SFR} (SFR per unit area) for nearby spiral galaxies. Figure 11 shows a plot of the specific luminosity $T_L(\text{F435W})$ versus SFRs calculated in Howell et al. (2010) using *IRAS* FIR and *GALEX* FUV fluxes (SFR total, panel a)) and *GALEX* FUV fluxes only (SFR UV, panel b)). The $T_L(\text{F435W})$ versus Σ_{SFR} (SFR per unit area) for respective SFRs is plotted in Figure 12. Panel a) in both figures shows no clear trends, the Spearman rank correlation coefficients are $r_s = 0.18$ with significance 0.5 and $r_s = -0.19$ with significance 0.4 for SFR total and Σ_{SFR} total, respectively. Panel b) exhibits an upward trend in $T_L(\text{F435W})$ with increasing SFR UV (Spearman rank correlation coefficient $r_s = 0.70$ with significance 8.1×10^{-4}) and Σ_{SFR} UV (Spearman rank correlation coefficient $r_s = 0.56$ with significance 1.2×10^{-2}). Unlike in Larsen & Richtler (2000), the scatter in the plotted data does not decrease when using Σ_{SFR} instead of SFR. A possible source of scatter in $T_L(\text{F435W})$ versus SFR or Σ_{SFR} plots are uncertainties in the estimation of SFRs due to the AGN contribution.

Larsen & Richtler (2000) list $T_L(\text{U})$ and $T_L(\text{V})$ values, thus in order to compare Larsen & Richtler (2000) T_L values with $T_L(\text{F435W})$ values of the cluster-rich LIRGs sample, an extrapolation to $T_L(\text{B})$ values is needed. The galaxy magnitudes were calculated using

B–V galaxy colors listed in Table 2 of Larsen & Richtler (2000) and the SC magnitudes were extrapolated assuming a mean cluster color of B–V= 0.2. Although this estimate is somewhat crude, it nevertheless allows a direct comparison presented in Figure 13. The $T_L(B)$ data points for nearby normal spiral galaxies from Larsen & Richtler (2000) are designated with triangles, and the $T_L(F435W)$ values of the cluster-rich sample are points. The two populations are disconnected; the Larsen & Richtler (2000) sample has lower SFRs and shows an upward trend, while the cluster-rich LIRGs sample has higher SFR values but no trend emerges.

The present LIRGs sample, unlike the Larsen & Richtler (2000) nearby spiral galaxies sample, does not exhibit a correlation between $T_L(F435W)$ and SFR or Σ_{SFR} derived from FIR fluxes. In LIRGs, the IR luminosity that is used to derive SFR originates for the most part in the nuclear region and not in the extended main body of the galaxy where SCs are located. Instead, a trend of $T_L(F435W)$ with SFR or Σ_{SFR} derived using FUV fluxes emerges. FUV emission arises from young, massive, un-obscured stars, the same type of SF that is traced by young SCs (see §6.8 and §6.9).

6.3. Brightest Clusters

Table 5 lists the absolute F435W magnitudes, the (F435W–F814W) colors, ages and masses of the most luminous cluster found in each galaxy. The age and the mass of the cluster were derived following the method described in §6.5. Eleven clusters have (F435W–F814W) < 0.5 resulting in ages younger than 7.6 Myr. Seven clusters have $0.5 < (F435W-F814W) < 1.0$ and one cluster (F435W–F814W)= 1.36, they suffer from a color-age degeneracy, and the smallest masses and consequently youngest ages were assumed in this analysis. No correction for extinction was performed due to difficulties in determining the extinction to each SC, as described in §6.6. The brightest clusters are young, with ages varying between 4.8 Myr and 8.3 Myr with a median of 7.6 Myr. The masses of brightest clusters vary between $1.1 \times 10^5 M_\odot$ and $5.8 \times 10^6 M_\odot$, with a median of $1.5 \times 10^6 M_\odot$. The ages are upper limits and the masses are lower limit estimates due to unknown extinction.

The present LIRGs sample contains some of the most luminous clusters observed so far. As described in §5.2.2, NGC 7469 ($M_{F435W} = -17.1$ mag) and NGC 6786 ($M_{F435W} = -16.7$ mag) harbor the brightest clusters in our sample; the median of the sample is $M_{F435W} = -15.4$ mag. For comparison, the brightest individual cluster in the Local Group, 30 Dor/R136 in the Large Magellanic Cloud, has $M_V = -11.1$ mag (Hunter et al. 1995), and W3 in NGC 7252 (Schweizer & Seitzer 1998) has $M_V = -16.2$ mag. Luminosities of clusters in the present sample are comparable to ones found in a sample of warm ULIRGs (Surace et al. 1998).



Surace et al. (1998) speculate that the brightest clusters in their ULIRG sample could be in fact cluster associations. Although the bright clusters in the present sample appear as unresolved, point-like and symmetric sources, the resolution of the *HST* observations correspond to size scales of 19 – 71 pc. Given that cluster associations can have sizes as small as 20 pc, the possibility that the brightest clusters are indeed cluster associations cannot be ruled out. Alternatively, since the majority of bright clusters are located in areas with high surface brightness (e.g., nuclear regions) there may be flux contributions from the underlying galaxy.

Several authors (Whitmore 2003; Larsen 2002b; Weidner et al. 2004; Bastian 2008) have investigated the correlation between the brightest young cluster and the SFR of its host galaxy. Figure 1 in Bastian (2008) shows a plot of V-band luminosity of the brightest cluster versus $\log(\text{SFR})$ with an apparent linear relation over several magnitudes of SFR, from individual star-forming regions to ULIRGs. An analogous plot including the present sample is shown in Figure 14. The F435W magnitude values were used since, according to Bruzual & Charlot (2003) evolutionary models, $B - V \approx 0$ for clusters in this age range. The SFRs are derived using *IRAS* IR and *GALEX* UV fluxes (Howell et al. 2010), see also §6.2). The galaxies from Larsen (2002b) sample are designated with triangles, the squares mark data from Bastian (2008) Table 1. Four LIRGs (NGC 2623, NGC 3256, NGC 6240 and IRAS 19155–2124) in Bastian (2008) Table 1 are also present in the GOALS sample and are excluded or replaced with our values. The cluster-rich LIRGs are indicated with star symbols. The straight line is the fit derived by Weidner et al. (2004) using the sample of spiral and dwarf galaxies observed by Larsen (2002a,b), i.e.,

$$M_V = -1.87(\pm 0.06) \times \log(\text{SFR}) - 12.14(\pm 0.07), \quad (4)$$

(i.e., Equation 2 of Weidner et al. (2004)). The brightest clusters in the cluster-rich LIRGs sample follow the correlation and are located at the high end of luminosities and SFRs. The amount of scatter is within the range of previous datasets and the outliers may be due to extinction (points below the line) and/or uncertainties in SFR estimation (e.g. as a result of AGN contribution). The outlier IC 5283 illustrates the effects of extinction - the brightest cluster in IC 5283 has an estimated age of 807 Myr, which is significantly higher than the estimated ages of less than 10 Myr for the brightest SC in the rest of the sample. If an extinction of $A_V = 1$ mag is adopted for this SC, the age estimate would change to 7.6 Myr (median age of the sample), $M_{F435W} = -13.7$ mag ($\Delta B = 1.4$ mag) and shift the location in the V-band luminosity versus SFR very close to the best-fit line. In the case of Arp 220, the cluster with the brightest measured F435W magnitude is the one plotted in the Figure. However, the fourth brightest F435W cluster is the brightest in F814W filter and is

estimated to have the extinction of $E(B-V)=1.48$ (Wilson et al. 2006); this corresponds to an $A_V = 4.4$ mag. If this magnitude is extinction corrected, the resulting $M_V = -16.48$ mag, making it the brightest cluster overall. It should also be noted that although the M_V are similar to Wilson et al. (2006), our SFR is larger by $\sim 90 M_\odot \text{ yr}^{-1}$ and Arp 220 still falls below the line.

The brightest cluster – SFR correlation can be explained by the size-of-sample effect (Whitmore 2003; Bastian 2008). A galaxy with higher SFR forms more young clusters and consequently is able to sample the cluster mass function to higher masses. Given the high SFRs of LIRGs in the present sample, it is not surprising to find that they harbor some of the most luminous clusters. Another important requirement for a brightest cluster – SFR correlation is that the brightest cluster has to be young in order to correlate with the present SFR. Bastian (2008) concludes that the youngest clusters (< 10 Myr) are predominantly the brightest, which is consistent with our findings.



6.4. Luminosity Function

Figures 15 and 16 show histograms of the cluster luminosity distribution as measured in the F435W and F814W images; luminosity functions (LF) have been fitted to each histogram. The data are presented in 0.5 mag bins, the width of the bin is large enough that photometric uncertainties should have little effect on the form of the distribution. The red histograms represent the raw, uncorrected luminosity distribution, the black histograms are corrected for foreground stars contamination and for the efficiency of the detection algorithm. The number of foreground Galactic stars expected in each luminosity bin was estimated using the procedure described in §4.3 and subtracted from the number of clusters in each respective magnitude bin. A correction for the efficiency of the detection algorithm was made by dividing the histograms by the completeness functions determined in §4.4. The histograms were not reddening corrected due to difficulties in determining the extinction (see §6.6).

The cluster luminosity function is a power law of the form

$$dN(L_i)/dL_i = \beta L_i^\alpha, \quad (5)$$

where L_i is the luminosity of the cluster in a filter i . In $\log - \log$ space, the power law becomes a liner relation

$$\log N(L_i) = aM_i + b, \quad (6)$$

with the variable a being related to the luminosity function index α as

$$\alpha = -(2.5a + 1) \quad (7)$$

(Larsen 2002b).

The linear relation was fitted to each histogram using the least squares fit weighted by the square root of the number of clusters in the bin. The range of the fit was limited to the magnitude bins in which at least which half of artificial stars were identified (§4.4); this limit is indicated in Figures 15 and 16 by an arrow.

Values of the LF indices α are listed in Table 6. They range from -1.5 to -2.3 with a median of -1.91 ± 0.21 and -1.88 ± 0.20 in the F435W and F814W images, respectively. Corrections for foreground stars and completeness have only a minor effect on LF indices; on average the slope becomes ~ 0.09 steeper. A fit to the raw luminosity histograms performed to the 80% completeness level (the highest uncorrected bin), results in median values of -1.81 ± 0.21 in F435W and -1.71 ± 0.26 in the F435W and F814W images, respectively.

The corrected luminosity histograms show no turn-over seen in the distribution of old globular clusters, although only NGC 3256 and NGC 3690 probe the LF beyond the peak magnitude of $M_I = -8.5$ mag (see e.g., Kundu & Whitmore (2001) for a discussion of globular cluster luminosity functions).

The LF for young clusters has been studied in numerous galaxies and galaxy types, and the index $\alpha \sim -2$ (Portegies Zwart et al. (2010) and references therein) is a representative value. Schweizer & Seitzer (2007) derive the LF index of -1.75 ± 0.10 for NGC 0034 in V band, which is in excellent agreement with our values of -1.70 ± 0.3 . Zepf et al. (1999) find a LF index of ~ -1.8 in NGC 3256, which is again in good agreement with our values of -1.84 ± 0.17 (F435W) and -1.91 ± 0.15 (F814W). LF index values for the present sample are somewhat lower than the generally accepted LF index $\alpha \approx -2$. Possible sources of uncertainties in our LF index estimates are extinction and blending of individual clusters into cluster associations due to limited resolution; both make the slope of the LF shallower. It is also possible that the completeness corrections have been underestimated since a single completeness function was calculated for the entire galaxy, without a sub-division into several surface brightness areas (§4.4). Therefore, our derived LF index values are lower limits.

6.5. Cluster Ages

Figures 17 and 18 show color-magnitude diagrams of absolute F435W magnitudes plotted versus (F435W – F814W) color of SCs. Evolutionary tracks computed using Bruzual-Charlot population synthesis models (Bruzual & Charlot 2003) for an instantaneous starburst with solar metallicity are plotted for cluster masses of $10^5 M_{\odot}$ and $10^6 M_{\odot}$. In the lower right panel, an evolutionary track for a cluster of mass $10^4 M_{\odot}$ is also shown; the arrow in the right upper corner represents 1 magnitude of visual extinction.

The evolutionary tracks in Figures 17 and 18 originate from GALAXEV (version 2003), a library of evolutionary stellar population synthesis models that were computed using the isochrone synthesis code of Bruzual & Charlot (2003). This code computes the spectral evolution of a stellar population based on a stellar evolution prescription (Padova 1994) and a library of observed stellar spectra (STELIB). The tracks in Figures 17 and 18 are for the case of an instantaneous starburst, solar metallicity and Salpeter IMF. The output of the model (spectral energy distribution) was convolved with the ACS F435W and F814W filter response functions in order to obtain magnitudes and colors in these filters and scaled with the mass of a cluster. The age and mass estimation using color-magnitude diagrams together with evolutionary tracks suffers from two major shortcomings (i) **color-age degeneracy** and (ii) unknown extinction that varies from cluster to cluster.

(i) Color-age degeneracy. Figure 19 shows the evolution of (F435W–F814W) color of a cluster as the cluster ages. The shape of the evolutionary track exhibits a color-age degeneracy for ages between 7.6 Myr to 500 Myr and colors $0.51 < (F435W-F814W) < 0.98$. A color value in this range can be attributed to at least three different ages. This degeneracy persists in color-magnitude diagrams; without a knowledge of cluster mass, the proper evolutionary track cannot be assigned to individual clusters and the absolute magnitude cannot break the degeneracy. A combination of younger age and smaller mass produces the same color and absolute magnitude as an older and more massive cluster. A $10^5 M_{\odot}$ cluster with an age of 10^7 years has the same M_{F435W} and (F435W–F814W) as a $10^6 M_{\odot}$ cluster with an age of $\text{few} \times 10^8$ years (see bottom right panel in Figure 17).

(ii) Extinction-age degeneracy. The extinction vector for M_{F435W} magnitude and (F435W – F814W) color is parallel to evolutionary tracks, therefore the effects of reddening by dust cannot be distinguished from aging. Unfortunately, imaging in only two bands makes it impossible to get a good estimate of extinction. Certainly, all clusters suffer some amount of extinction, which also varies from cluster to cluster. In particular, extinction has a strong effect on age estimates of clusters with (F435W – F814W) > 1.0, located to the right of the evolutionary tracks. Even a moderate amount of extinction of $A_V=1$ can make a cluster appear ~ 800 Myr older, as in the case of the brightest cluster in IC 5283 (§6.3). Given these shortcom-

ings, ages and masses were determined only for clusters with $(F435W - F814W) < 0.51$, corresponding to the age of 7.6 Myr. The ages are upper limits and masses are lower limits since we do not attempt to correct for extinction.

While the unknown extinction and masses of clusters prevent an accurate determination of the ages of the majority of SCs, clusters with $(F435W - F814W) < 0.51$ are not subjected to color-age degeneracy and are sufficiently blue that they cannot suffer a significant amount of extinction, and thus limits can be placed on their ages and masses. Clusters can be as young as 1.5 Myr (NGC 3690, NGC 5257, NGC 6786, NGC 7674), and the median age for the young clusters in this LIRGs sample is ~ 6.9 Myr. It should be emphasized that ages are upper limits, while the masses are lower limits, since no attempt was made to correct for extinction. Clearly, some amount of extinction is present. In particular, young SCs are assumed to be embedded in dust that is present in the star-forming region. Although the dust might clear in as little as a few Myr (Larsen 2010), $0.5 < A_V < 2.5$ mag extinction is found for 0–4 Myr old clusters (Whitmore & Zhang 2002; Reines et al. 2008). On the other hand, given the blueness of clusters with $(F435W - F814W) < 0.51$, the extinction cannot be larger than $A_V = 1$ mag.

Table 6 lists the percentage of SCs with $(F435W - F814W) < 0.51$. The percentage of these young clusters is highest in Arp 256 NED02 (57%) and lowest in Arp 220 (7%) with a median of $\sim 30\%$. The available data make it difficult to determine if a larger percentage of young clusters in a galaxy is due to a younger cluster population or due to less extinction.

For clusters with $0.51 < (F435W - F814W) < 0.98$ the color-age degeneracy and unknown masses make an age estimate difficult. It would be reasonable to assume that some distribution of masses and ages is present; in which case the age range could span from a few Myrs to a few hundred Myrs. For example, Whitmore et al. (2010) find in the Antennae a similar range of cluster ages.






Clusters with $(F435W - F814W) > 1.0$ have either ages above 500 Myr or are much younger clusters affected by a moderate amount of extinction. Several clusters have very red colors indicating possible ages above 1 Gyr and hence could be old globular clusters. However, objects with $(F435W - F814W) > 1.5$ and $M_{F435W} < -9.5$ mag cannot be old globular clusters (assuming the upper mass limit of globular clusters of $10^6 M_\odot$) and have to be either foreground Galactic stars or highly extinguished clusters. The same argument applies to objects that lie outside of the color range of the evolutionary models. Most galaxies in the present sample have several clusters in this region of the color-magnitude diagram, but only NGC 3256 and NGC 3690 have a significant percentage of cluster population in this range. The observed extremely red colors can be produced even by a moderate amount of extinction of $A_V=2$.

It is certain that young massive un-extinguished clusters with ages less than 7.6 Myr are present and make up a large fraction of cluster population ($\sim 30\%$) in this sample of LIRGs. A population of heavily extinguished clusters is present as well. An age distribution with a range of a few Myr to a few hundred Myr as seen in the Antennae is likely. Imaging with additional filters or spectroscopy are needed to further constrain the cluster ages.

6.6. Extinction

The extinction affecting SCs, once corrected for foreground reddening as discussed in §4.2, can be either due to dust associated with the local star-forming region where a cluster formed, or due to the wider dust distribution within the host galaxy. The dust surrounding the birthplace of a cluster is cleared within a few Myr (see review by Larsen (2010)). Therefore the dust in the galactic environment is likely responsible for the majority of extinction. In the case of LIRGs it is of particular concern, since these galaxies contain large amounts of dust obscuring their nuclear regions, resulting in their high IR luminosities.

Figure 21 shows the location of star clusters overlaid on (F435W–F814W) images. The grey-scale displays the (F435W–F814W) color of the galaxy with darker shades corresponding to larger (F435W–F814W) values and redder color and lighter shades to smaller (F435W–F814W) values and bluer color. Cluster symbols are color-coded indicating the color and hence a combination of the ages and reddening of clusters. SCs designated with blue dots have (F435W–F814W) < 0.51 . These SCs can be reliably age-dated as being younger than 7.6 Myr. SCs designated with green triangles have (F435W–F814W) = 0.51 – 1.0 and have a wide range of possible ages from 7.6 – 500 Myr. This color bin covers the widest range of cluster ages and therefore contains the largest number of SCs; the peak of the cluster color histograms is within this bin (see §5.2.3). SCs designated with yellow squares have (F435W–F814W) = 1.0 – 1.5 and ages between 500 Myr and 1 Gyr. SCs designated with red stars have (F435W–F814W) > 1.5 and ages older than 1 Gyr. These could be either globular clusters, highly reddened young clusters or foreground Galactic stars.




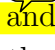
The inspection of Figure 21 shows that clusters are found predominantly in galaxy regions with relatively blue (F435W–F814W) colors. In early merger stages SCs are located predominantly in spiral arms, in what appears to be high surface brightness high cluster density regions. The spiral arms  accompanied by dark dust lanes containing relatively few SCs.  In general, it appears that  colors of clusters found in red dusty regions are  redder than other clusters. Figure 20  supports the assumption that the red cluster colors are due to extinction rather than age-related. This figure shows the ratio (percentage) of clusters found in “red” regions of the galaxy (i.e., redder than the median galaxy color) to


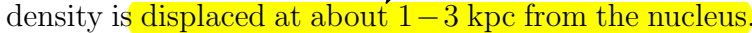
all detected clusters as a function of cluster color. For $(F435W - F814W) > 2$, 80% of the clusters are found in red, highly extinguished galaxy regions.

Imaging in only two filters does not allow a determination of extinction for each cluster. Calzetti et al. (1994) estimate the mean value $E(B-V)=0.45\pm0.22$ mag, corresponding to $A_V=1.3$, in a sample of nearby SB galaxies. For the present LIRGs sample, the extinction is variable – some clusters, located in less dusty galaxy regions, are expected to have only a small amount of extinction. For other clusters, a value of $A_V=2$ seems reasonable.

6.7. Spatial Distribution of Star Clusters

6.7.1. Surface Density Profiles

Figure 22 shows  cluster surface density profiles as a function of distance from the $8\mu\text{m}$ core. The  $8\mu\text{m}$ core is used as the location of the nucleus of each merger component, since it suffers from less dust extinction than the optical *HST* images. The cluster surface density was calculated in circular annuli of 1 kpc width, and only the area within the masks outlining the galaxy (§4.1) was taken into account. The cluster surface density is generally highest near the nucleus of a galaxy and it gradually decreases with distance. Most clusters are found in the main body of a galaxy within 10 kpc. The shape of the cluster surface density profiles can be interpreted by comparing them to optical images (Figure 25) and to grey-scale maps in Figure 27. The surface  density profiles of galaxies in early merger stages (NGC 0695 to Arp 256) appear  jagged and have several peaks that correspond to locations of spiral arms; clusters are predominantly located in spiral arms where the cluster surface density is increased. Galaxies in late merger stages (NGC 3256 - Arp 220) have smooth surface density profiles; clusters are distributed more uniformly through-out the body of the galaxy. Mid-merger stages (NGC 3690 - NGC 2623) have profiles with several peaks that reflect an irregular distribution of large star-forming regions in the galaxy.

For roughly half of the galaxies in the sample (11 out of 19), the maximum cluster surface density coincides with the  nucleus. In the remaining 8 galaxies, the maximum cluster surface density is  displaced at about 1–3 kpc from the nucleus. Four galaxies (VV 340b, NGC 7469, Arp 256 NED02, IC 5283), all of them early stage mergers, have narrow central peaks; in the rest of the sample the central peaks are broader and the cluster surface density values drop to half of their maximum values at ~ 5 kpc. The highest cluster surface density value (20 clusters/kpc²) is found in NGC 3256, which is easily explained by its large number of clusters and proximity. The lowest cluster surface density value is in NGC 7674, which is due to the large linear size of the galaxy and more widespread distribution of clusters.

Six galaxies in this sample have extended tails: NGC 3690, IC 0883, NGC 1614, NGC 2623, NGC 3256 and NGC 0034. The LIRGs NGC 1614 and NGC 2623 have $\sim 20\%$ of their optically-visible cluster population in tails, NGC 3690 and IC 0883 have around $\sim 10\%$ and NGC 0034 and NGC 3256 have less than 1%. NGC 3256 tails are not covered completely by the ACS/WFC images.

6.7.2. Autocorrelation Functions

A more quantitative approach to the characterization of SC distribution was taken by Zhang et al. (2001). They introduced the two-point correlation function in order to investigate the spatial distribution of star clusters and compare them to flux maps in other wavelength bands in NGC 4038/4039, the Antennae galaxies. The two-point correlation function is a well-known technique that has been extensively used to study the large scale galaxy distribution (Peebles 1973, 1980) and can be easily adopted for the two-dimensional discrete distribution of star clusters. The three-dimensional two-point correlation function ξ is defined such that $\bar{n}[1 + \xi(r)]dr^3$ is the probability of finding a neighbor in a volume dr^3 within a distance r from a random object in the sample with the average density of objects \bar{n} . With this, the autocorrelation function for clusters can be defined as

$$1 + \xi(r) = \frac{1}{\bar{n}N} \sum_{i=1}^N n_i(r), \quad (8)$$

where $n_i(r)$ is the number density of clusters found in an aperture of radius r centered on, but excluding cluster i , N is the total number of clusters and \bar{n} is the average number density of clusters. On the right hand side of the equation the mean surface density within radius r from a cluster is divided by the mean surface density of the total sample; therefore $1 + \xi(r)$ is effectively the surface density enhancement within radius r as compared to the average over the whole galaxy. For a random distribution of clusters the auto-correlation function will be flat with $1 + \xi(r) = 1$. For a clustered distribution, $1 + \xi(r) > 1$ and the auto-correlation function will be peaked at small radii. The width of the central peak represents the characteristic spatial scale of association between the clusters. The statistical uncertainty is estimated as $N_p^{-1/2}$ with N_p the number of pairs formed with the central clusters i of the aperture (Peebles 1980; Zhang et al. 2001). In order to estimate the number density $n_i(r)$ of clusters in an aperture centered at cluster i , the area of each aperture was calculated explicitly. Only the area within the masks outlining the galaxy was taken into account.

Figure 23 shows plots of the auto-correlation functions of SCs on a logarithmic scale. The auto-correlation functions peak sharply on small scales with a median FWHM of 0.53 pc. FWHM values show strong correlations with galaxy distance and therefore are largely artifacts of resolution rather than being representative of the true spatial scale of clustering.

The maximum $\xi + 1$ values are between 25 and 13. The $\xi + 1$ axis scaling is somewhat arbitrary. As already mentioned, $\xi + 1$ values are a measure of overdensity within the aperture of radius r as compared to the average density over the whole galaxy \bar{n} . The area of a galaxy is not well-defined and consequently the average density over the galaxy \bar{n} is not well-defined either. In general, an aperture of 10 kpc radius centered on the $8\mu\text{m}$ core was used (except for NGC 7674), since most clusters are found within 10 kpc from the nucleus. There is no correlation with maximum values of Figure 22, e.g. NGC 3256 has the highest peak cluster surface density while the maximum of its auto-correlation function is one of the lowest in the sample. The reason for this is the following: the peak values of cluster surface density reflect the highest density found in a region of a galaxy, while the maximum of the auto-correlation function in Figure 23 reflects the local overdensity measured for all clusters in a galaxy.

Autocorrelation functions have their maxima at small radii and decrease at larger radii. Up to a distance of 1 kpc, the autocorrelation functions in a log-log plot are linear and can be approximated with a power law. Slopes are fit out to a radius of 1 kpc; the resulting power law indices are provided in Table 3.5. The median of the sample is -0.77 ± 0.13 with minimum and maximum values of -0.52 and -0.95 , respectively. These values are in good agreement with values found by Zhang et al. (2001) in the Antennae (-0.83 to -1.06 for cluster populations of different ages) and Scheepmaker et al. (2009) in M51 (-0.8 and -0.7).

In Figure 24, indices of the power law, fitted to the auto-correlation functions, are plotted versus the merger order of the galaxy (as seen in Figure 5). Merger orders 4 – 7 are galaxy pairs and therefore have two data points. The steepest slopes are found in UGC 11415, IC 5283 and Arp 256 NED02 and the shallowest slopes are in NGC 3256 and NGC 3690. A possible trend emerges: early merger stage LIRGs (merger orders 1–7) appear to have steeper slopes and late merger stages (merger orders 8 – 15) shallower slopes. The median auto-correlation function index of galaxies in early merger stages is -0.84 ± 0.07 and the median index of galaxies in late merger stages is -0.62 ± 0.09 . The Mann-Whitney U test shows a statistically significant difference of both means ($p = 5.2 \times 10^{-5}$), and the Kolmogorov-Smirnov test ($p = 2.7 \times 10^{-4}$) confirms that the auto-correlation function indices of galaxies in early and late merger stages were drawn from different populations. A higher power-law index of galaxies in early merger stages indicates a larger degree of “clustering”, while in late merger stages individual clusters are distributed through-out the galaxy. This finding is confirmed also by a visual inspection of the ACS images and cluster surface density profiles.



Clusters in early merger stages are found in spiral arms and giant star-forming regions with a large degree of “clustering”, while in late merger stages clusters are spread out through-out the galaxy.

The two-point auto-correlation function provides some insights into the physical processes of cluster formation. Since SCs form in molecular cloud complexes, the spatial distribution of young star clusters is likely to reflect the structure of the ISM. Zhang et al. (2001) note that the scale of 1 kpc is comparable to the size of giant molecular cloud complexes in the Antennae. The power-law dependency of $\xi + 1$ with radius r is a sign of a hierarchical, self-similar or fractal distribution. The index of a power-law n is related to the fractal dimension $D2$ as $D2 = n + 2$ (Scheepmaker et al. 2009; Mandelbrot 1983). Elmegreen & Elmegreen (2001) showed that the ISM has a fractal dimension of 1.3. The mean power-law index of our sample (-0.77) is in a good agreement. Late merger stages have smaller indexes, possibly indicating that the ISM has a different fractal dimension in late-stage mergers than in spirals, or that clusters have dispersed from their original formation locations.

6.8. Distribution of Flux in near-UV and mid-IR

One of the main benefits of the GOALS data set is the availability of observations at multiple wavelengths (Armus et al. 2009), which makes it possible to compare the properties of star formation traced by the optically visible SCs to star formation traced by *GALEX* near-UV and *Spitzer* mid-IR images. The *GALEX* and *Spitzer* IRAC resolutions ($5.3''$ and $2''$, respectively), although significantly lower than the resolution of *HST*/ACS ($0.1''$), still permit an assessment of the distribution of large-scale star-forming regions as traced at these wavelengths. The details of *GALEX* near-UV and *Spitzer* mid-IR imaging are presented in Howell et al. (2010) and Mazzarella (2011).

Continuum fluxes in the ultraviolet and infrared spectral regions are among the main indicators of star-formation activity and are widely used to estimate star formation rates of galaxies (e.g., Kennicutt 1998). The far- and near-UV trace directly the emission from photospheres of young massive stars. Dust attenuation poses a serious problem since even a moderate amount of dust extinction reduces the UV flux significantly. In the particular case of LIRGs, UV traces on average only $\sim 2.8\%$ of the total SFR (Howell et al. 2010). The IRAC $8\mu\text{m}$ channel is dominated by emission from Polycyclic Aromatic Hydrocarbons (PAH) which are heated by UV photons. In certain cases, the PAH emission can be regarded as a measure of the amount of UV radiation, e.g., actively star-forming regions with uniform metallicity and little contribution from the general radiation field of the galaxy, the $8\mu\text{m}$ emission correlates almost linearly with the SFR (e.g., Figure 3 of Calzetti et al. 2007). The

application of PAHs as a star formation tracer on galactic scales is problematic since the PAH abundance is dependent on metallicity and PAHs are excited by the general radiation field originating from older stars as well. Besides, PAHs are destroyed by harsh UV photon fields in star-forming regions and the emission rather originates in the rims of HII regions (Helou et al. 2004; Bendo 2006). MIPS $24\mu\text{m}$ channel is a good tracer of star formation as well (Calzetti et al. 2005, 2007), but it is not used for this morphology analysis because the $24\mu\text{m}$ images have low resolution and show signatures of the instrumental PSF.

Figure 25 shows the appearance of LIRGs in the cluster-rich sample in four different filters: *GALEX* near-UV ($0.23\mu\text{m}$), *HST*/ACS F435W ($0.4\mu\text{m}$) and F814W ($0.8\mu\text{m}$) and *Spitzer* IRAC $8\mu\text{m}$. The images are in the same merger sequence as Figure 5. The $3.6\mu\text{m}$, $4.5\mu\text{m}$ and $5.8\mu\text{m}$ IRAC images are omitted since their morphology is very similar to the $8\mu\text{m}$ images. The *Spitzer* MIPS $24\mu\text{m}$ emission is not resolved and is omitted as well.

Optical F435W and F814W *HST*/ACS images of our sample show a wide variety of morphologies. These high resolution images reveal an abundance of structures – spiral arms, dust lanes, star-forming regions/complexes and tails. The F435W and F814W images are similar in appearance. The F435W images highlight star-forming regions; dust lanes are prominent as dark patches. The F814W images are less affected by dust and trace light from the older stellar population and the nucleus.

The morphology of *GALEX* near-UV images can be roughly divided into 2 classes: (i) bright nuclear region with knots distributed throughout the lower surface brightness spiral arm emission and (ii) diffuse UV emission similar in extent to optical images with a lack of prominent UV emission from the nucleus. Class (i) encompasses early merger stages VV 340b, NGC 7674, NGC 6786 / UGC 11415, NGC 7469, as well NGC 3690, IC 1623 and NGC 3256. Class (ii) is represented by NGC 0695, NGC 5257/8, Arp 256, IC 0883, NGC 2623 and NGC 0034. In NGC 1614 most UV emission originates from a bright star-forming region, and the nucleus is less prominent. Arp 220 shows very little UV emission.

The IRAC $8\mu\text{m}$ images can be divided into three classes. The first two classes are identical to the UV classes; and class (iii) are systems with an unresolved bright nucleus and almost no extended emission. Class (i), similar to UV images, encompasses early merger stages VV 340b, NGC 7674, NGC 6786 / UGC 11415, Arp 256 NED01 as well as NGC 3690, IC 1623, NGC 1614 and NGC 3256. Class (ii) includes NGC 0695, NGC 5257/8 and Arp 256 NED02. Finally, class (iii) contains predominantly late merger stages NGC 7469, IC 0883, NGC 2623, NGC 0034 and Arp 220.

In general, two clearly different trends as a function of merger stage are observed:

- (1) In the early merger stages, the near-UV and $8\mu\text{m}$ morphology appear similar. The

nuclear regions are bright, and emission from spiral arms is clearly visible.

(2) In the late merger stages, the near-UV and $8\mu\text{m}$ morphologies are very different. The near-UV appears more diffuse and extended, whereas the $8\mu\text{m}$ morphology is more concentrated and originates primarily from the nucleus.

Figure 26 shows (F435W–F814W) images in grey-scale with near-UV and $8\mu\text{m}$ contours overlaid. The (F435W–F814W) images, already used in Figure 21, give a better view of the structure of galaxies such as dust lanes, obscured nuclei (dark shading) and blue star-forming regions (light shading). In early merger stages (mostly face-on spiral galaxies), blue star-forming regions in spiral arms run along dark red dust lanes. In late merger stages the nuclear region is obscured by dust and appears red, and giant star-forming regions stand out in light shading. As expected, in general the near-UV and $8\mu\text{m}$ emission originate in different regions: the UV flux coincides with blue galaxy regions while $8\mu\text{m}$ flux correlates with red, dusty regions. In early merger stages (NGC 0695, VV 340b, NGC 7674 and NGC 6786 / UGC 11415) $8\mu\text{m}$ and UV contours overlap somewhat since both follow the spiral arms. Starting with NGC 7469 the overlap disappears: the maxima of emission are offset, and in some cases are opposite: e.g., in IC 1623 the western galaxy is bright in UV and the eastern nucleus is bright in $8\mu\text{m}$.

These multi-wavelength figures clearly illustrate a scenario in which the star formation within LIRGs occurs throughout spiral arms and nuclear region of the progenitors in the early stages, with dust playing a smaller role in obscuration. As the merger progresses and gas flows inward as the spiral structure is disrupted, the star formation in the nuclear regions is enhanced, and dust has a much stronger affect on obscuring the nuclear starburst at optical and UV wavelengths.

6.9. Distribution of Star Clusters Relative to near-UV and mid-IR Emission

Figure 27 shows in grey-scale the surface density of clusters. The grey-scale maps were created by smoothing an image containing the positions of clusters with a Gaussian filter to match the resolution of the IRAC $8\mu\text{m}$ images. Overlaid on the grey-scale SC surface density are contours of near-UV and $8\mu\text{m}$ emission. In general, the distribution of near-UV emission appears to correlate better with the cluster distribution than the $8\mu\text{m}$ emission. As described in the previous section, the $8\mu\text{m}$ emission in early stage mergers follows roughly the spiral arms tracing the dark dust lanes that run along these spiral arms (e.g., in NGC 7674, NGC 6786 / UGC 11415, NGC 5257/8 and Arp 256). In these cases, there is some degree of overlap between cluster locations and $8\mu\text{m}$ emission contours. For example, in NGC 7674

knots of $8\mu\text{m}$ emission coincide with high cluster density areas as well as spiral arms. With progressing merger stage the images no longer show a clear association between $8\mu\text{m}$ emission and cluster locations. In particular, $8\mu\text{m}$ emission emanates from the nucleus while the SC distribution is extended. In these late merger stage systems, the near-UV emission appears to trace the clusters more effectively than the $8\mu\text{m}$ emission. In some cases the peaks (NGC 3690, IC 1623, IC 0883, NGC 1614) or higher contours (NGC 2623, NGC 3256) of near-UV emission are directly associated with cluster-dense regions.

To test the above visual impression, cross-correlation functions between SC locations and the $8\mu\text{m}$ and near-UV fluxes were calculated. Zhang et al. (2001) define the cross-correlation function between SC locations and flux maps as

$$1 + \xi(r) = \frac{1}{\bar{f}N} \sum_{i=1}^N f_i(r), \quad (9)$$

where $f_i(r)$ is the intensity (i.e. flux per pixel) in an aperture with radius r centered on cluster i , and \bar{f} is the mean intensity over the galaxy. Only the statistical uncertainty due to a finite number of clusters N is taken into account; the uncertainty in flux estimates is neglected, leading to uncertainties of $N^{-1/2}$.

Figure 28 shows the results of the cross-correlation of SC locations with $8\mu\text{m}$ and near-UV fluxes. Some degree of correlation is expected simply due to the fact that both, SCs and flux, are located within the galaxy. As mentioned in §6.7.2, the $\xi + 1$ axis scaling is somewhat arbitrary. In case of cross-correlation functions, $\xi + 1$ values are a measure of flux excess within the aperture of radius r as compared to the average flux \bar{f} over the whole galaxy. In order to compare near-UV and $8\mu\text{m}$ fluxes, the correlation functions were calculated using the same area in both the UV and $8\mu\text{m}$ images, usually $48''$ was sufficient to cover the entire flux of a galaxy.

Correlation functions with near-UV emission (red line) have Gaussian shapes, with a maximum at small radii and decreasing smoothly. The FWHM has a median value of 6.9 kpc; i.e., the near-UV emission traces clusters rather diffusely. The FWHM of the correlation functions show a strong dependence on the distance of the galaxy, which is clearly an effect of resolution.

The $8\mu\text{m}$ correlation functions (black line) have peaks with approximately half the amplitude of the near-UV functions. Further, the profiles are flatter and peak either at small radii or have a maximum at 5–8 kpc. This latter feature is due to the fact that, in many LIRGs, the mid-infrared emission is concentrated in the nuclear region, which is offset from the main location of clusters (e.g., NGC 2623). These offsets primarily occur at late

merger stages, a slightly better correlation for early merger stages can be inferred, as seen also in Figure 27.

The correlation functions confirm the visual impression: near-UV emission is clearly better associated with young SCs than $8\mu\text{m}$ emission. This finding is not surprising: as already mentioned in §6.2 the UV emission arises from young massive un-obscured stars and traces the same type of star formation as the young SCs.

7. Conclusions

The cluster populations of 15 cluster-rich (> 140), nearby ($z < 0.034$) LIRGs from the GOALS sample were investigated. *Hubble Space Telescope* ACS/WFPC images obtained with the F435W and F814W filters were used for cluster detection and photometry. The following conclusions have been reached:

- The overall appearance of host galaxies in optical images shows clear signs of an interaction process. The cluster-rich LIRGs sample contains systems at different interaction stages, from widely separated galaxy pairs to apparent single-nucleus late-stage mergers.
- The number of detected SCs ranges between 150 and 1700 per galaxy, with a median of ~ 300 clusters. The number of detected SCs is affected by the distance to the galaxy, galaxy orientation, and the amount of dust obscuration, and thus may not reflect the intrinsic cluster population of a LIRG.
- The apparent magnitudes of detected SCs in F435W and F814W filters range from 21 to 27 mag, corresponding to the absolute magnitude range of -13 to -9 mag.
- The $(F435W-F814W)$ colors of clusters vary between $-0.5 < (F435W-F814W) < 3$; median $(F435W-F814W)$ colors of a SC population in a galaxy range between 0.43 and 1.13.
- The specific frequency, T_N , (i.e., a measure of the number of clusters per unit host galaxy luminosity) for young clusters, limited to $M_{F435W} < -9$ mag and corrected for completeness, ranges from 0.67 to 1.73 with a median of 1.14 ± 0.30 . The specific frequency is enhanced in this sample of LIRGs as compared to local spirals, which have values in the range of 0.18 to 1.75 with a median of 0.45 ± 0.53 (Larsen & Richtler 2000).

- The specific luminosity, T_L , (i.e. the percentage of flux contributed by clusters to the total flux of the host galaxy) varies between 0.3 and 7.3 with a median 3.4 ± 2.0 in F435W and 1.9 ± 0.9 in F814W images. The relation of T_L with total SFR, found in normal spiral galaxies (Larsen & Richtler 2000) is not valid for LIRGs, but instead a trend of T_L with SFR derived from FUV fluxes is observed.
- The present LIRGs sample contains some of the most luminous clusters observed so far, with brightest clusters having $M_{F435W} \sim -17$ mag. The cluster-rich LIRGs follow well the brightest cluster – SFR correlation observed for lower luminosity star-forming galaxies.
- Power-law indices of completeness-corrected luminosity functions have median values of -1.91 ± 0.21 and -1.88 ± 0.20 for F435W and F814W images, respectively. These values are in good agreement with previously published results for other galaxy samples (e.g., Portegies Zwart et al. (2010) and references therein).
- In order to constrain cluster ages, color-magnitude diagrams ((F435W–F814W) versus M_{F435W}) were constructed and Bruzual-Charlot population synthesis models were plotted for various cluster masses. A significant population of very young un-extinguished SCs that can be reliably age-dated as being younger than 7.6 Myr is present. These clusters comprise $\sim 9\% - 60\%$ of the cluster population, with a median value of $\sim 30\%$. Given the unknown extinction and cluster masses, the ages of cluster population can vary from 5×10^6 years to few 10^8 years. Approximately 80% of the clusters with colors > 2.0 are associated with dust lanes, and thus their colors are likely red primarily due to extinction rather than age.
- Autocorrelation functions of SC locations were calculated and a power-law fit to the inner 1 kpc. The power-law indices vary between -0.52 and -0.95 with a median of -0.77 ± 0.13 . Early merger stage LIRGs have the median auto-correlation function index of -0.84 ± 0.07 and late merger stages have the median index of -0.62 ± 0.09 , indicating a larger degree of “clustering” in early merger stages. SCs in LIRGs in early merger stages are found in spiral arms and giant star-forming regions with a large degree of clustering, while in late merger stages SCs are dispersed throughout the galaxy.
- A comparison of galaxy morphology in near-UV and mid-IR ($8\mu\text{m}$) shows that early stage mergers have similar near-UV and $8\mu\text{m}$ morphologies, with bright nuclear regions and emission from spiral arms. In contrast, late stage mergers have extended and diffuse near-UV emission and compact $8\mu\text{m}$ emission primarily concentrated in the nuclear regions. This is consistent with a scenario in which the star formation within

LIRGs occurs throughout the spiral arms and nuclear regions of the progenitors in the early stages, with dust playing a smaller role in obscuration. As the merger progresses and gas flows inward as the spiral structure is disrupted, the star formation in the nuclear regions is enhanced, and dust has a much stronger effect on obscuring the nuclear starburst.

- Cluster density maps were constructed in order to compare the distribution of optically visible clusters with IR and UV imaging data. The cluster-overdense regions do not coincide well with $8\mu\text{m}$ /PAH emission as traced by *Spitzer* IRAC images but are rather associated with high surface brightness regions in *GALEX* near-UV images. Cross-correlation functions of SC locations with near-UV and $8\mu\text{m}$ fluxes were computed. The correlation coefficients (amplitudes) of the near-UV are about twice as large as $8\mu\text{m}$ coefficients. It is concluded that, in general, the optical star formation is not associated with regions of strong PAH emission and imbedded star formation. This finding is not surprising since un-obscured young SCs are expected to produce a significant amount of UV emission and $8\mu\text{m}$ /PAH emission originates primarily in obscured central regions.
- Optically visible young clusters and UV emission represent un-obscured star formation which appears to be unassociated with the bulk of the star formation that takes place in the dusty central regions of LIRGs.

The authors thank G. Soutchkova and L-H Chien for useful discussions and assistance. TV, ASE and DCK were supported by NSF grant AST 02-06262 and by NASA through grants HST-GO10592.01-A and HST-GO11196.01-A from the SPACE TELESCOPE SCIENCE INSTITUTE, which is operated by the Association of Universities for Research in Astronomy, Inc., under NASA contract NAS5-26555. TV acknowledges support from the IPAC Fellowship Program. This research has made use of the NASA/IPAC Extragalactic Database (NED) which is operated by the Jet Propulsion Laboratory, California Institute of Technology, under contract with the National Aeronautics and Space Administration. This work is based, in part, on observations made with the NASA Galaxy Evolution Explorer. GALEX is operated for NASA by the California Institute of Technology under NASA contract NAS5-98034.

REFERENCES

- Adamo, A., Östlin, G., & Zackrisson, E. 2011, MNRAS, 1488
- Armus, L., Mazzarella, J. M., Evans, A. S., et al. 2009, PASP, 121, 559

- Bastian, N. 2008, MNRAS, 390, 759
- Bendo, G. J. 2006, in Astronomical Society of the Pacific Conference Series, Vol. 357, Astronomical Society of the Pacific Conference Series, ed. L. Armus & W. T. Reach, 192
- Bertin, E. & Arnouts, S. 1996, A&AS, 117, 393
- Bruzual, G. & Charlot, S. 2003, MNRAS, 344, 1000
- Calzetti, D., Kennicutt, R. C., Engelbracht, C. W., et al. 2007, ApJ, 666, 870
- Calzetti, D., Kennicutt, Jr., R. C., Bianchi, L., et al. 2005, ApJ, 633, 871
- Elmegreen, B. G. & Elmegreen, D. M. 2001, AJ, 121, 1507
- Evans, A. S., Vavilkin, T., Pizagno, J., et al. 2008, ApJ, 675, L69
- Fruchter, A. S. & Hook, R. N. 2002, PASP, 114, 144
- Harris, W. E. & van den Bergh, S. 1981, AJ, 86, 1627
- Helou, G., Roussel, H., Appleton, P., et al. 2004, ApJS, 154, 253
- Howell, J. H., Armus, L., Mazzarella, J. M., et al. 2010, ApJ, 715, 572
- Kennicutt, Jr., R. C. 1998, ARA&A, 36, 189
- Knierman, K. A., Gallagher, S. C., Charlton, J. C., et al. 2003, AJ, 126, 1227
- Koekemoer, A. M., Fruchter, A. S., Hook, R. N., & Hack, W. 2002, in The 2002 HST Calibration Workshop : Hubble after the Installation of the ACS and the NICMOS Cooling System, ed. S. Arribas, A. Koekemoer, & B. Whitmore, 337
- Kundu, A. & Whitmore, B. C. 2001, AJ, 121, 2950
- Larsen, S. S. 2002a, in IAU Symposium, Vol. 207, Extragalactic Star Clusters, ed. D. P. Geisler, E. K. Grebel, & D. Minniti, 421
- Larsen, S. S. 2002b, AJ, 124, 1393
- Larsen, S. S. 2010, Royal Society of London Philosophical Transactions Series A, 368, 867
- Larsen, S. S. & Richtler, T. 1999, A&A, 345, 59
- Larsen, S. S. & Richtler, T. 2000, A&A, 354, 836

- Mandelbrot, B. B. 1983, *The Fractal Geometry of Nature* (New York: W. H. Freedman and Co.)
- Peebles, P. J. E. 1973, *ApJ*, 185, 413
- Peebles, P. J. E. 1980, in *Annals of the New York Academy of Sciences*, Vol. 336, Ninth Texas Symposium on Relativistic Astrophysics, ed. J. Ehlers, J. J. Perry, & M. Walker, 161–171
- Portegies Zwart, S. F., McMillan, S. L. W., & Gieles, M. 2010, *ARA&A*, 48, 431
- Reines, A. E., Johnson, K. E., & Goss, W. M. 2008, *AJ*, 135, 2222
- Rhoads, J. E. 2000, *PASP*, 112, 703
- Sanders, D. B., Mazzarella, J. M., Kim, D., Surace, J. A., & Soifer, B. T. 2003, *AJ*, 126, 1607
- Scheepmaker, R. A., Lamers, H. J. G. L. M., Anders, P., & Larsen, S. S. 2009, *A&A*, 494, 81
- Schlegel, D. J., Finkbeiner, D. P., & Davis, M. 1998, *ApJ*, 500, 525
- Schweizer, F. & Seitzer, P. 2007, *AJ*, 133, 2132
- Sirianni, M., Jee, M. J., Benítez, N., et al. 2005, *PASP*, 117, 1049
- Surace, J. A., Sanders, D. B., Vacca, W. D., Veilleux, S., & Mazzarella, J. M. 1998, *ApJ*, 492, 116
- van Dokkum, P. G. 2001, *PASP*, 113, 1420
- Weidner, C., Kroupa, P., & Larsen, S. S. 2004, *MNRAS*, 350, 1503
- Whitmore, B. C. 2003, in *A Decade of Hubble Space Telescope Science*, ed. M. Livio, K. Noll, & M. Stiavelli, 153–178
- Whitmore, B. C. 2004, in *Astronomical Society of the Pacific Conference Series*, Vol. 322, *The Formation and Evolution of Massive Young Star Clusters*, ed. H. J. G. L. M. Lamers, L. J. Smith, & A. Nota, 419
- Whitmore, B. C., Chandar, R., Schweizer, F., et al. 2010, *AJ*, 140, 75
- Whitmore, B. C. & Schweizer, F. 1995, *AJ*, 109, 960

- Whitmore, B. C. & Zhang, Q. 2002, AJ, 124, 1418
- Whitmore, B. C., Zhang, Q., Leitherer, C., et al. 1999, AJ, 118, 1551
- Wilson, C. D., Harris, W. E., Longden, R., & Scoville, N. Z. 2006, ApJ, 641, 763
- Zepf, S. E., Ashman, K. M., English, J., Freeman, K. C., & Sharples, R. M. 1999, AJ, 118, 752
- Zhang, Q., Fall, S. M., & Whitmore, B. C. 2001, ApJ, 561, 727

Table 1. Cluster-Rich LIRGs Sample

Name IRAS	Name Optical ID	R.A. (J2000)	Dec. (J2000)	V_{Helio} (kms^{-1})	D_L (Mpc)	scale (kpc'')	$\log L_{\text{IR}}$ (L_{\odot})
00085-1223	NGC 0034	00h11m06.5s	-12d06m26s	5881	84.1	0.392	11.49
00163-1039	Arp 256						11.48
	Arp 256 NED02	00h18m50.1s	-10d21m42s	8193	118.0	0.540	
	Arp 256 NED01	00h18m50.9s	-10d22m37s	8125	117.0	0.536	
01053-1746	IC 1623	01h07m47.2s	-17d30m25s	6016	85.5	0.399	11.71
01484+2220	NGC 0695	01h51m14.2s	+22d34m57s	9735	139.0	0.634	11.68
04315-0840	NGC 1614	04h33m59.8s	-08d34m44s	4778	67.8	0.319	11.65
08354+2555	NGC 2623	08h38m24.1s	+25d45m17s	5549	84.1	0.393	11.60
10257-4338	NGC 3256	10h27m51.3s	-43d54m14s	2804	38.9	0.185	11.64
11257+5850	NGC 3690	11h28m32.2s	+58d33m44s	3093	50.7	0.242	11.93
13183+3423	IC 0883	13h20m35.3s	+34d08m22s	6985	110.0	0.507	11.73
13373+0105	Arp 240						11.62
	NGC 5258	13h39m57.7s	+00d49m51s	6757	108.0	0.500	
	NGC 5257	13h39m52.9s	+00d50m24s	6798	109.0	0.503	
14547+2449	VV340						11.74
	VV340a	14h54m48.3s	+24d49m03s	10094	157.0	0.710	
	VV340b	14h54m47.9s	+24d48m25s	10029	156.0	0.706	
15327+2340	Arp 220	15h34m57.1s	+23d30m11s	5434	87.9	0.410	12.28
19120+7320	VV 414						11.49
	NGC 6786	19h10m53.9s	+73d24m37s	7500	113.0	0.519	
	UGC 11415	19h11m04.5s	+73d25m36s	7555	113.0	0.522	
23007+0836	Arp 298						11.65
	NGC 7469	23h03m15.6s	+08d52m26s	4892	70.8	0.332	
	IC 5283	23h03m18.0s	+08d53m37s	4804	69.6	0.327	
23254+0830	Arp 182						11.56
	NGC 7674	23h27m56.7s	+08d46m45s	8671	125.0	0.574	
	NGC 7674A	23h27m58.8s	+08d46m58s	8852	128.0	0.585	

Note. — Column 1: Name of the IRAS source. Column 2: Name of the optical source. The systems are separated into individual galaxies/components. Columns 3 and 4: Right Ascension and Declination from NED. Column 5: Heliocentric velocity. Column 6: The luminosity distance in Megaparsecs. Column 7: The total infrared luminosity in \log_{10} Solar units. The redshift dependent values were derived by correcting the heliocentric velocity for the 3-attractor flow model of Mould et al. 2000 and adopting cosmological parameters $H_0 = 70 \text{ km s}^{-1} \text{ Mpc}^{-1}$, $\Omega_M = 0.28$, and $\Omega_V = 0.72$ based on the five-year WMAP results (Hinshaw et al., 2009), as provided by NED. Values are consistent with Armus et al., 2009.

Table 2. Observations

Name	Dataset ^a	Observation Date	Exposure Time (sec)		Extinction	
			F435W	F814W	A_B (mag)	A_I (mag)
NGC 0034	J9CV010*0	2006 Jul 05	1260	720	0.116	0.052
Arp 256	J9CV020*0	2006 May 23	1260	720	0.156	0.070
IC 1623	J9CV040*0	2006 Jul 12	1260	720	0.069	0.031
NGC 0695	J9CV090*0	2005 Aug 23	1260	720	0.388	0.174
NGC 1614	J9CV140*0	2006 Aug 14	1260	720	0.663	0.298
NGC 2623	J9CV250*0	2005 Nov 29	1275	730	0.177	0.080
NGC 3256	J9CV340*0	2005 Nov 06	1320	760	0.524	0.236
NGC 3690	J9CV380*0	2006 Mar 19	1425	830	0.072	0.032
IC 0883	J9CV470*0	2006 Jan 11	1290	740	0.054	0.024
Arp 240	J9CV490*0	2005 Nov 17	1260	720	0.119	0.054
VV 340	J9CV540*0	2006 Jan 07	1260	720	0.183	0.082
Arp 220	J9CV580*0	2005 Dec 21	1260	720	0.219	0.098
VV 414	J9CV710*0	2005 Sep 10	1515	890	0.609	0.274
Arp 298	J9CV810*0	2006 Jun 12	1260	720	0.297	0.134
Arp 182	J9CV850*0	2006 Jun 10	1260	720	0.254	0.114

^a'' is replace by 1 for F435W, 2 for F814W filter

Note. — Column 1: Name of the optical source. Column 2: Name of the dataset in MAST archives. Column 3: Observation date. Columns 4 and 5: Exposure times in F435W and F814W filters. Columns 6 and 7: Foreground Galactic Extinction following Schlegel et al. (1998), available from NED. B band corresponds closely to F435W filter and I band to F814W filter.

Table 3. Host Galaxy Photometry in the Cluster–Rich LIRGs Sample

Name	m_{F435W}	M_{F435W}	m_{F814W}	M_{F814W}	merger stage
NGC 0034	13.91 ± 0.005	-20.83	12.32 ± 0.002	-22.36	late
Arp 256	13.99 ± 0.005	-21.52	12.61 ± 0.003	-22.81	early
Arp 256 NED02	14.73 ± 0.007	-20.77	13.34 ± 0.004	-22.17	
Arp 256 NED01	14.75 ± 0.007	-20.75	13.39 ± 0.004	-22.12	
IC 1623	13.31 ± 0.003	-21.42	12.06 ± 0.002	-22.63	mid
NGC 0695	14.32 ± 0.006	-21.79	12.49 ± 0.003	-23.40	early
NGC 1614	13.69 ± 0.004	-21.13	11.87 ± 0.002	-22.59	mid
NGC 2623	14.29 ± 0.005	-20.51	12.61 ± 0.003	-22.10	mid
NGC 3256	12.22 ± 0.002	-21.25	10.42 ± 0.001	-22.76	late
NGC 3690	12.34 ± 0.002	-21.25	10.77 ± 0.001	-22.79	mid
IC 0883	14.54 ± 0.006	-20.72	12.92 ± 0.003	-22.31	mid
Arp 240	12.86 ± 0.003	-22.44	11.28 ± 0.002	-23.95	early
NGC 5258	13.64 ± 0.004	-21.65	11.97 ± 0.002	-23.27	
NGC 5257	13.58 ± 0.004	-21.71	12.10 ± 0.002	-23.13	
VV340	14.35 ± 0.006	-21.81	12.43 ± 0.003	-23.63	early
VV340a	15.33 ± 0.009	-20.83	13.09 ± 0.004	-22.98	
VV340b	14.96 ± 0.007	-21.21	13.37 ± 0.004	-22.69	
Arp 220	14.08 ± 0.005	-20.86	12.07 ± 0.002	-22.75	late
VV 414	13.72 ± 0.004	-22.15	11.79 ± 0.002	-23.75	early
NGC 6786	14.30 ± 0.005	-21.57	12.47 ± 0.003	-23.07	
UGC 11415	14.67 ± 0.006	-21.20	12.63 ± 0.003	-22.91	
Arp 298	13.09 ± 0.003	-21.46	11.15 ± 0.001	-23.23	early
NGC 7469	13.30 ± 0.003	-21.24	11.41 ± 0.002	-22.98	
IC 5283	14.92 ± 0.007	-19.62	12.82 ± 0.003	-21.56	
Arp 182	13.78 ± 0.004	-21.95	11.99 ± 0.002	-23.61	early
NGC 7674	14.10 ± 0.005	-21.64	12.35 ± 0.003	-23.25	
NGC 7674A	16.05 ± 0.012	-19.69	13.96 ± 0.005	-21.64	

Note. — Column 1: Name of the optical source. Column 2: Apparent F435W magnitude. Column 3: Absolute F435W magnitude calculated using luminosity distance in Table 1. Column 4: Apparent F814W magnitude. Column 5: Absolute F814W magnitude calculated using luminosity distance in Table 1. Column 6: Merger stage

Table 4. Star Cluster Properties in the Cluster–Rich LIRGs Sample I

Name	N _{cl}	(F435W–F814W)	T_N	T_L (F435W)	T_L (F814W)
NGC 0034	182	0.84 ± 0.48	0.674 ± 0.03	2.43 ± 0.04	1.52 ± 0.03
Arp 256	274				
Arp 256 NED02	169	0.43 ± 0.45	1.442 ± 0.10	4.64 ± 0.09	1.86 ± 0.05
Arp 256 NED01	105	0.52 ± 0.46	0.971 ± 0.06	2.72 ± 0.07	1.37 ± 0.05
IC 1623	313	0.57 ± 0.72	0.990 ± 0.04	7.01 ± 0.12	3.54 ± 0.07
NGC 0695	200	1.01 ± 0.57	1.003 ± 0.08	3.80 ± 0.15	2.18 ± 0.09
NGC 1614	374	0.69 ± 0.55	1.191 ± 0.06	3.37 ± 0.09	1.82 ± 0.04
NGC 2623	211	0.72 ± 0.61	0.946 ± 0.04	1.24 ± 0.04	0.69 ± 0.02
NGC 3256	1729	0.90 ± 0.62	1.298 ± 0.03	4.83 ± 0.11	2.80 ± 0.06
NGC 3690	1321	0.66 ± 0.62	1.729 ± 0.05	5.42 ± 0.10	3.17 ± 0.06
IC 0883	164	0.83 ± 0.61	1.187 ± 0.07	3.07 ± 0.04	1.90 ± 0.02
Arp 240	860				
NGC 5258	385	0.88 ± 0.59	1.208 ± 0.07	3.81 ± 0.07	1.95 ± 0.05
NGC 5257	475	0.73 ± 0.56	1.529 ± 0.09	3.88 ± 0.13	1.89 ± 0.07
VV340	202				
VV340a	14				
VV340b	188	0.56 ± 0.50	0.870 ± 0.07	2.53 ± 0.10	1.09 ± 0.06
Arp 220	204	1.13 ± 0.65	0.709 ± 0.03	0.50 ± 0.03	0.33 ± 0.01
VV 414	421				
NGC 6786	293	0.63 ± 0.56	1.137 ± 0.09	6.28 ± 0.12	2.04 ± 0.06
UGC 11415	128	0.73 ± 0.53	0.721 ± 0.05	0.89 ± 0.04	0.37 ± 0.02
Arp 298	414				
NGC 7469	332	0.71 ± 0.64	0.690 ± 0.02	7.31 ± 0.11	2.66 ± 0.07
IC 5283	82	1.12 ± 0.87	1.194 ± 0.05	0.96 ± 0.05	0.66 ± 0.03
Arp 182	299				
NGC 7674	299	0.68 ± 0.50	1.315 ± 0.11	1.70 ± 0.06	0.60 ± 0.03
NGC 7674A	0				

Note. — Column 1 : Name of the optical source. Column 2: Number of detected star clusters. Column 3: Median (F435W–F814W) color of clusters in a galaxy. Column 4: Corrected specific frequency T_N , limited to $M_{F435W} < -9$ and corrected for completeness. Column 5: Specific luminosity T_L in the F435W images. Column 6: Specific luminosity T_L in the F814W images. No analysis was performed for VV 340a and NGC 7674A.

Table 5. Most Luminous Star Clusters in the Cluster-Rich LIRGs Sample

Name	M_{F435W} (mag)	(F435W–F814W) (mag)	Age (Myr)	Mass $\times 10^6 (M_{\odot})$	SFR total ($M_{\odot} \text{yr}^{-1}$)
NGC 0034	-15.15	0.78	7.94	1.33	46.9
Arp 256					
Arp 256 NED02	-15.75	-0.08	5.01	1.74	3.9
Arp 256 NED01	-14.62	0.28	6.61	0.67	48.6
IC 1623	-16.16	-0.17	4.79	2.54	94.1
NGC 0695	-15.18	0.60	7.59	1.26	84.6
NGC 1614	-15.52	0.66	7.94	1.84	78.7
NGC 2623	-14.06	0.91	8.32	0.58	69.2
NGC 3256	-15.85	0.26	6.61	1.96	76.5
NGC 3690	-15.85	0.45	7.24	2.12	150.5
IC 0883	-16.27	0.75	7.94	3.53	94.2
Arp 240					
NGC 5258	-16.22	0.92	8.32	3.77	36.0
NGC 5257	-15.35	0.50	7.59	1.46	35.7
VV340					
VV340a					
VV340b	-14.78	0.15	5.75	0.70	17.6
Arp 220	-12.24	0.73	7.94	0.11	327.7
VV 414					
NGC 6786	-16.67	-0.14	5.01	3.94	143.2
UGC 11415	-14.75	0.50	7.59	0.86	54.5
Arp 298					
NGC 7469	-17.09	0.27	6.61	5.83	66.7
IC 5283	-12.30	1.36	807.24	0.24	10.7
Arp 182					
NGC 7674	-14.41	0.05	5.25	0.52	61.3
NGC 7674A					

Note. — Column 1: Name of the optical source. Column 2: Absolute F435W magnitude of the most luminous cluster. Columns 3: (F435W–F814W) color of the most luminous cluster. Columns 4 and 5: Age and mass for the respective age according to Bruzual & Charlot 2003 evolutionary models. Column 6: SFR derived from *IRAS* FIR and *GALEX* FUV fluxes (Howell et al., 2010).

Table 6. Star Cluster Properties in the Cluster-Rich LIRGs Sample II

Name	Luminosity Function Index $\alpha(\text{F435W})$	Luminosity Function Index $\alpha(\text{F814W})$	Percentage SCs younger 7.6 Myr	Autocorrelation index
NGC 0034	-1.70 ± 0.28	-1.70 ± 0.26	9.9	-0.69 ± 0.18
Arp 256				
Arp 256 NED02	-1.81 ± 0.21	-1.78 ± 0.34	56.8	-0.92 ± 0.25
Arp 256 NED01	-1.76 ± 0.22	-1.72 ± 0.24	48.6	-0.84 ± 0.33
IC 1623	-1.54 ± 0.20	-1.50 ± 0.20	44.7	-0.77 ± 0.10
NGC 0695	-1.65 ± 0.20	-1.72 ± 0.23	18.0	-0.77 ± 0.18
NGC 1614	-1.82 ± 0.27	-1.75 ± 0.25	30.7	-0.65 ± 0.07
NGC 2623	-2.12 ± 0.27	-2.16 ± 0.24	25.1	-0.77 ± 0.15
NGC 3256	-1.84 ± 0.17	-1.91 ± 0.15	17.1	-0.52 ± 0.03
NGC 3690	-1.80 ± 0.16	-1.76 ± 0.15	38.3	-0.54 ± 0.03
IC 0883	-2.17 ± 0.22	-2.01 ± 0.21	17.1	-0.59 ± 0.29
Arp 240				
NGC 5258	-1.91 ± 0.30	-1.88 ± 0.29	16.6	-0.84 ± 0.15
NGC 5257	-1.96 ± 0.29	-1.97 ± 0.28	29.5	-0.77 ± 0.12
VV340				
VV340a				
VV340b	-1.93 ± 0.26	-1.97 ± 0.21	44.1	-0.89 ± 0.38
Arp 220	-2.27 ± 0.30	-2.15 ± 0.27	6.9	-0.56 ± 0.24
VV 414				
NGC 6786	-1.81 ± 0.29	-1.78 ± 0.30	37.9	-0.75 ± 0.15
UGC 11415	-2.27 ± 0.30	-1.94 ± 0.36	27.3	-0.94 ± 0.26
Arp 298				
NGC 7469	-1.98 ± 0.39	-2.02 ± 0.33	31.9	-0.77 ± 0.11
IC 5283	-2.16 ± 0.29	-1.54 ± 0.27	15.9	-0.95 ± 0.15
Arp 182				
NGC 7674	-2.20 ± 0.30	-2.22 ± 0.20	37.8	-0.84 ± 0.20
NGC 7674A				

Note. — Column 1: Name of the optical source. Columns 2 and 3: Luminosity function index α for F435W and F814W images. Column 4: Percentage of cluster population that can be reliably age-dated as younger than 7.6 Myr with no extinction correction. Column 5: Autocorrelation function index.

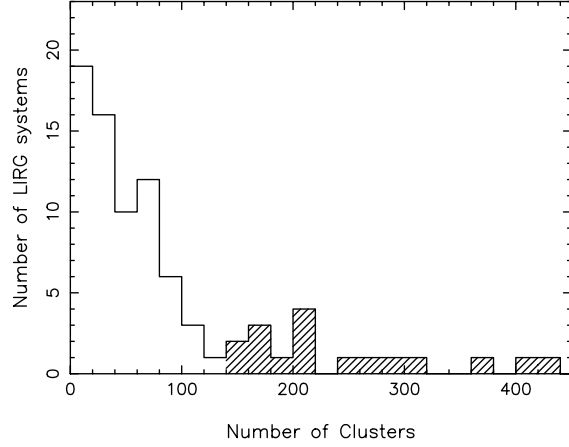


Figure 1: The distribution of the number of SCs per LIRG system (i.e. galaxy pairs count as one system). Three LIRGs (NGC 3256, NGC 3690 and NGC 5257) are absent from this histogram due to a very large (>800) number of SCs. The shaded portion of the histogram constitutes the cluster-rich LIRGs sample.

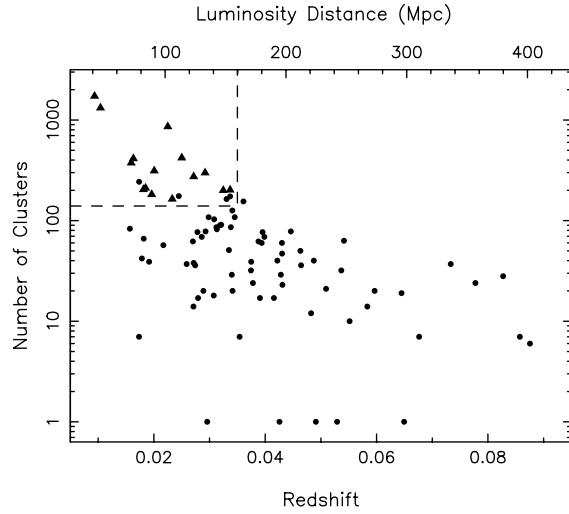


Figure 2: Number of detected SCs versus luminosity distance. The system in the cluster-rich LIRGs sample are denoted with triangles. The horizontal dashed lines indicates the number of clusters selection criterion, the vertical dashed line indicates the resulting luminosity distance range.

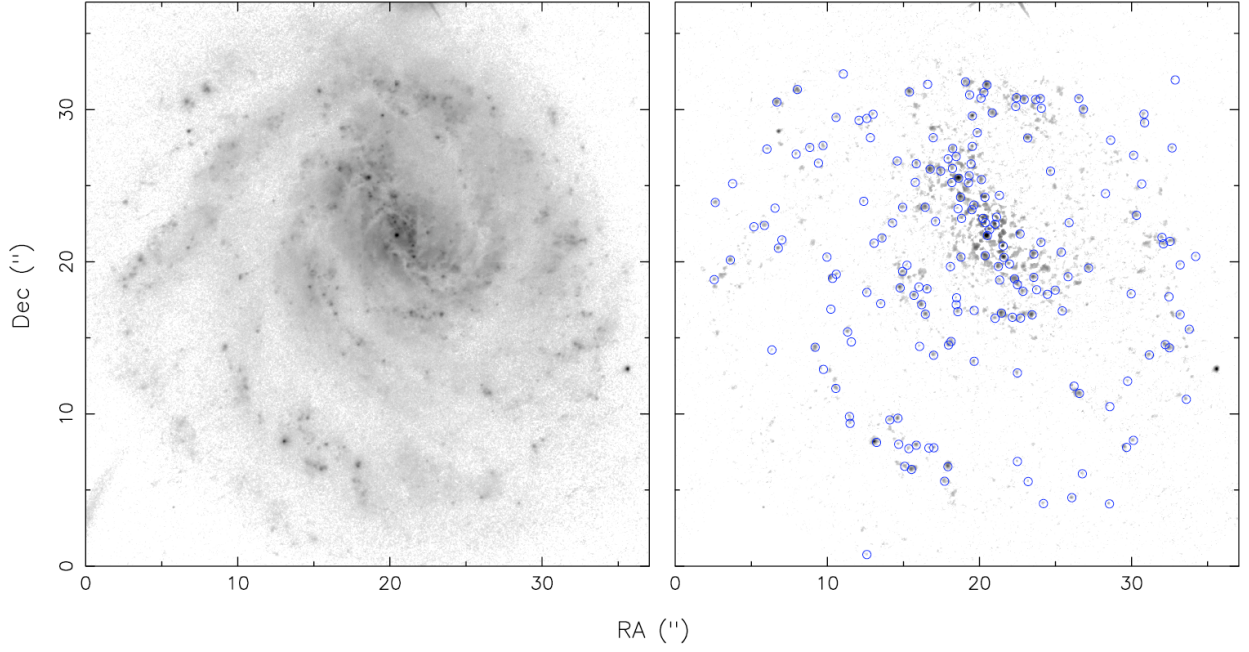


Figure 3: *HST*/ACS F435W images of VV 340b. (a) The original image of the galaxy. (b) The image of the galaxy after the underlying galaxy has been subtracted by SExtractor; identified clusters are designated with blue circles.

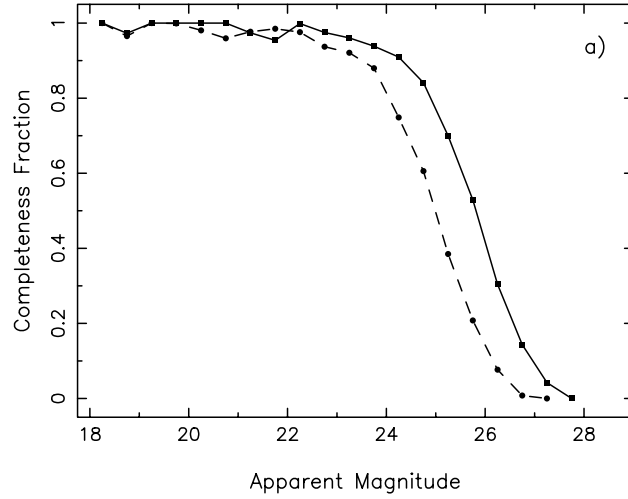


Figure 4: Star cluster detections completeness functions for NGC 0034 in the F435W filter (solid line) and the F814W filter (dashed line).

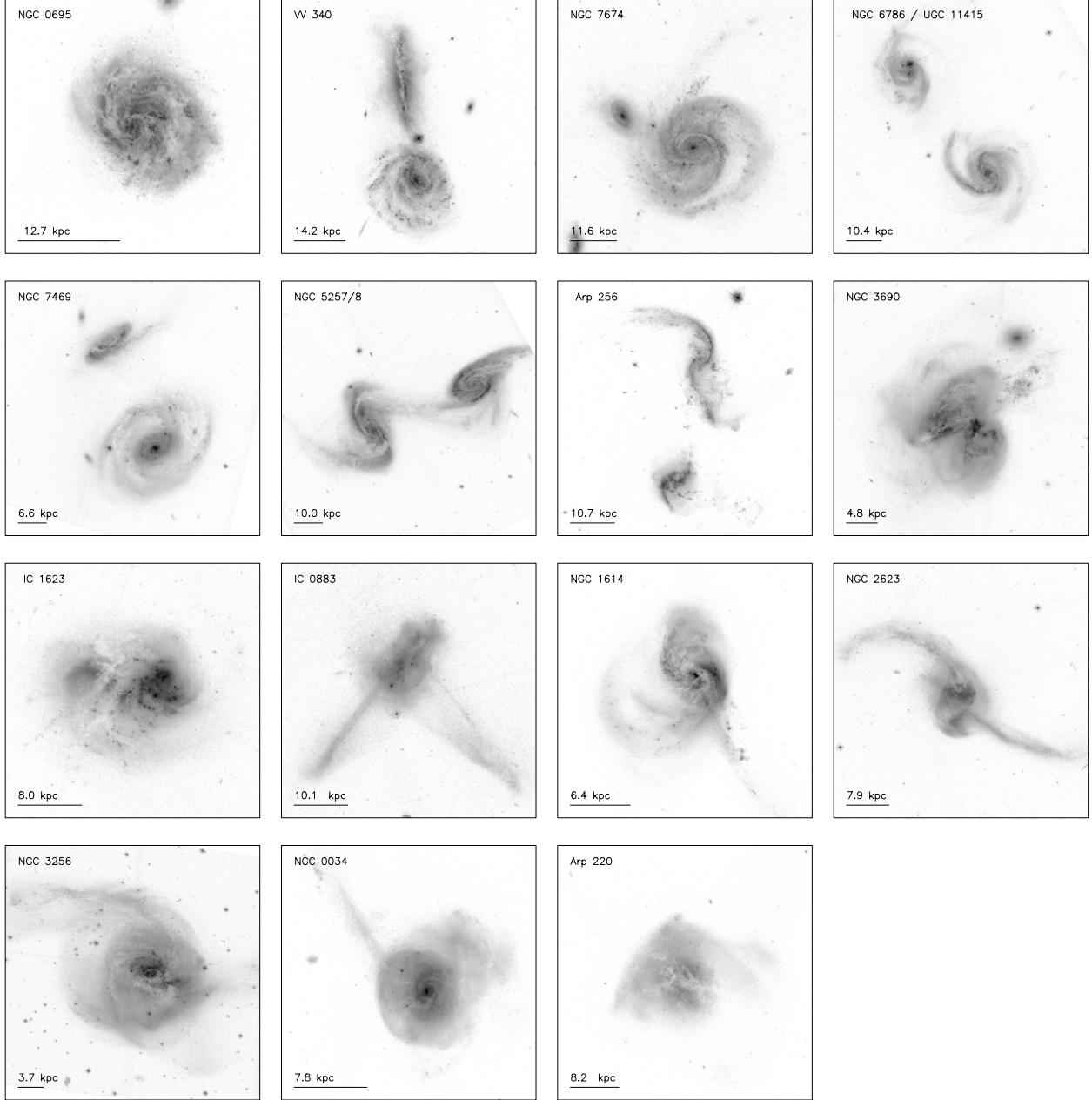


Figure 5: F435W images of the cluster-rich LIRGs sample in merger sequence order from the earliest stage in the upper left to latest stage in the lower right. This order is retained in subsequent figures. The scale bar in the lower left corner corresponds to $20''$ and the number above indicates the scale in kpc at the distance of the system.

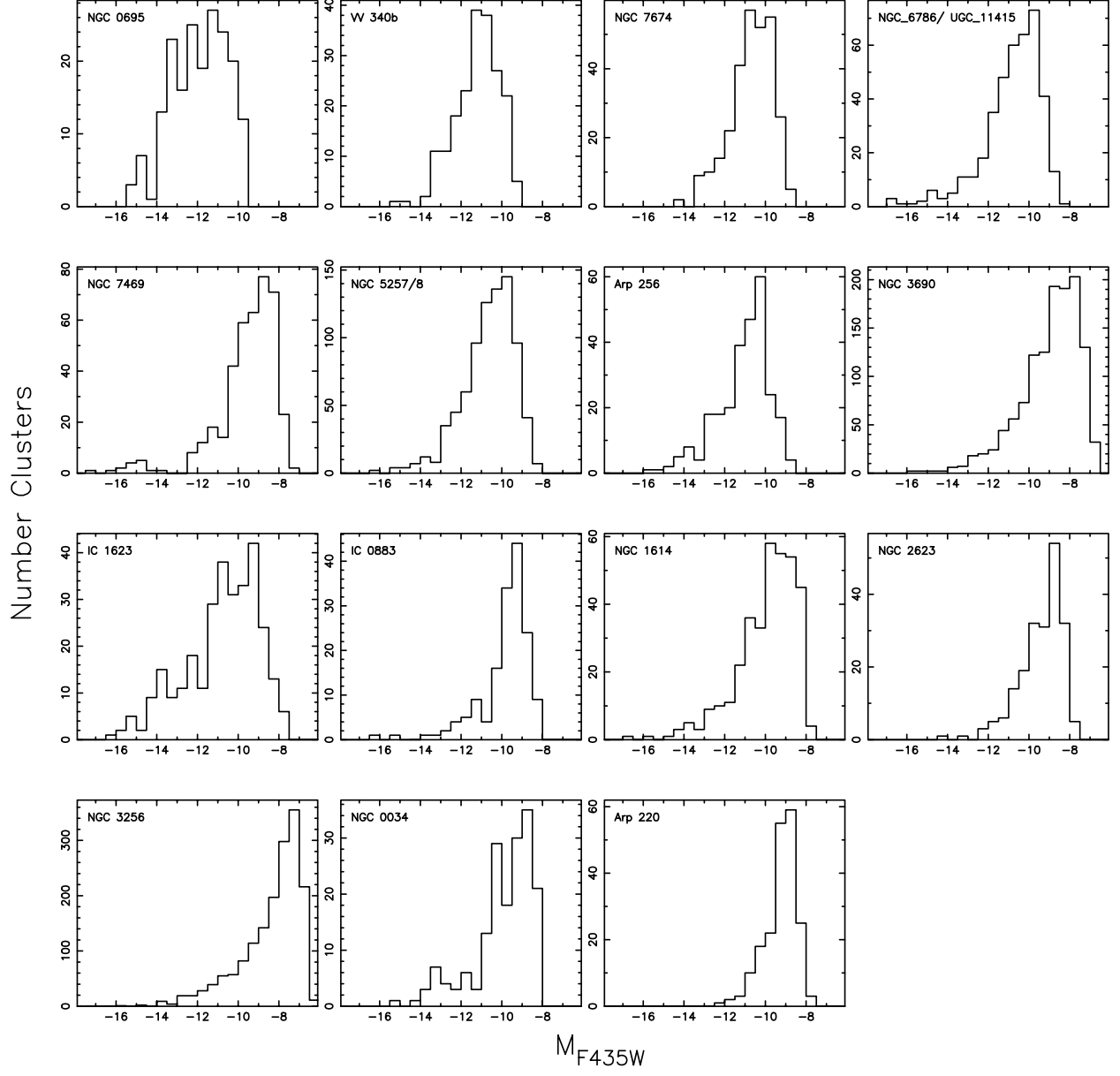


Figure 6: Distribution of absolute F435W magnitudes.

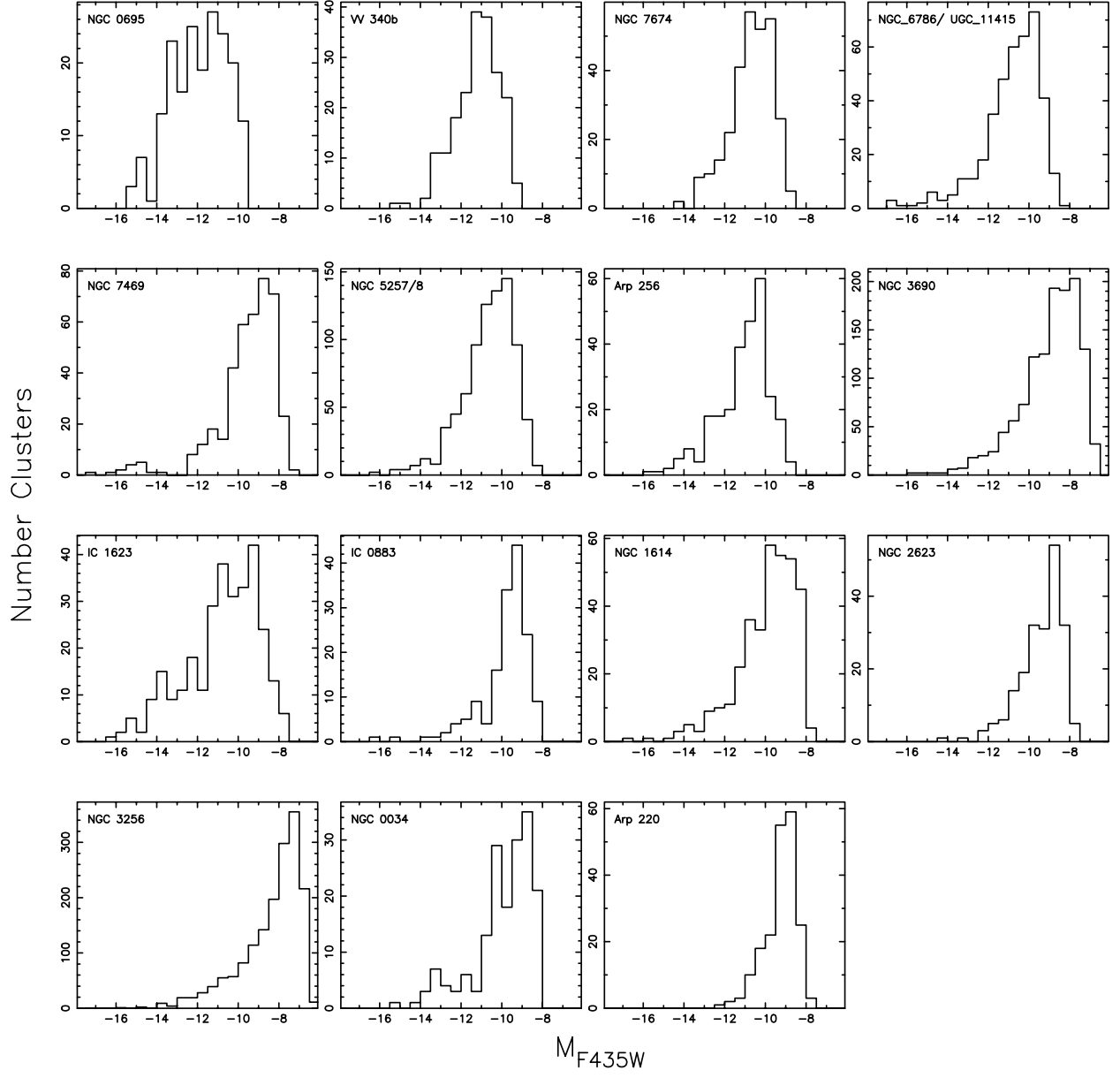


Figure 7: Distribution of absolute F814W magnitudes.

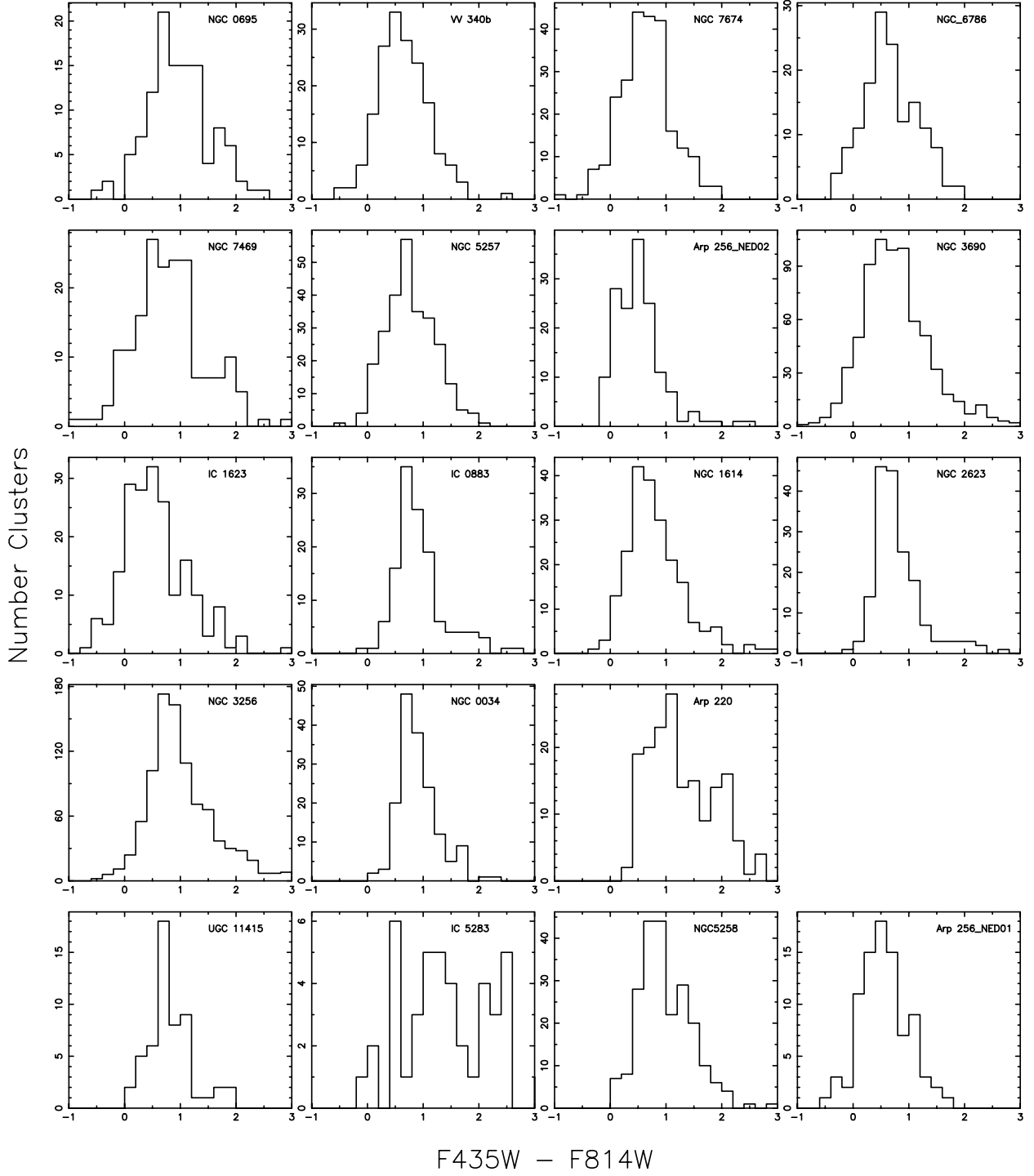


Figure 8: Distribution of $(F435W - F814W)$ colors of clusters. The bottom row shows the four galaxies that are members of galaxy pairs and have fewer detected clusters.

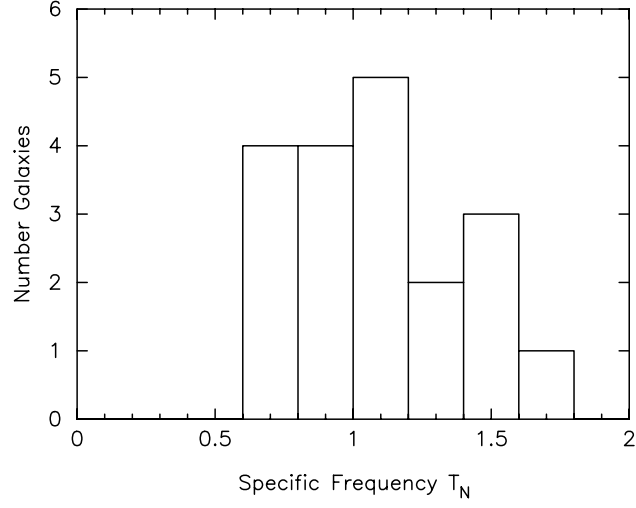


Figure 9: Distribution of corrected specific frequency T_N values in the cluster-rich LIRGs sample.

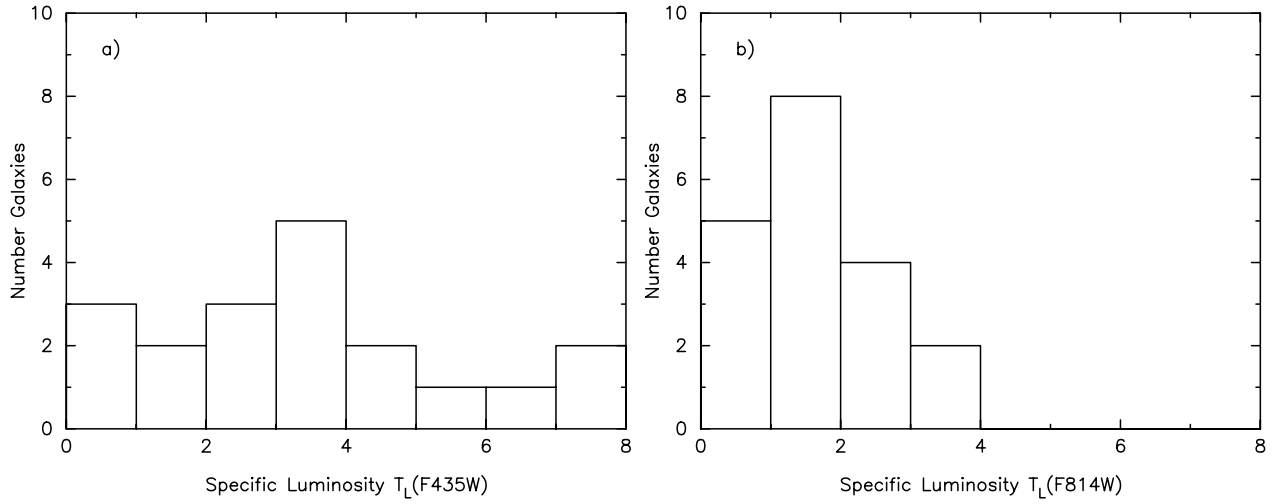


Figure 10: Distribution of specific luminosity T_L values in the cluster-rich LIRGs sample in the F435W (panel a)) and F814W (panel b)) images.

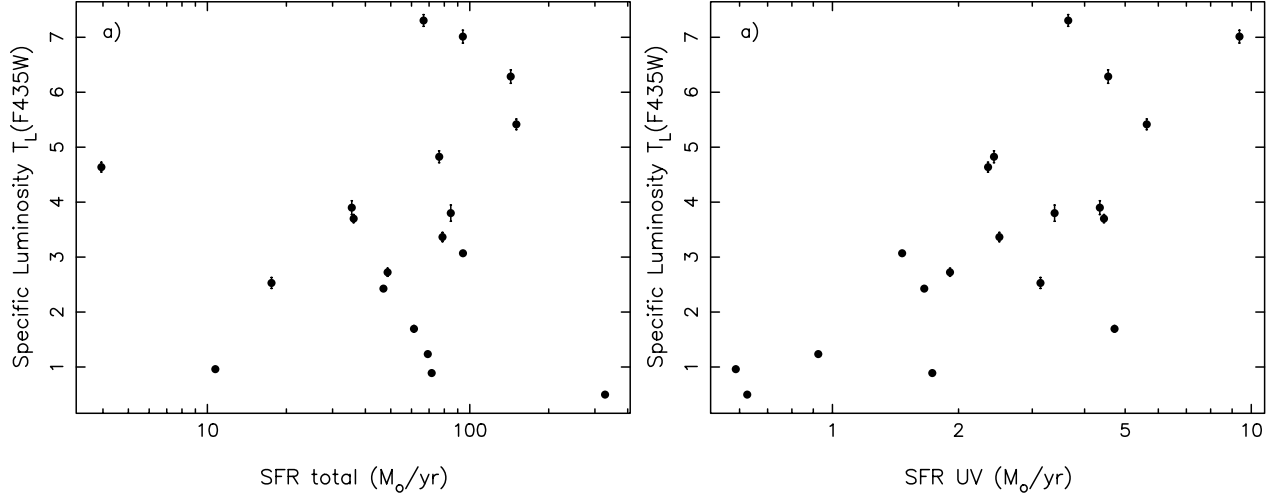


Figure 11: Specific luminosity T_L in the F435W image versus SFR derived from FIR and FUV fluxes (panel a)) and FUV fluxes only (panel b)).

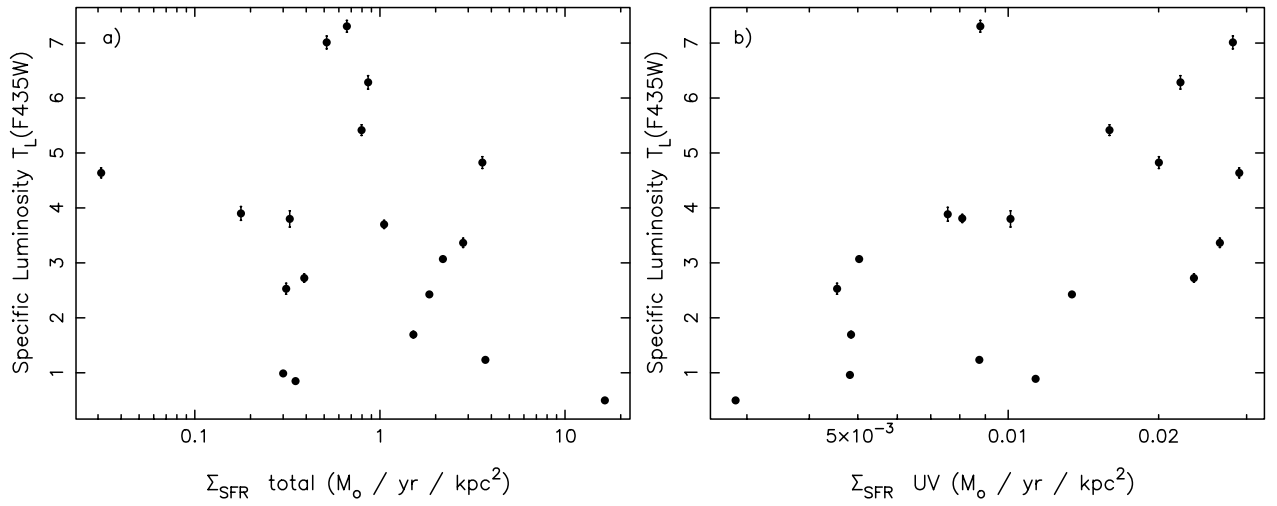


Figure 12: Specific luminosity in the F435W image versus Σ_{SFR} (SFR per unit area) derived from FIR and FUV fluxes (panel a)) and Σ_{SFR} derived from FUV fluxes only (panel b)).

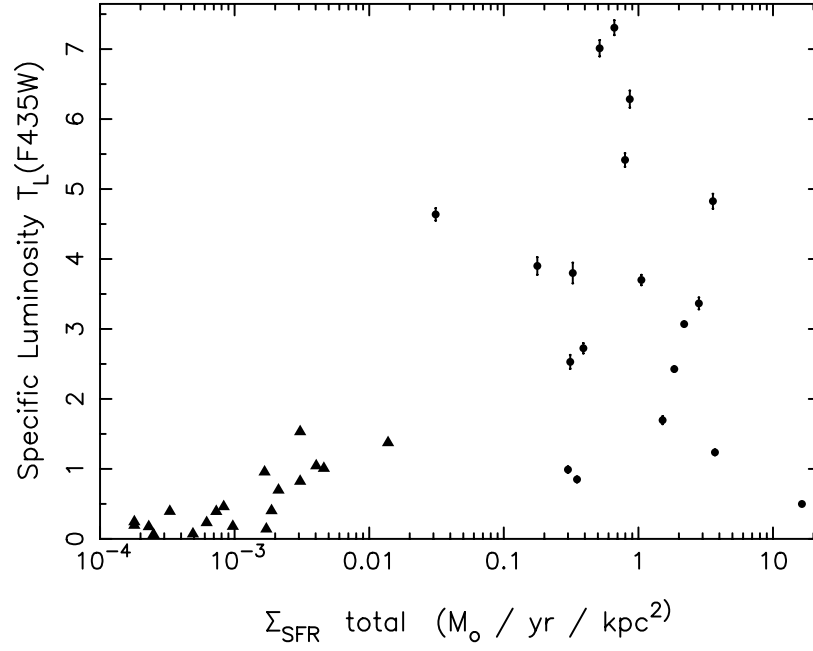


Figure 13: Specific luminosity $T_L(\text{B})$ versus SFR derived from FIR fluxes. The $T_L(\text{B})$ data points for nearby normal spiral galaxies from Larsen & Richtler (2000) are designated with triangles; the $T_L(\text{F435W})$ values of the cluster-rich sample are designated with points.

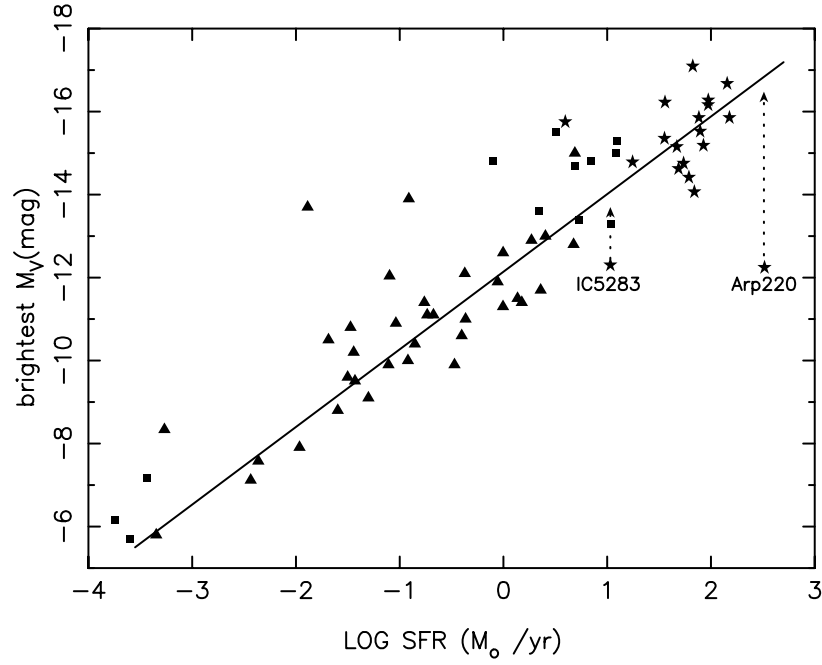


Figure 14: M_V of the most luminous cluster within the galaxy versus SFR. The galaxies from the Larsen (2002b) sample are designated with triangles, the squares mark data from Bastian (2008) Table 1. The cluster-rich LIRGs are indicated with star symbols. The diagonal line is the fit from Weidner et al. (2004). The dashed arrows show the location of two outliers, IC 5283 and Arp 220, after correction for extinction.

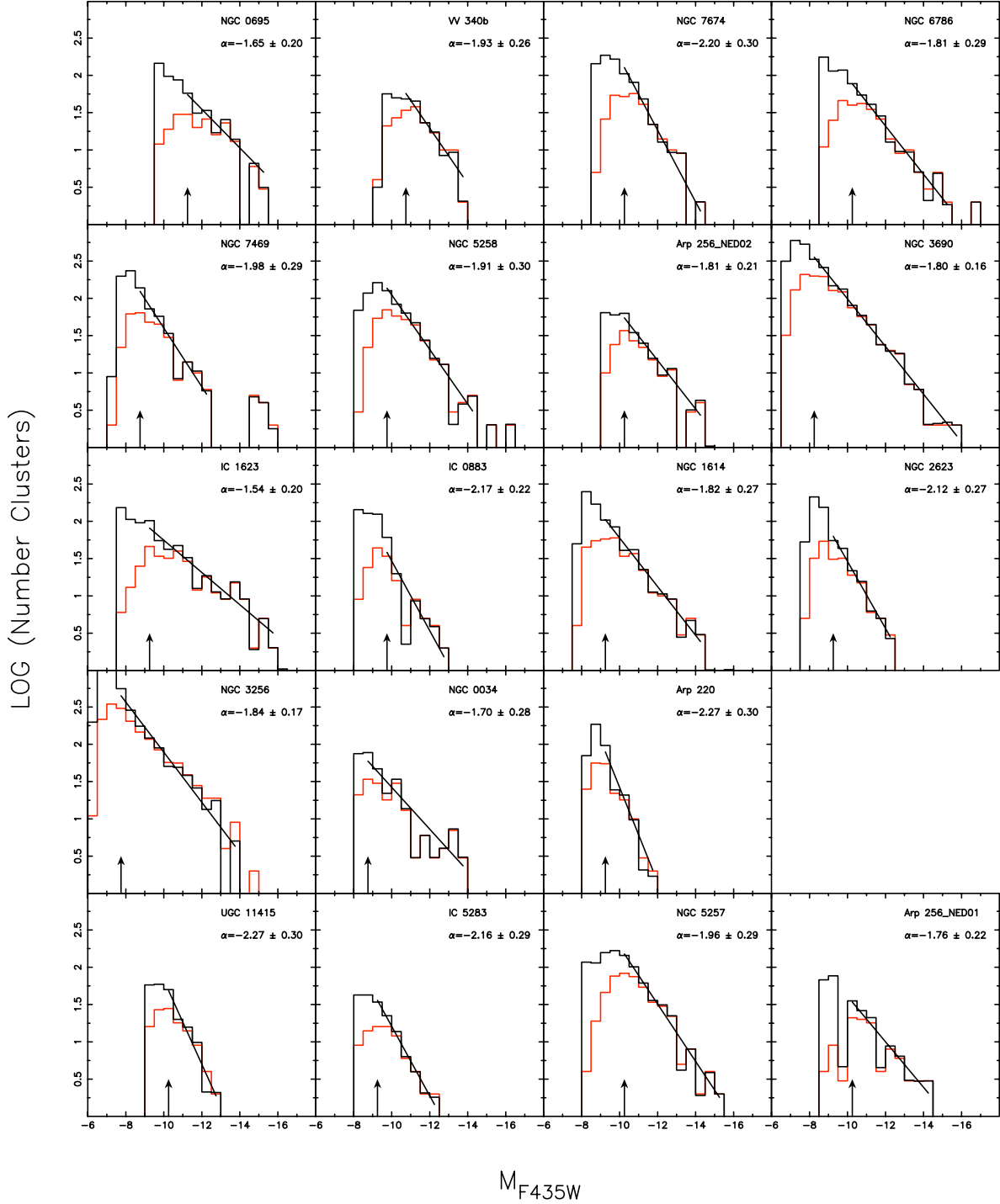


Figure 15: Cluster luminosity function for F435W images. The red histograms represent the raw, uncorrected luminosity distribution. The black histograms have been corrected for foreground stars contamination and for the efficiency of the detection algorithm. The black line is the χ^2 fit to the corrected histograms and the derived power-law index α of the luminosity function is quoted in the upper right corner. The arrow indicates the 50% detection completeness limit.

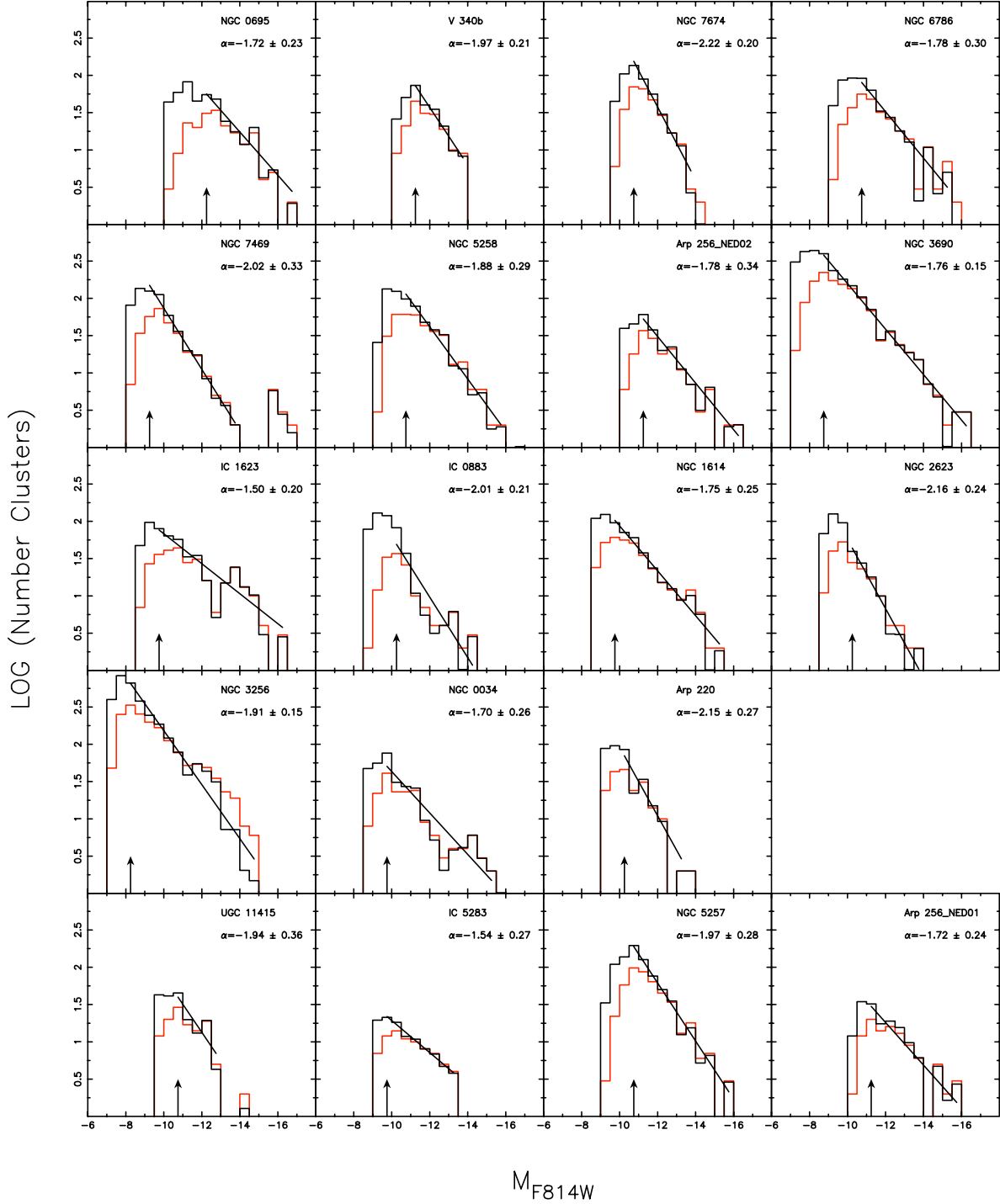


Figure 16: Cluster luminosity function for F814W. The red histograms represent the raw, uncorrected luminosity distribution. The black histograms have been corrected for foreground stars contamination and for the efficiency of the detection algorithm. The black line is the χ^2 fit to the corrected histograms and the derived power-law index α of the luminosity function is quoted in the upper right corner. The arrow indicates the 50% detection completeness limit.

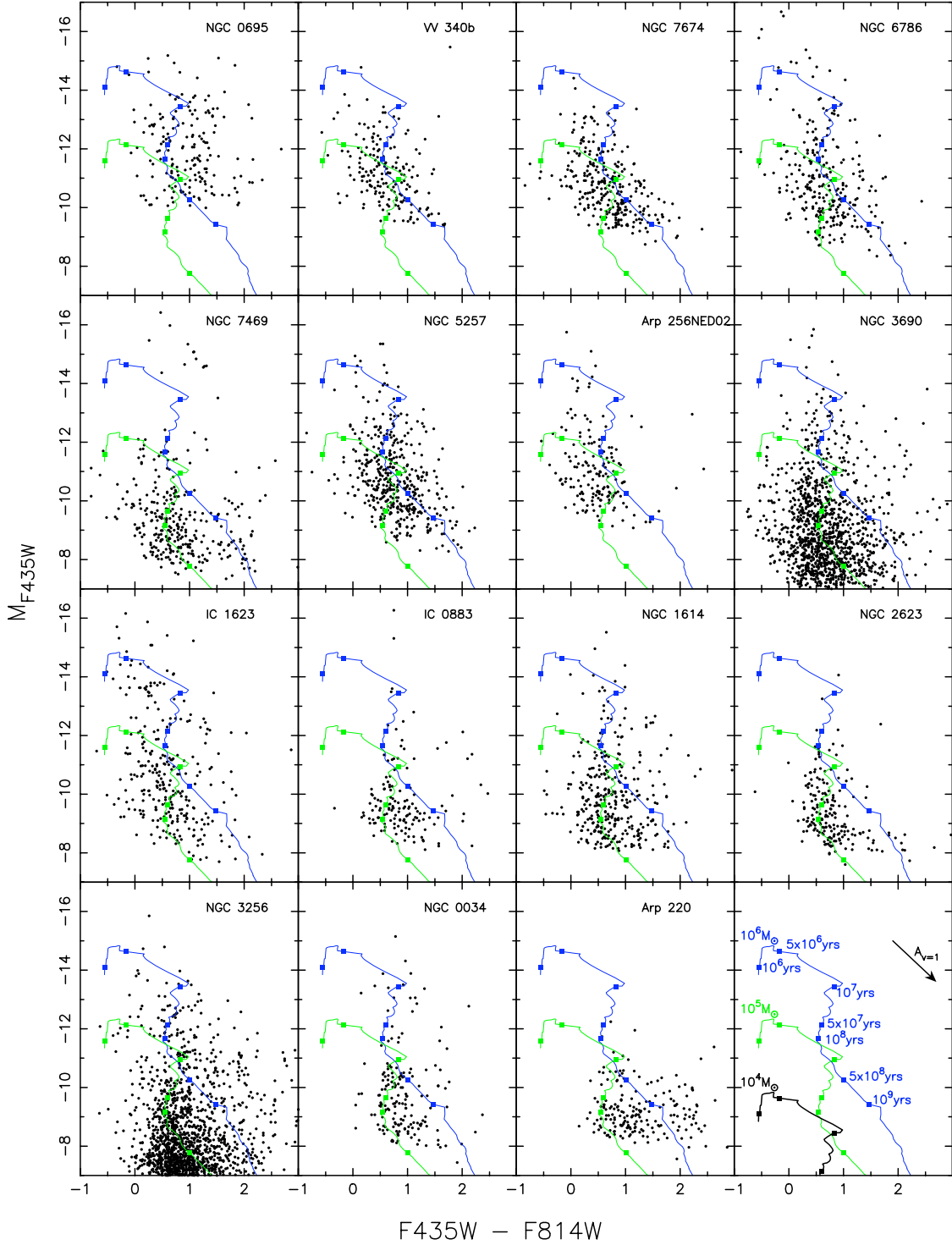


Figure 17: The M_{F435W} versus $(F435W - F814W)$ color-magnitude diagrams. Evolutionary tracks from Bruzual-Charlot population synthesis models for an instantaneous starburst are plotted for cluster masses with $10^5 M_{\odot}$ (green) and $10^6 M_{\odot}$ (blue). The lower right panel contains also the $10^4 M_{\odot}$ track in black. The blue $10^6 M_{\odot}$ track is labeled with ages. The arrow represents 1 magnitude visual extinction. Only SC with $(F435W - F814W)$ error < 0.25 mag are plotted.

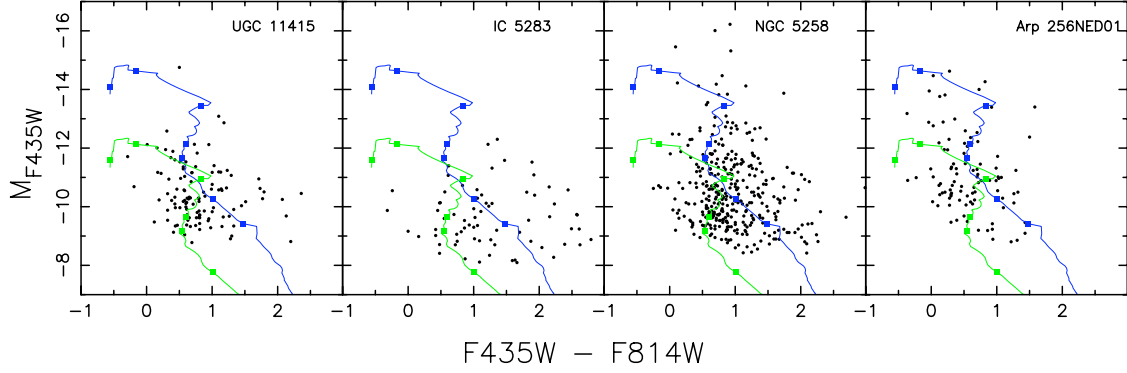


Figure 18: The M_{F435W} versus $(F435W-F814W)$ color-magnitude diagram for the four galaxies that are members of galaxy pairs and have fewer detected clusters.

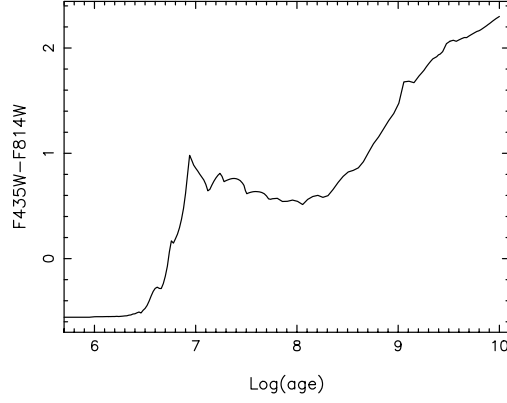


Figure 19: $(F435W-F814W)$ color evolutionary track according to Bruzual-Charlot population synthesis models.

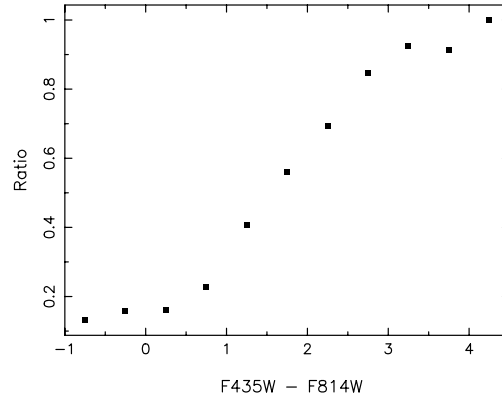


Figure 20: Ratio of clusters located in red galaxy regions (i.e., redder than the median galaxy color) to all detected clusters as a function of cluster color.

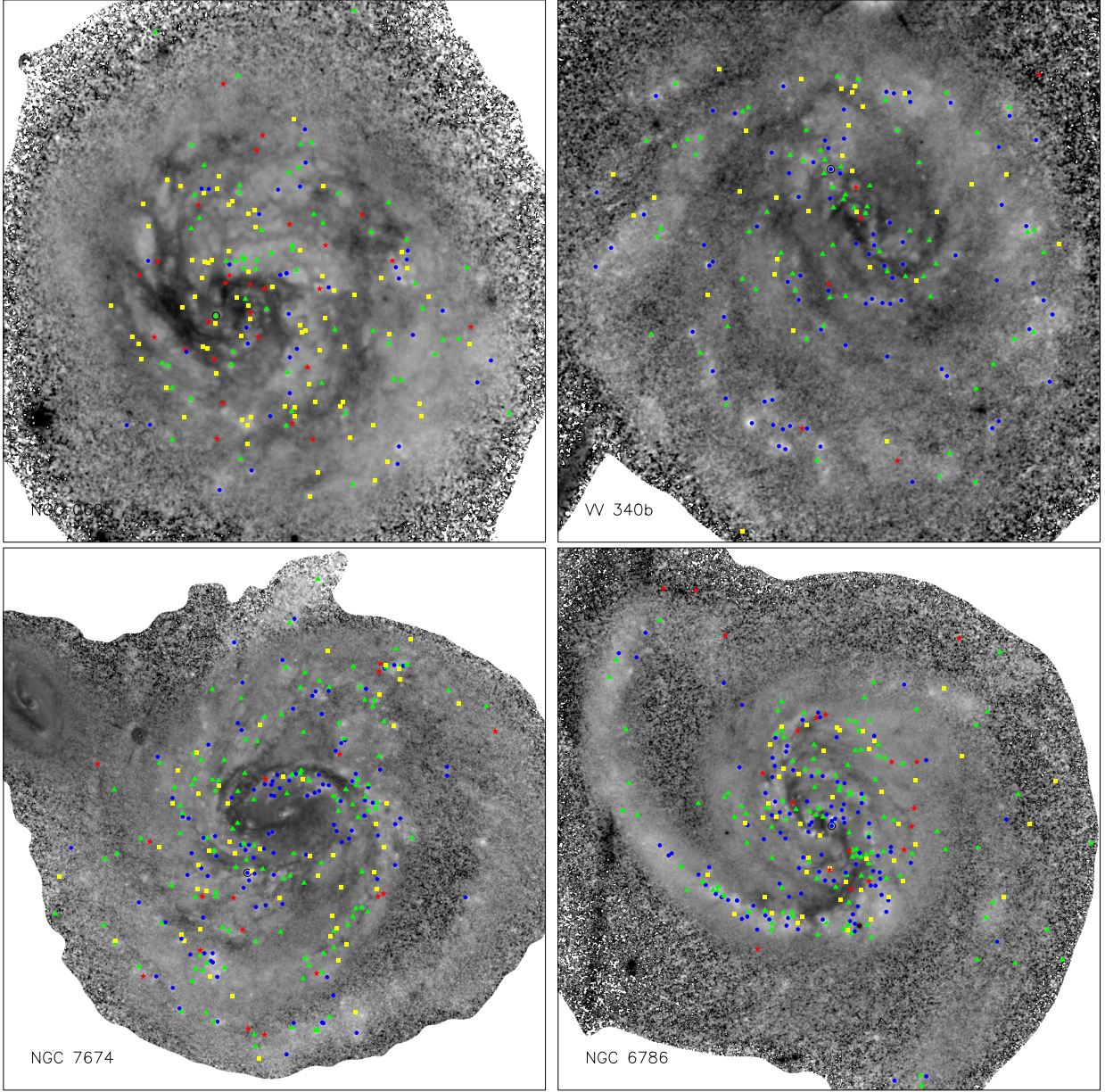


Figure 21: Grey-scale ($F435W-F814W$) host galaxy images with superposed positions of clusters I. Darker shades correspond to larger ($F435W-F814W$) values and redder color and lighter shades to smaller ($F435W-F814W$) values and bluer color. The color value of the cluster represents the ($F435W-F814W$) bin the cluster is in. ($F435W-F814W$) < 0.51 bin clusters are designated with blue dots, $0.51 < (F435W-F814W) < 1.0$ with green triangles, $1.0 < (F435W-F814W) < 1.5$ with yellow squares, ($F435W-F814W$) > 1.5 with red stars. Black circle indicates the most luminous cluster. LIRGs are arranged in the merger sequence order.

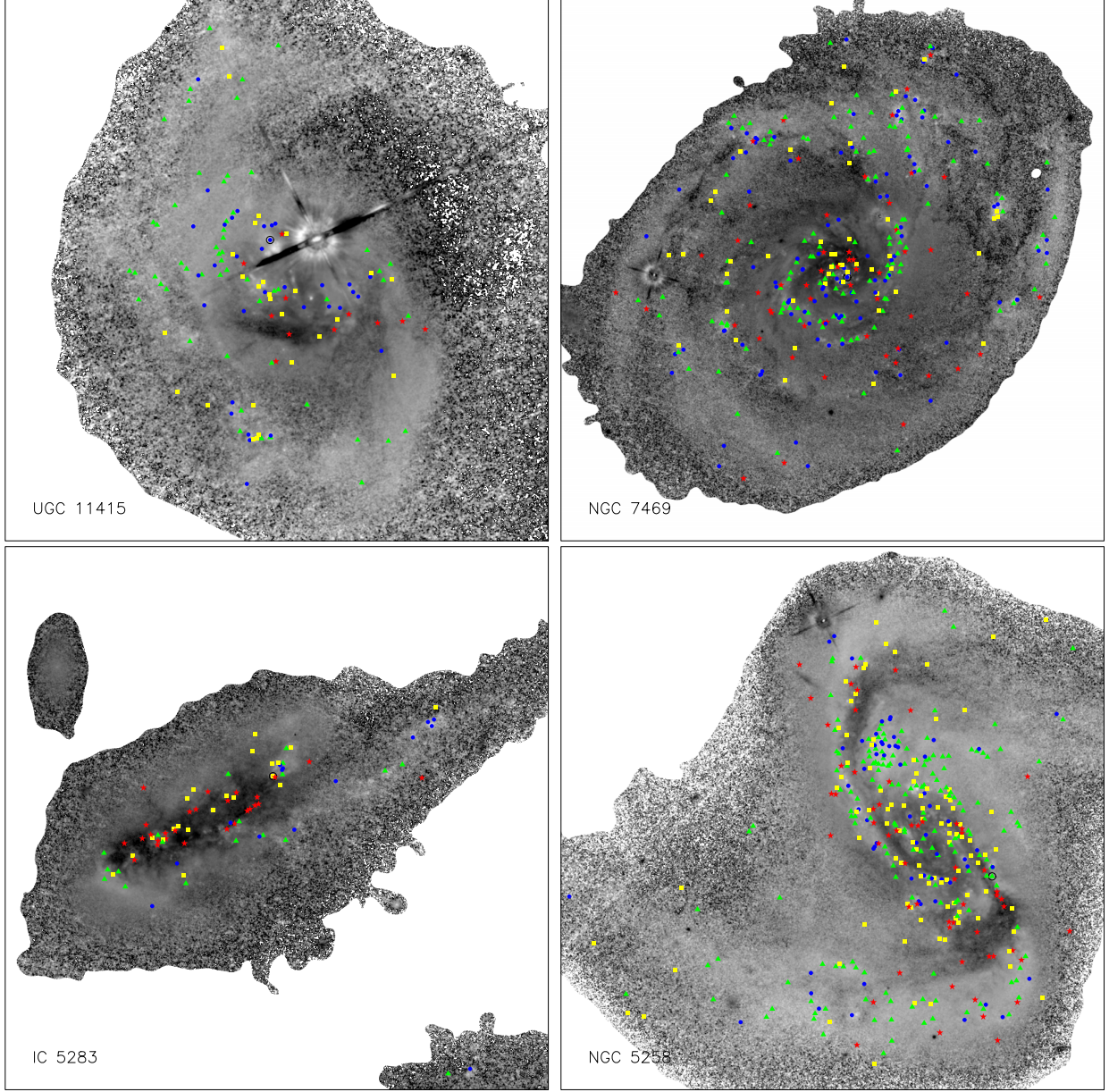


Figure 21: $(F435W - F814W)$ images with superposed positions of clusters II. The color value of the cluster represents the $(F435W - F814W)$ bin the cluster is in. $(F435W - F814W) < 0.51$ bin clusters are designated with blue dots, $0.51 < (F435W - F814W) < 1.0$ with green triangles, $1.0 < (F435W - F814W) < 1.5$ with yellow squares, $(F435W - F814W) > 1.5$ with red stars. Black circle indicates the most luminous cluster.

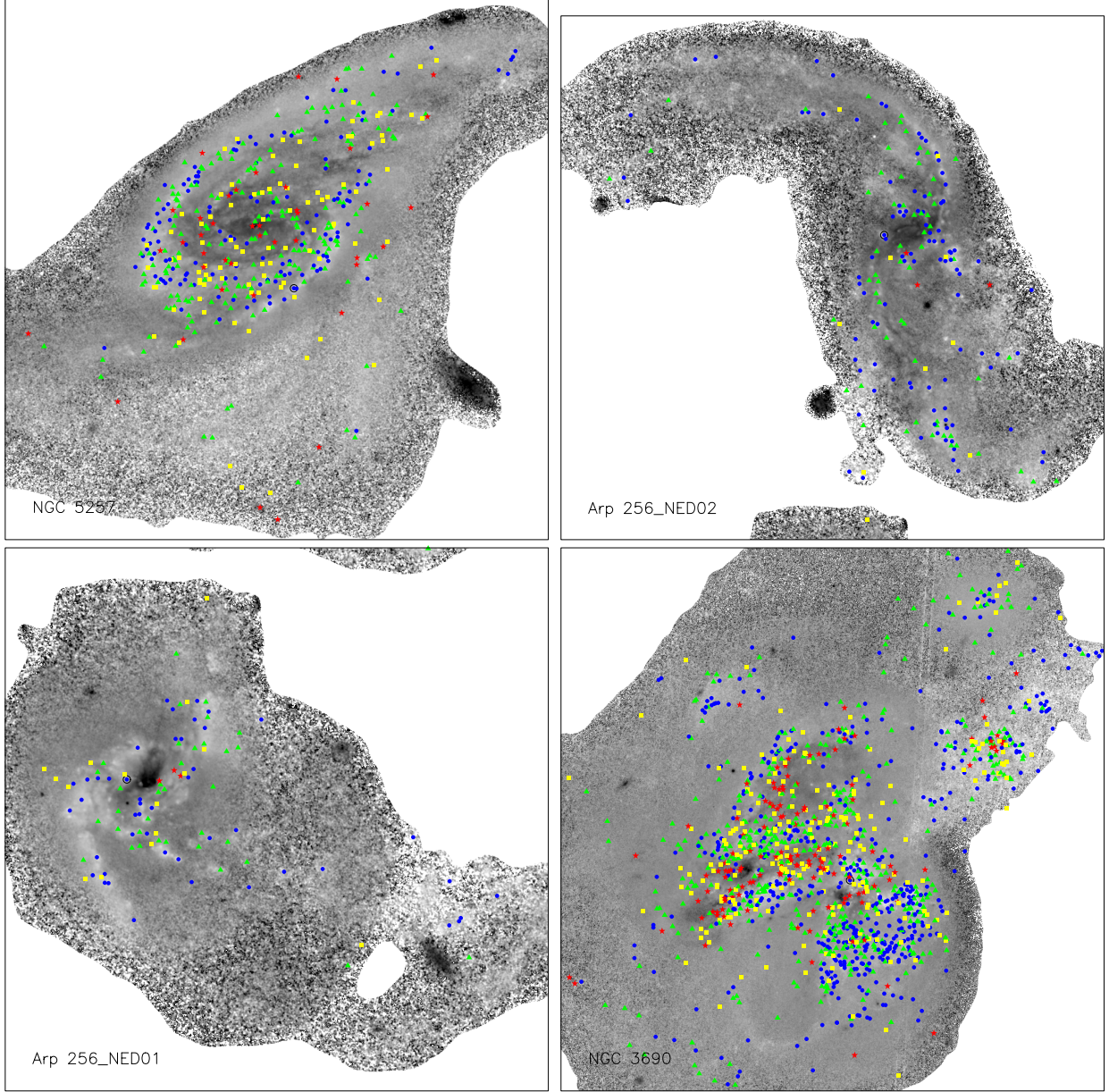


Figure 21: $(F435W-F814W)$ images with superposed positions of clusters III. The color value of the cluster represents the $(F435W-F814W)$ bin the cluster is in. $(F435W-F814W) < 0.51$ bin clusters are designated with blue dots, $0.51 < (F435W-F814W) < 1.0$ with green triangles, $1.0 < (F435W-F814W) < 1.5$ with yellow squares, $(F435W-F814W) > 1.5$ with red stars. Black circle indicates the most luminous cluster.

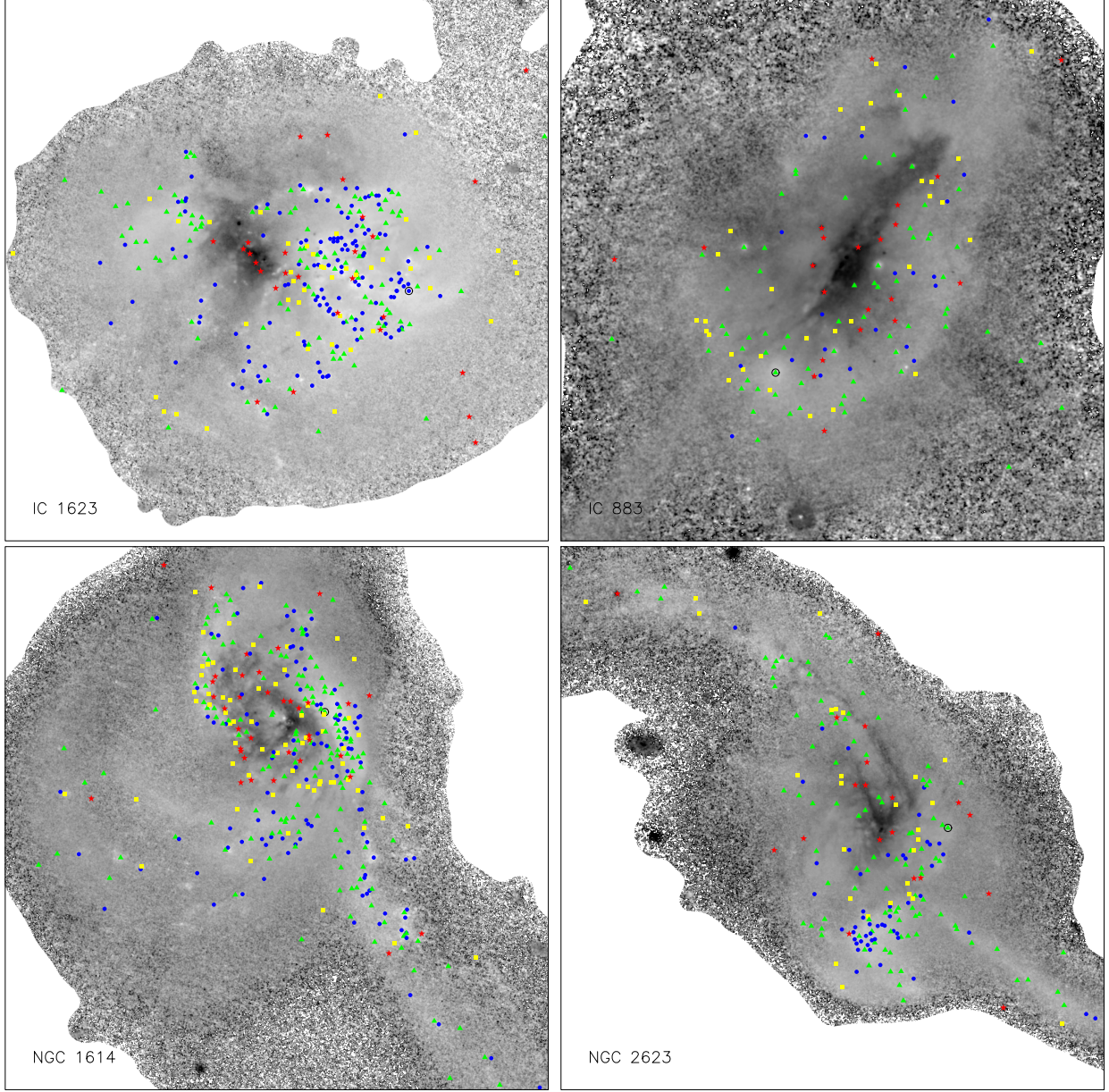


Figure 21: $(F435W - F814W)$ images with superposed positions of clusters IV. The color value of the cluster represents the $(F435W - F814W)$ bin the cluster is in. $(F435W - F814W) < 0.51$ bin clusters are designated with blue dots, $0.51 < (F435W - F814W) < 1.0$ with green triangles, $1.0 < (F435W - F814W) < 1.5$ with yellow squares, $(F435W - F814W) > 1.5$ with red stars. Black circle indicates the most luminous cluster.

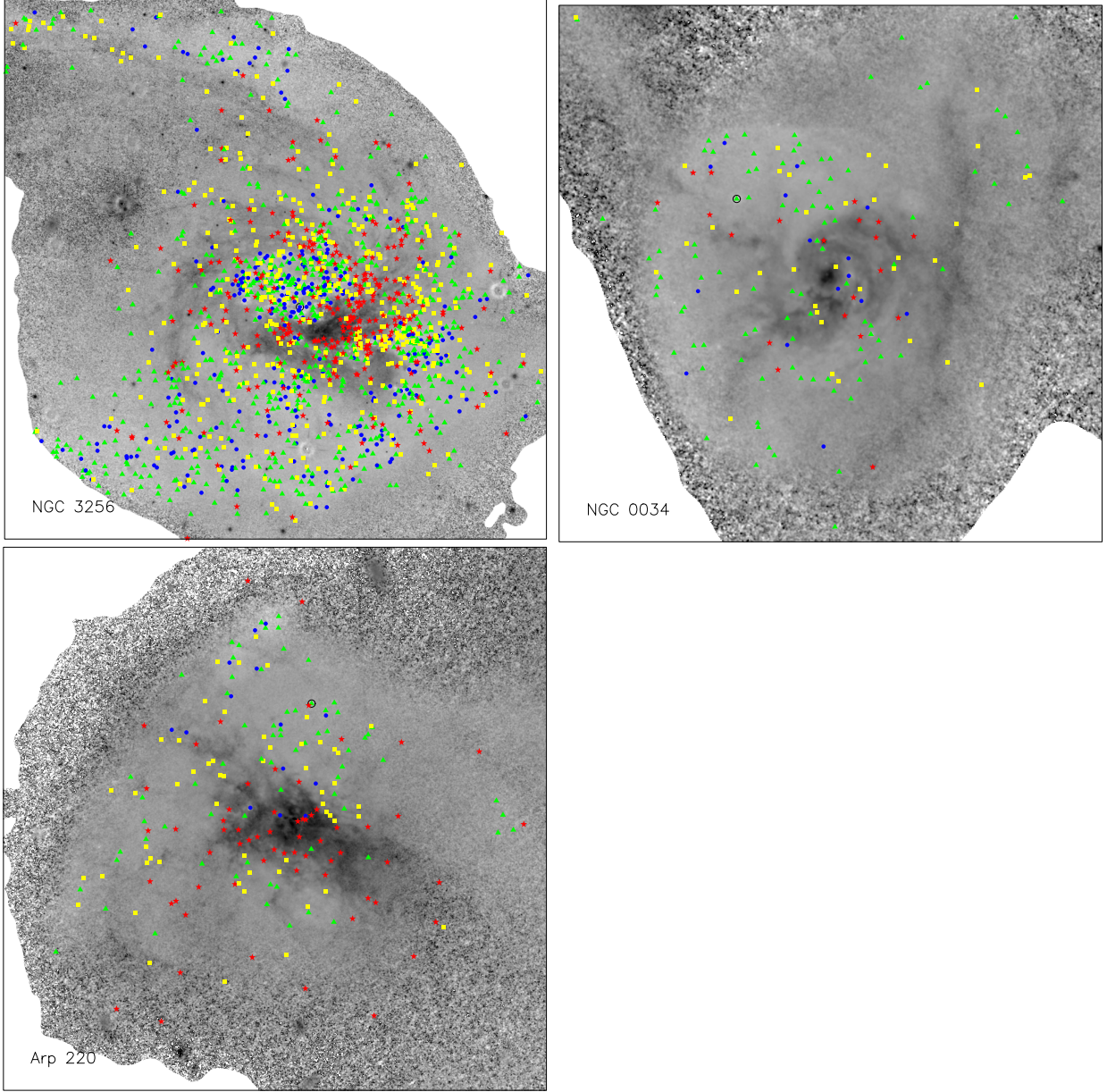


Figure 21: $(F435W-F814W)$ images with superposed positions of clusters V. The color value of the cluster represents the $(F435W-F814W)$ bin the cluster is in. $(F435W-F814W) < 0.51$ bin clusters are designated with blue dots, $0.51 < (F435W-F814W) < 1.0$ with green triangles, $1.0 < (F435W-F814W) < 1.5$ with yellow squares, $(F435W-F814W) > 1.5$ with red stars. Black circle indicates the most luminous cluster.

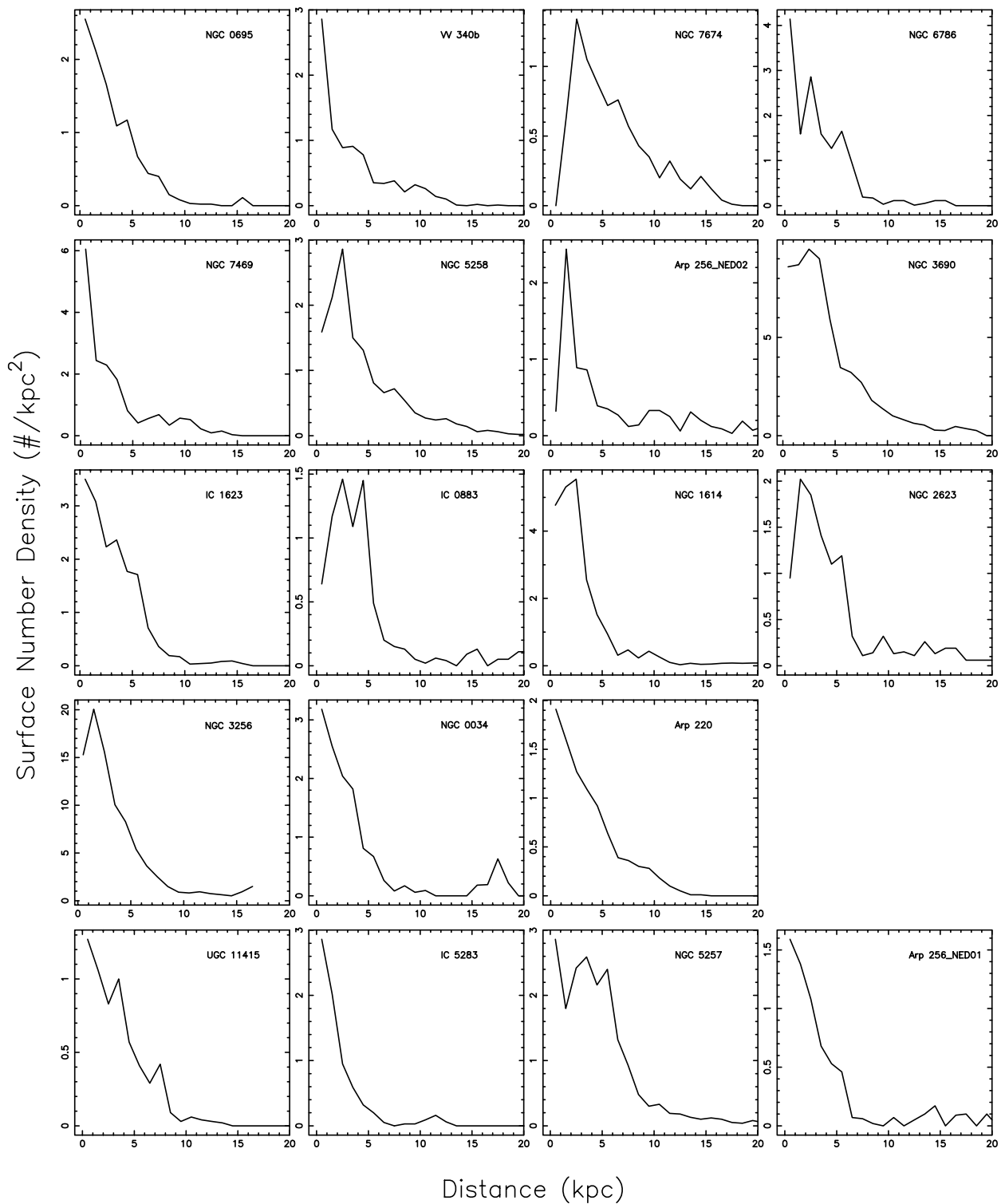


Figure 22: Cluster surface density as a function of distance from the $8\mu\text{m}$ centroid. The bottom row shows the four galaxies that are members of galaxy pairs and have fewer detected clusters.

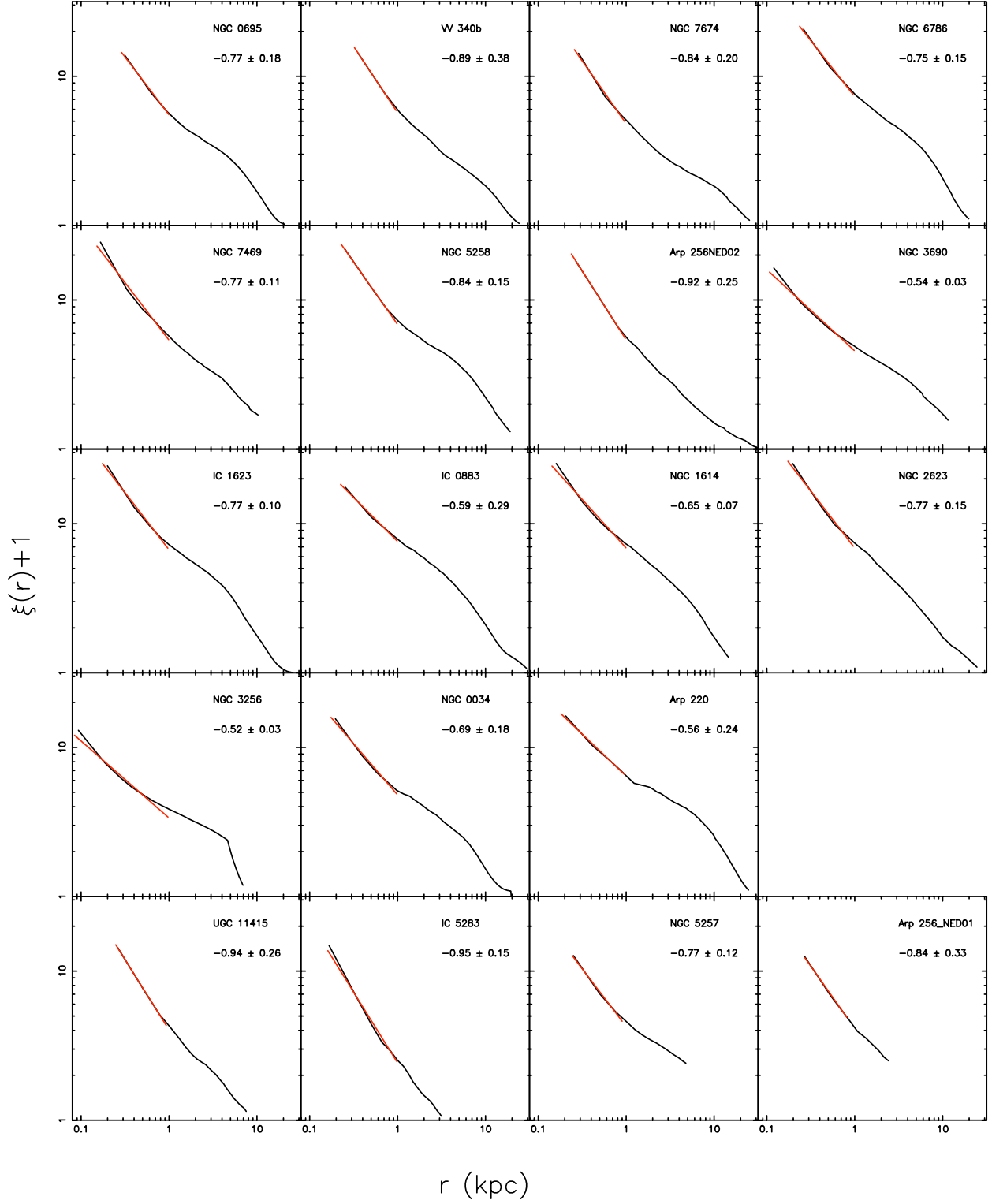


Figure 23: Autocorrelation functions of SCs. Both axis are shown on a logarithmic scale. The red line is a linear fit to the autocorrelation function up to a distance of 1 kpc. The index of the power-law is indicated in the upper right corner. The bottom row shows the four galaxies that are members of galaxy pairs and have fewer detected clusters.

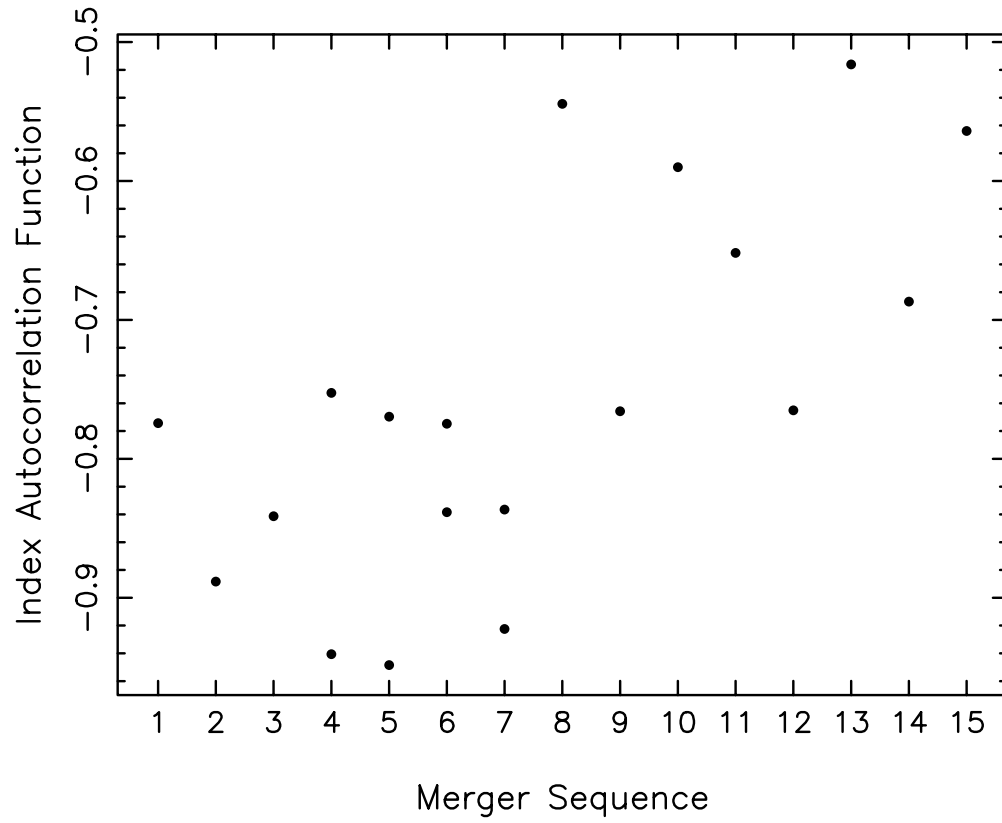


Figure 24: Indices of the power law fit to autocorrelation functions versus merger sequence in the same order as in Figure 5.

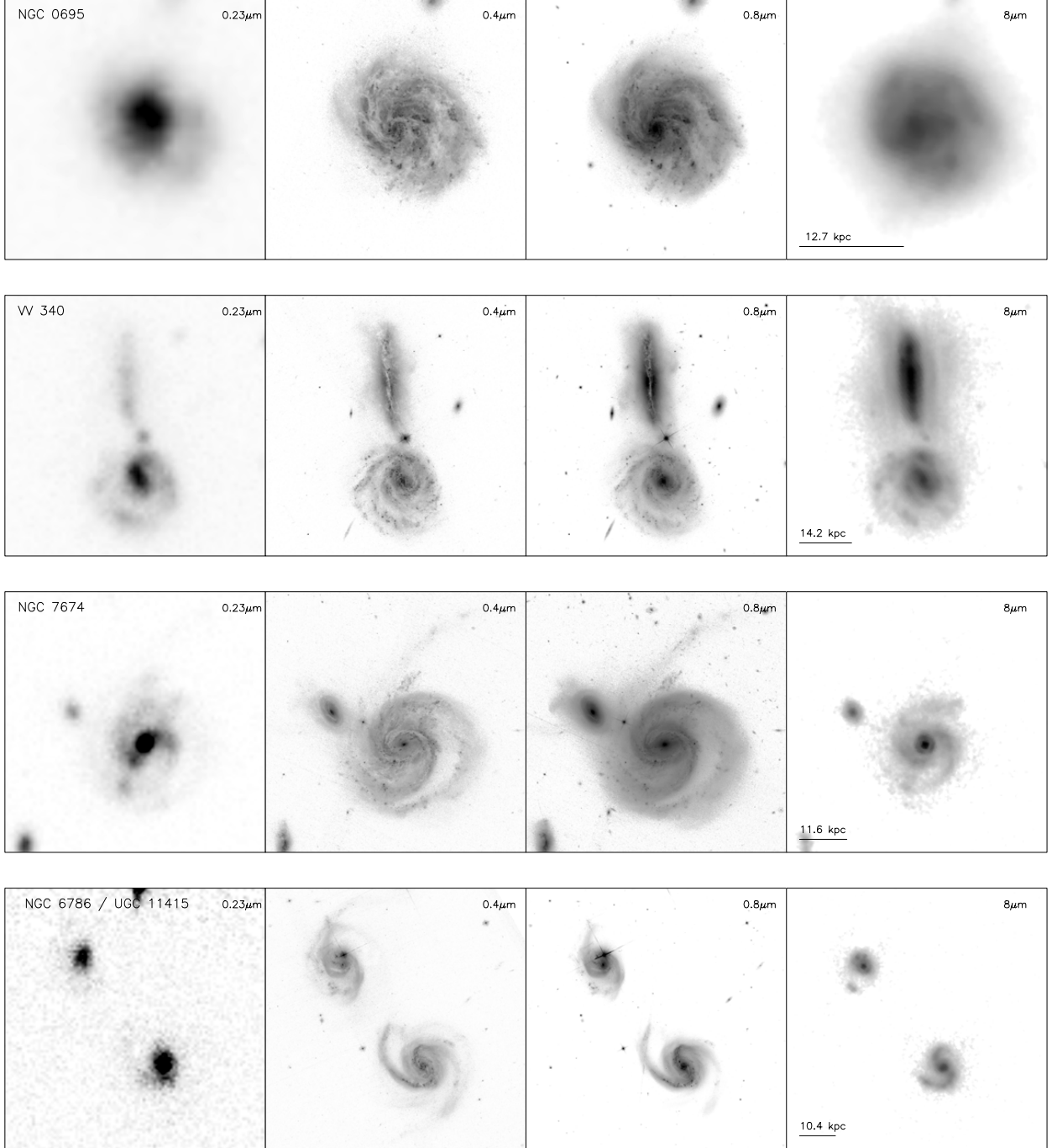


Figure 25: Multi-wavelength view of the cluster-rich LIRGs sample I. Each row shows *GALEX* near-UV, *HST*/ACS F435W, *HST*/ACS F814W and *Spitzer* IRAC 8 μm images. The scale bar in the lower left corner corresponds to 20'' and the number above indicates the scale in kpc at the distance of the system. LIRGs are arranged in the merger sequence order.

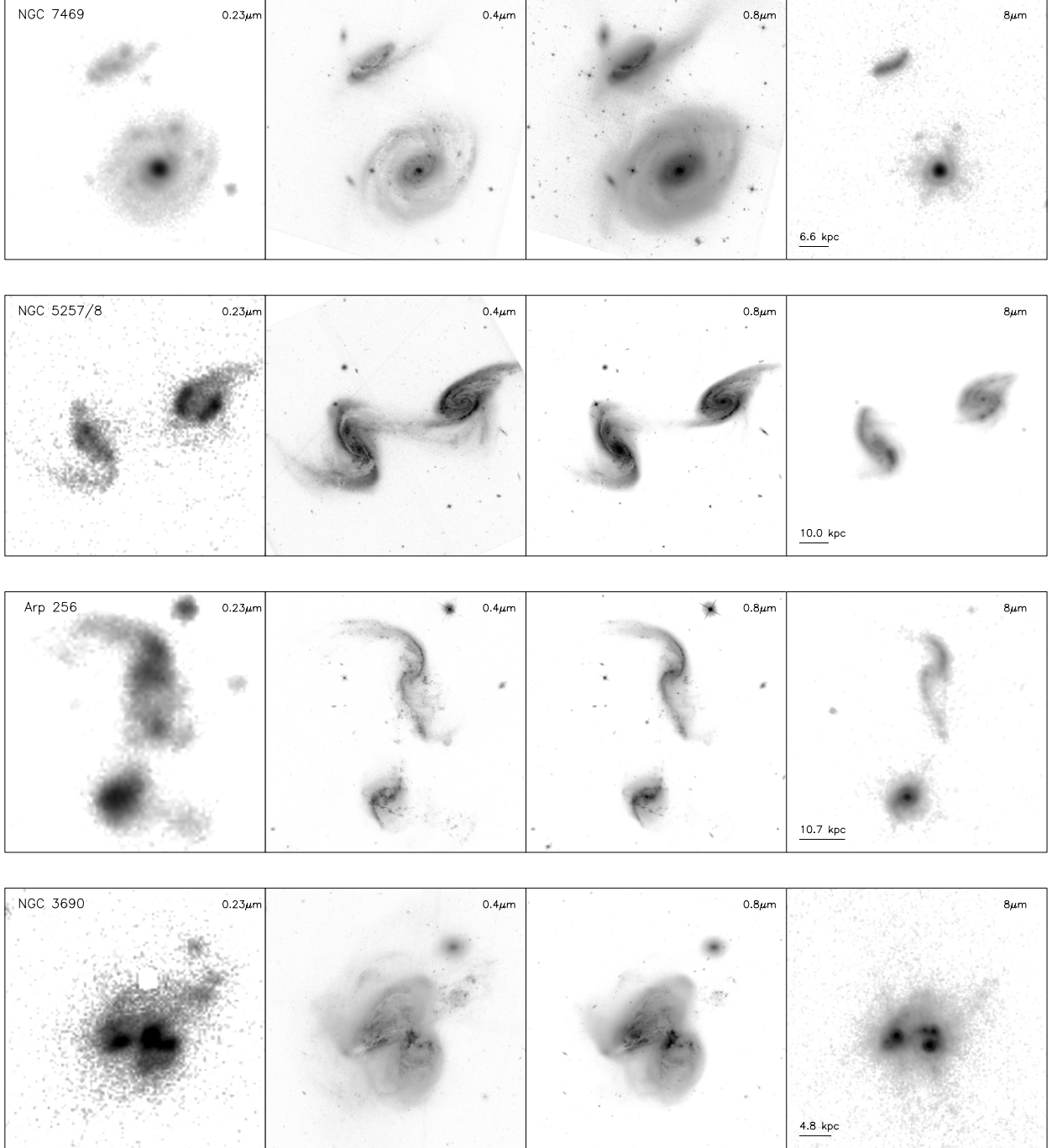


Figure 25: Multi-wavelength view of the cluster-rich LIRGs sample II. Each row shows *GALEX* near-UV, *HST*/ACS F435W, *HST*/ACS F814W and *Spitzer* IRAC 8 μm images. The scale bar in the lower left corner corresponds to 20'' and the number above indicates the scale in kpc at the distance of the system. LIRGs are arranged in the merger sequence order.

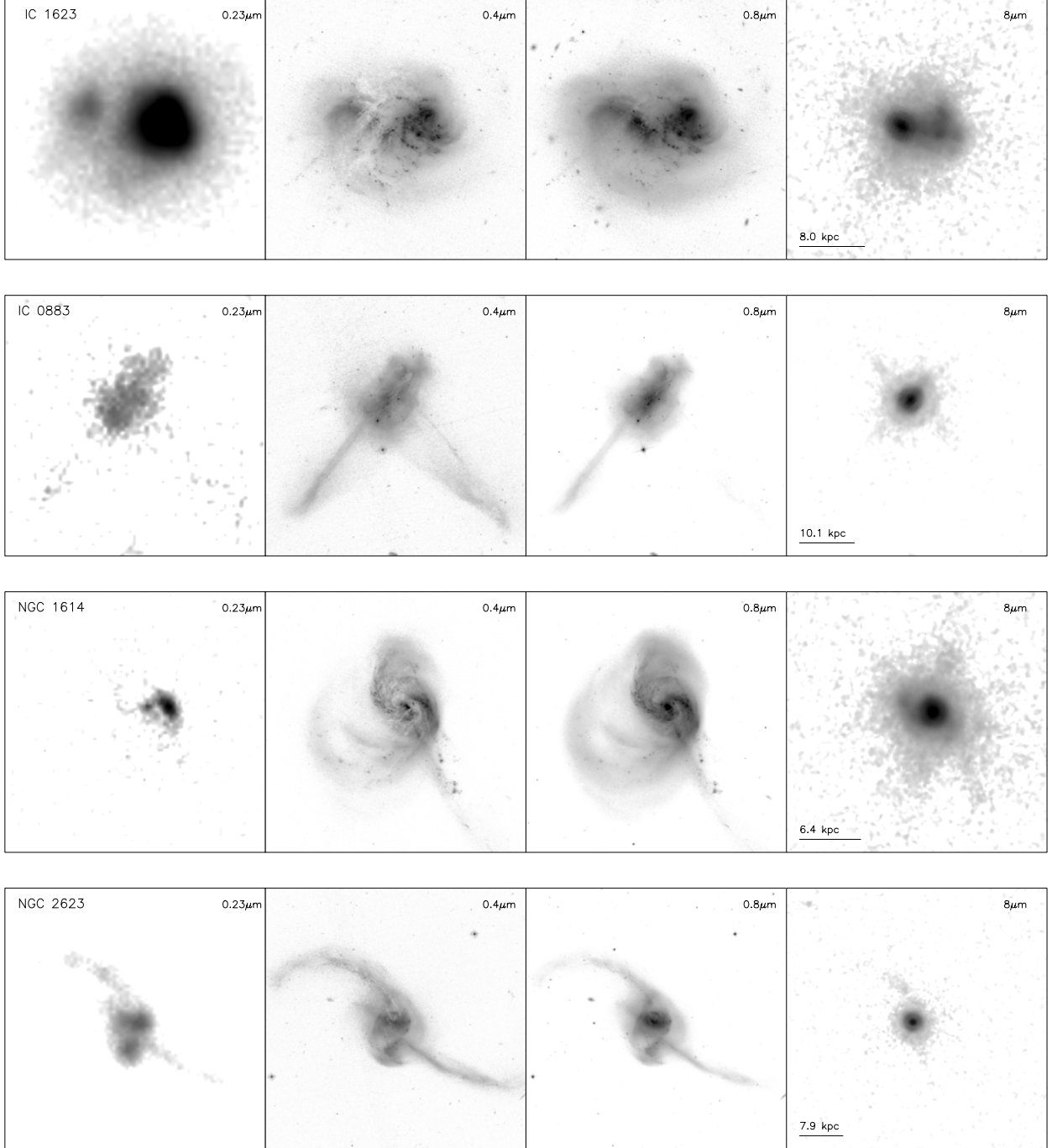


Figure 25: Multi-wavelength view of the cluster-rich LIRGs sample III. Each row shows *GALEX* near-UV, *HST*/ACS F435W, *HST*/ACS F814W and *Spitzer* IRAC $8\mu\text{m}$ images. The scale bar in the lower left corner corresponds to $20''$ and the number above indicates the scale in kpc at the distance of the system. LIRGs are arranged in the merger sequence order.

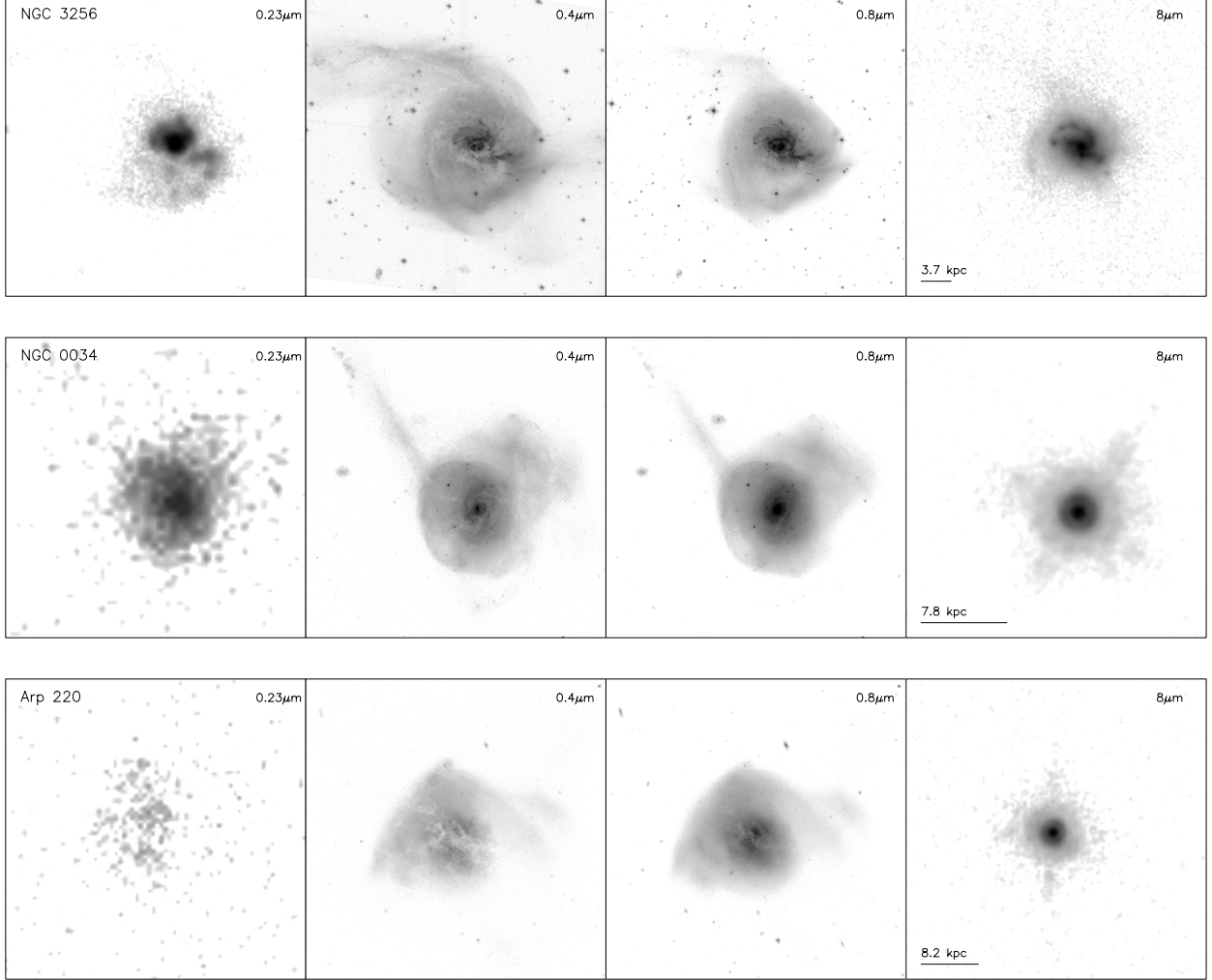


Figure 25: Multi-wavelength view of the cluster-rich LIRGs sample IV. Each row shows *GALEX* near-UV, *HST*/ACS F435W, *HST*/ACS F814W and *Spitzer* IRAC 8 μm images. The scale bar in the lower left corner corresponds to 20'' and the number above indicates the scale in kpc at the distance of the system. LIRGs are arranged in the merger sequence order.

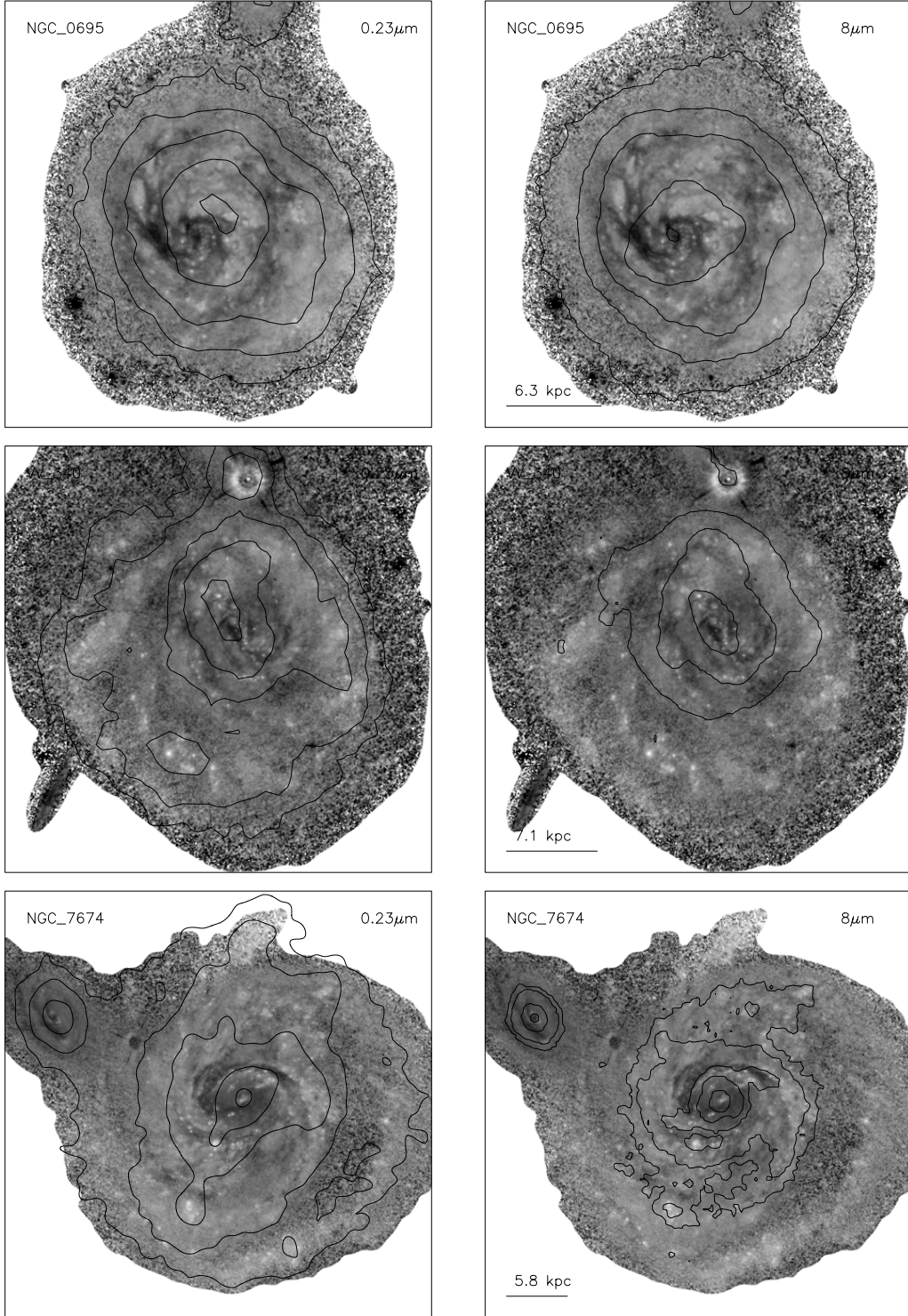


Figure 26: *GALEX* NUV 0.23 μ m contours (left column) and *Spitzer* IRAC 8 μ m contours superposed on grey-scale (F435W–F814W) host galaxy images I. Darker shades correspond to larger (F435W–F814W) values and redder color and lighter shades to smaller (F435W–F814W) values and bluer color. The scale bar in the lower left corner corresponds to 10'' and the number above indicates the scale in kpc at the distance of the system. LIRGs are arranged in the merger sequence order.

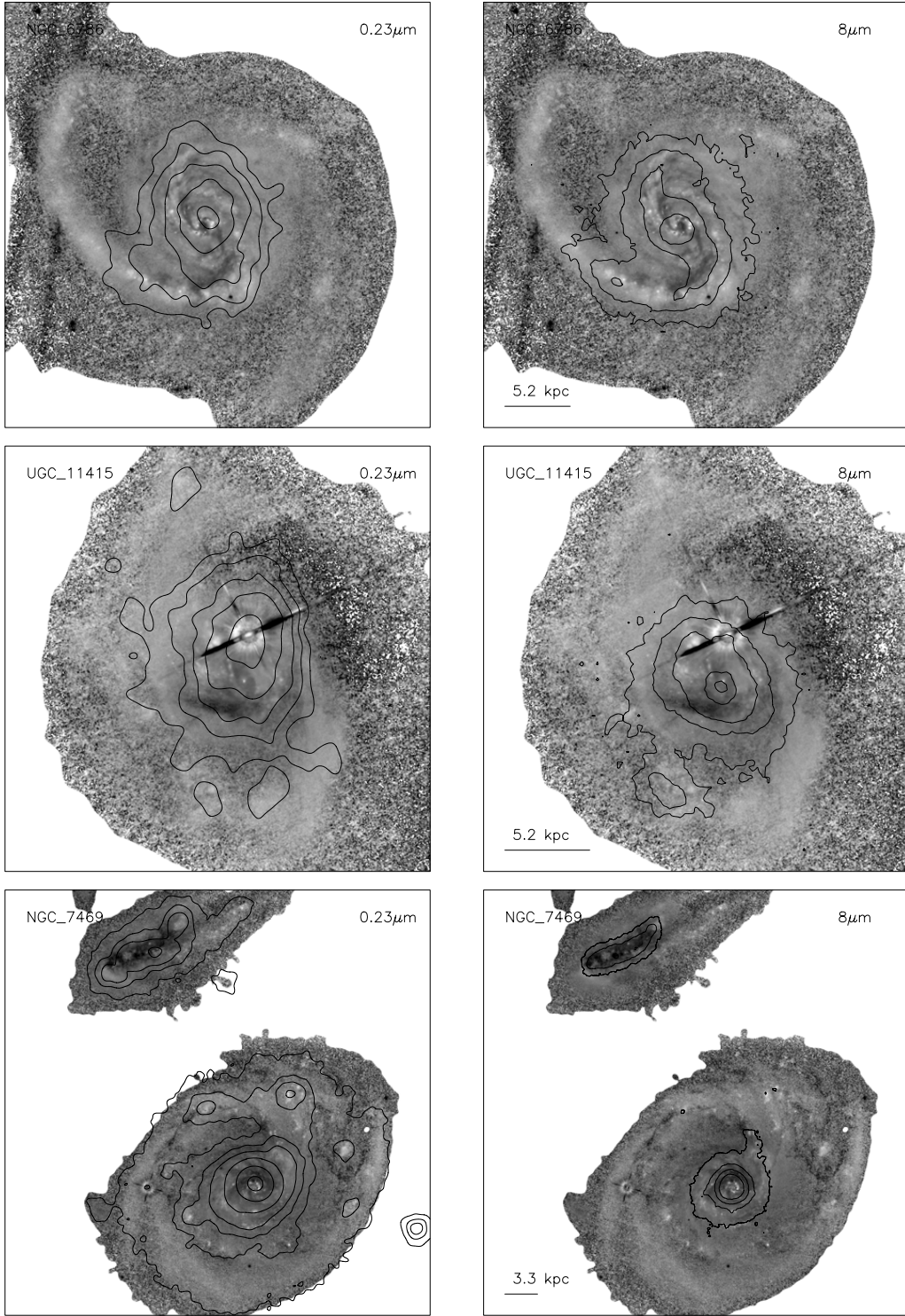


Figure 26: *GALEX* NUV 0.23 μm contours (left column) and *Spitzer* IRAC 8 μm contours superposed on grey-scale (F435W–F814W) host galaxy images II.

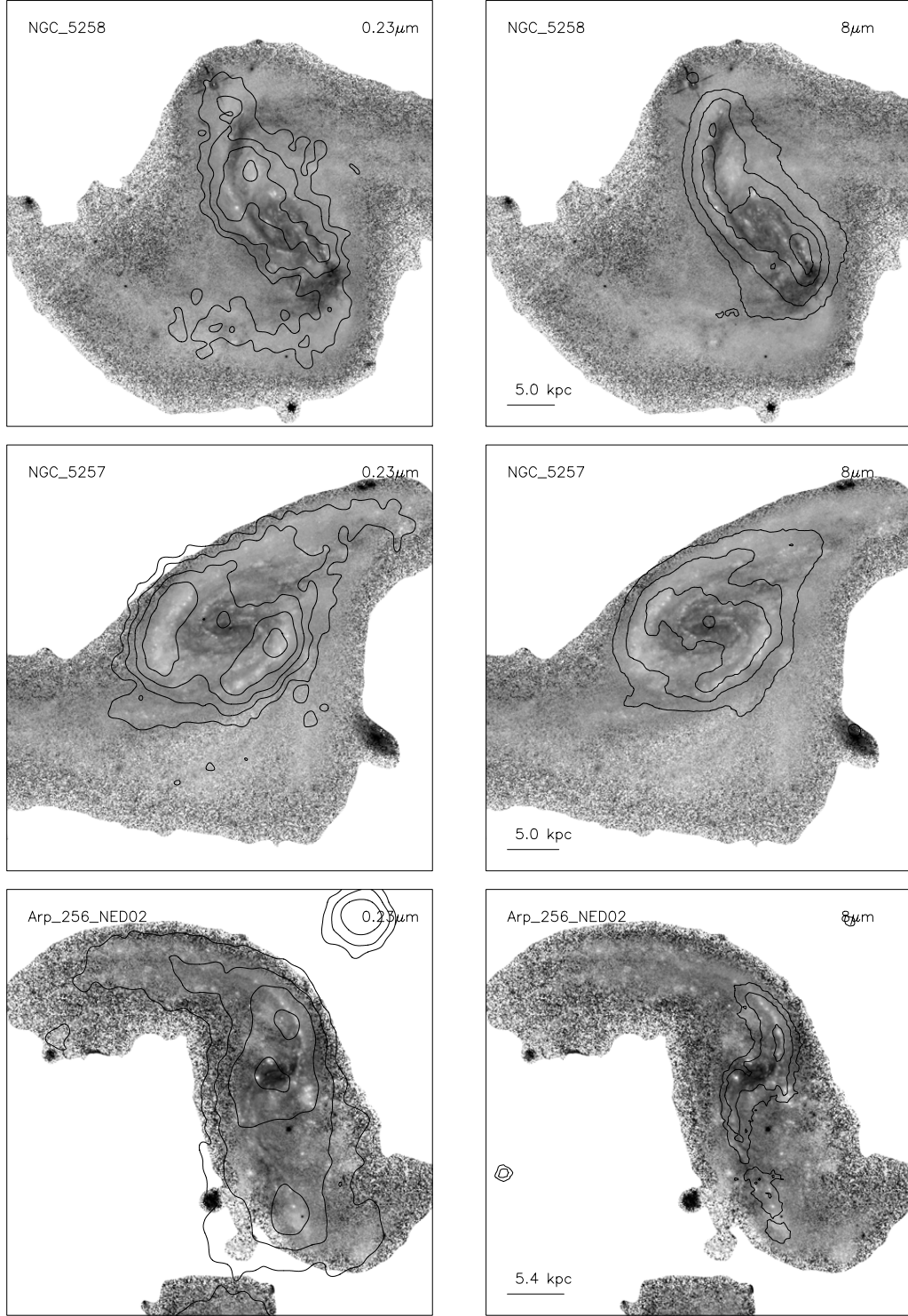


Figure 26: *GALEX* NUV 0.23 μm contours (left column) and *Spitzer* IRAC 8 μm contours superposed on grey-scale (F435W–F814W) host galaxy images III.

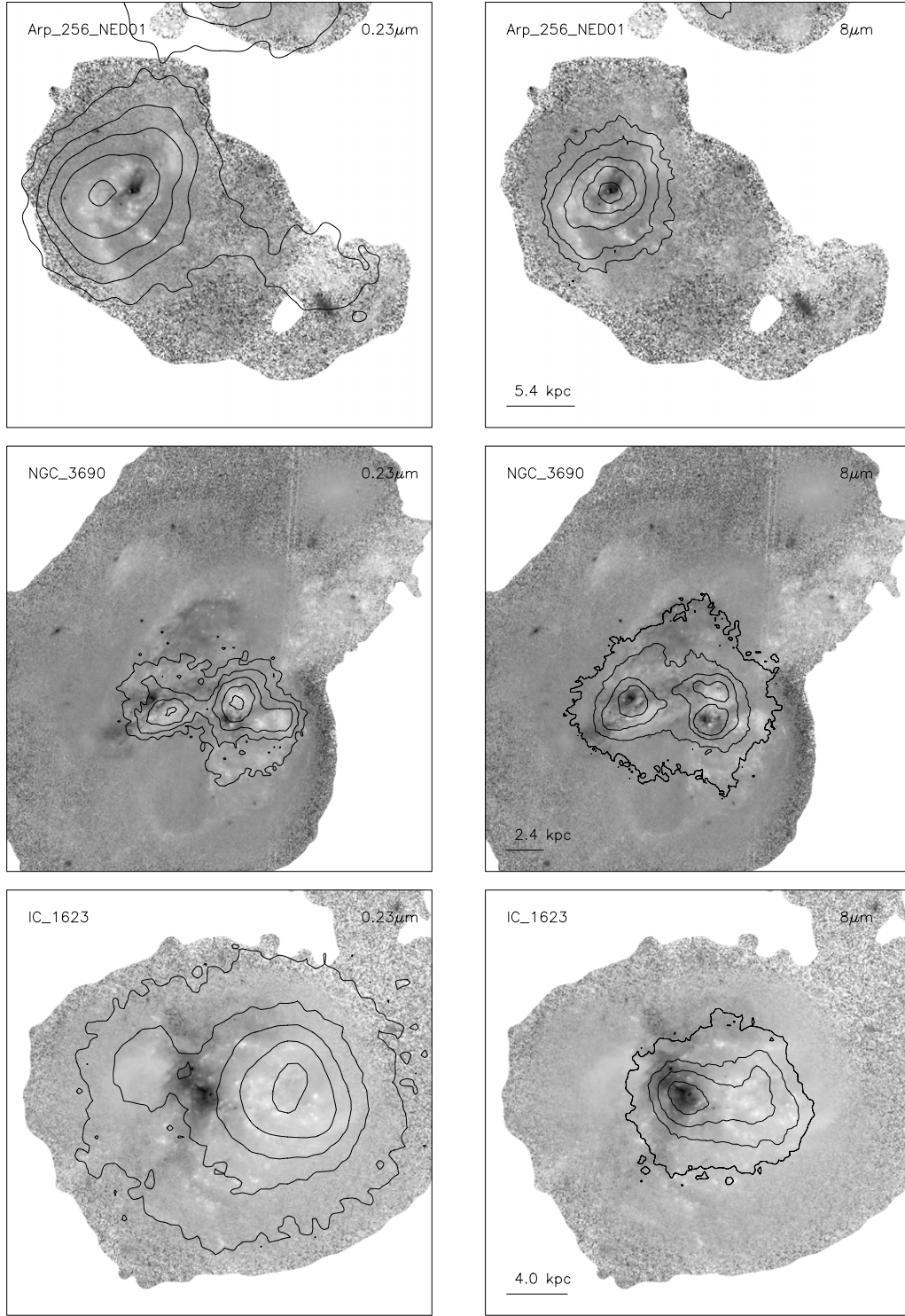


Figure 26: *GALEX* NUV $0.23\mu\text{m}$ contours (left column) and *Spitzer* IRAC $8\mu\text{m}$ contours superposed on grey-scale (F435W–F814W) host galaxy images IV.

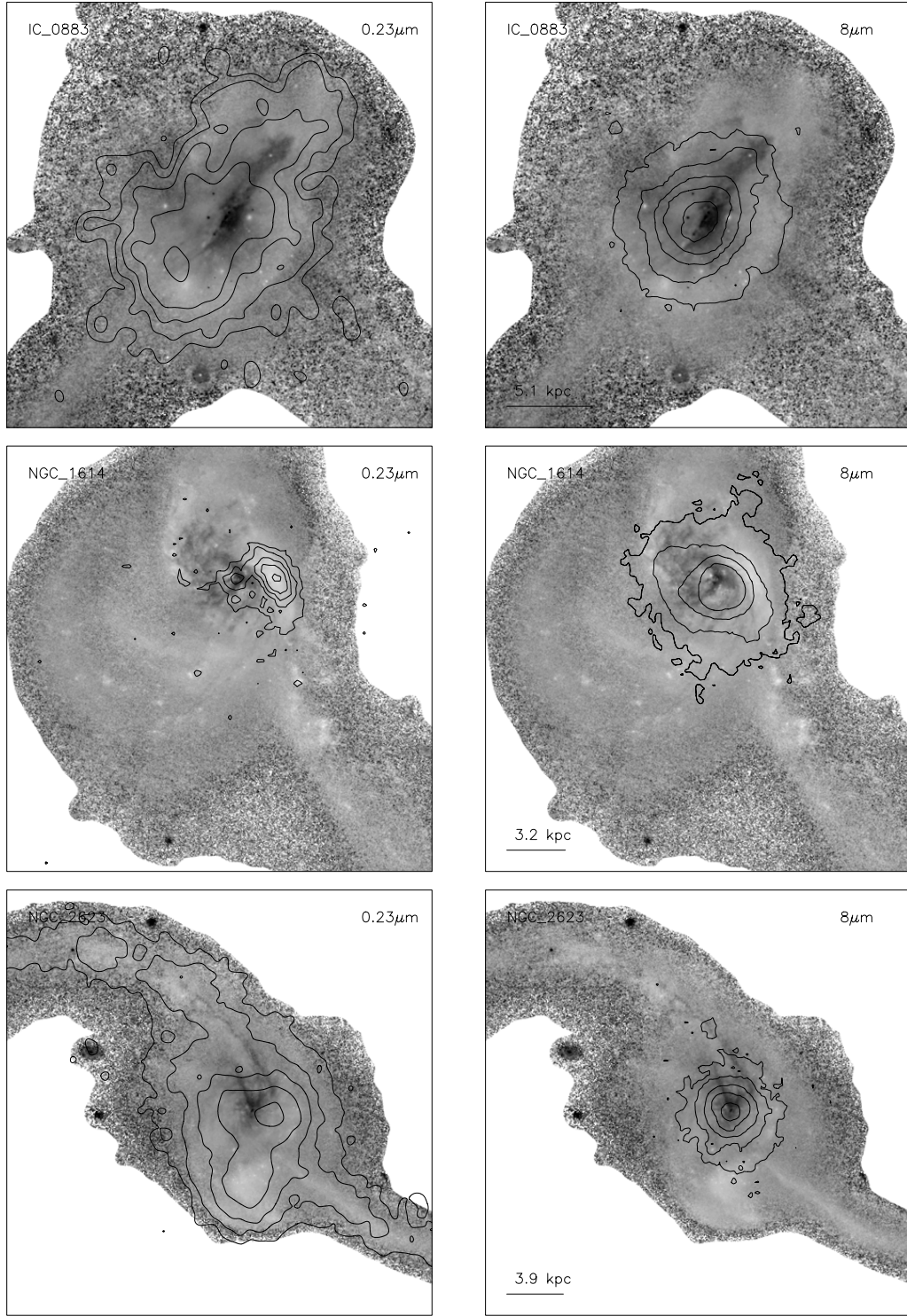


Figure 26: *GALEX* NUV 0.23 μ m contours (left column) and *Spitzer* IRAC 8 μ m contours superposed on grey-scale (F435W–F814W) host galaxy images V.

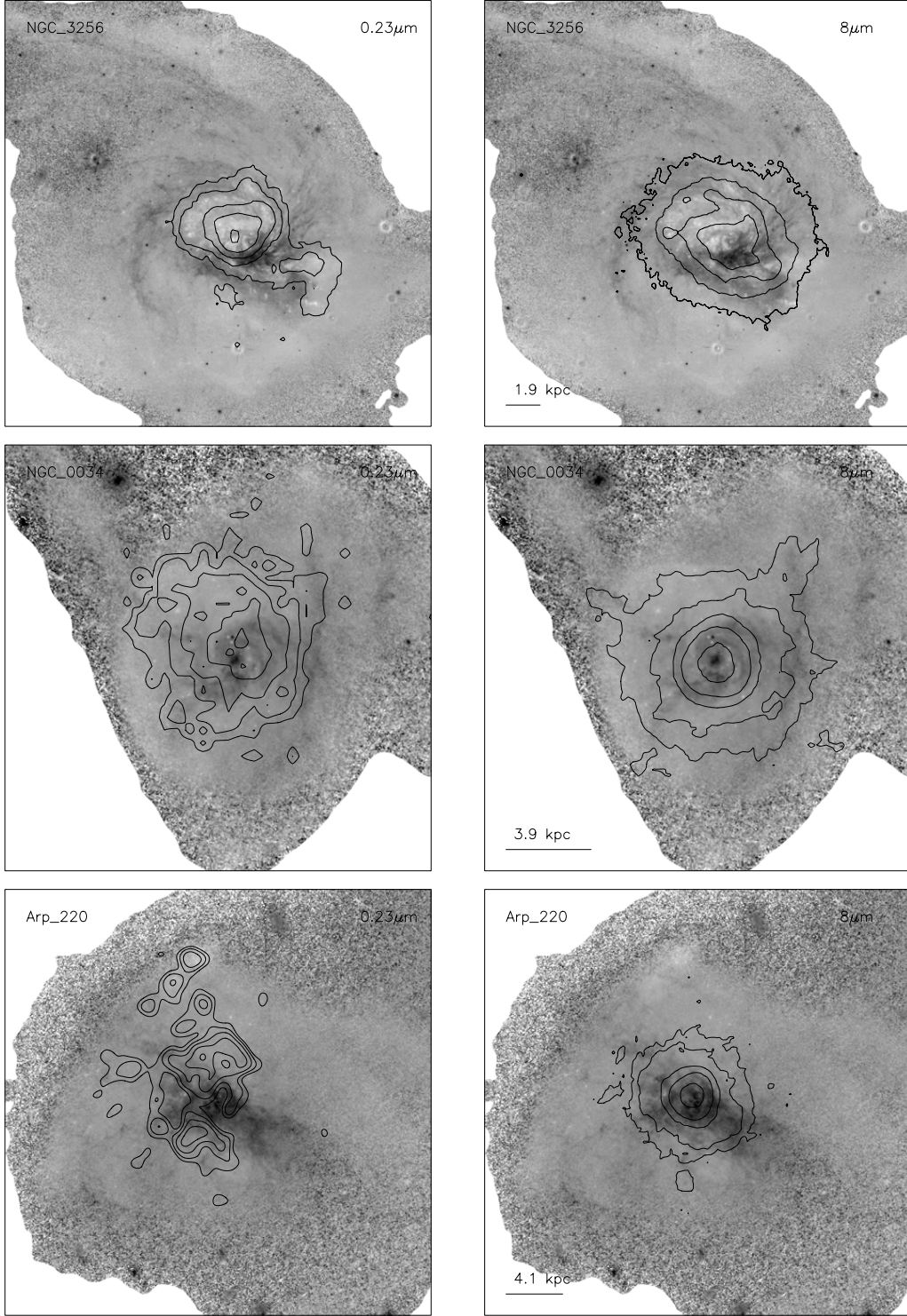


Figure 26: *GALEX* NUV 0.23 μ m contours (left column) and *Spitzer* IRAC 8 μ m contours superposed on grey-scale (F435W–F814W) host galaxy images VI.

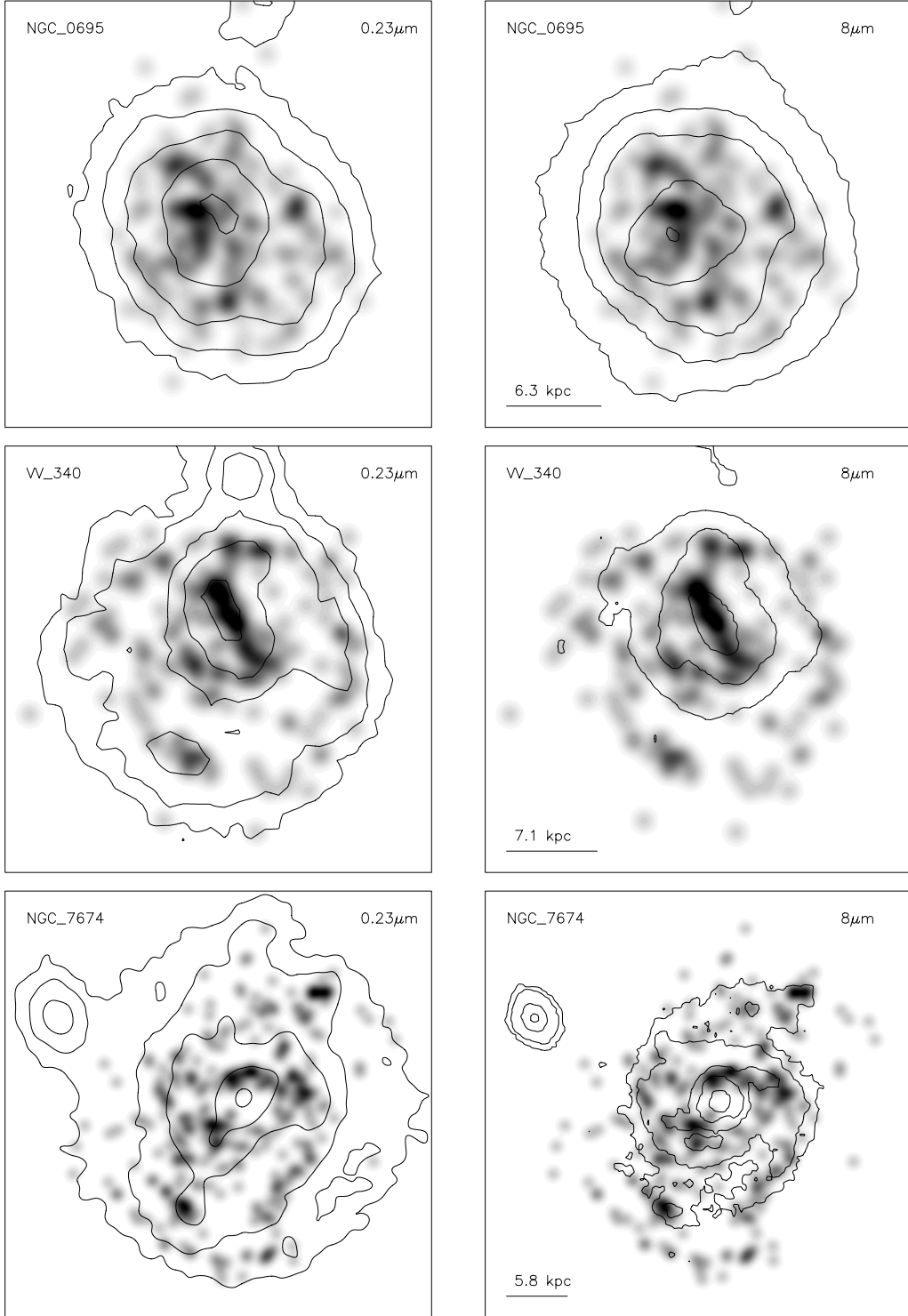


Figure 27: *GALEX* NUV 0.23 μm contours (left column) and *Spitzer* IRAC 8 μm contours superposed on grey-scale SC density maps I. Darker shades correspond to larger SC density values and lighter shades to smaller SC density values. The scale bar in the lower left corner corresponds to 10'' and the number above indicates the scale in kpc at the distance of the system. LIRGs are arranged in the merger sequence order.

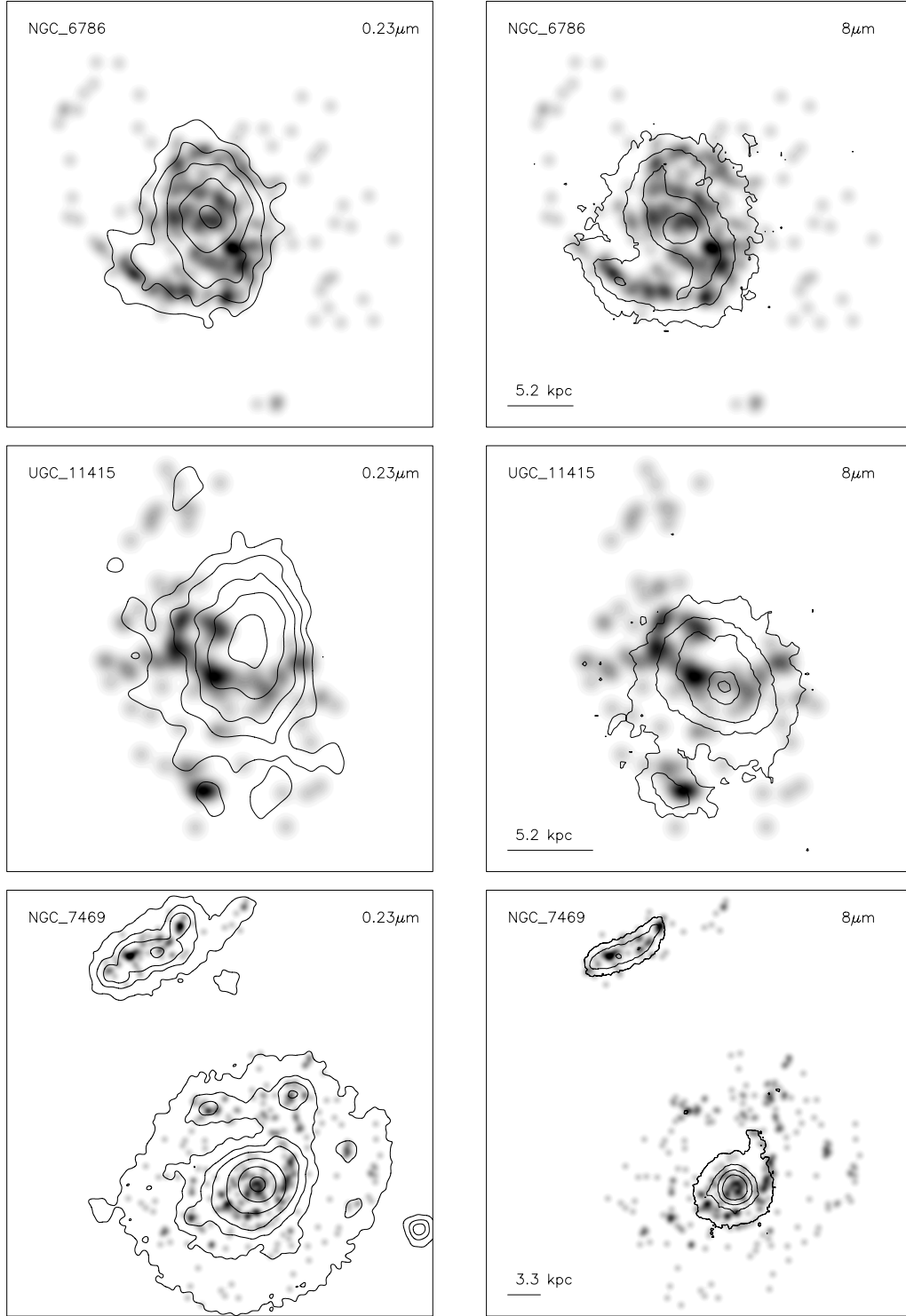


Figure 27: *GALEX* NUV 0.23 μ m contours (left column) and *Spitzer* IRAC 8 μ m contours superposed on grey-scale SC density maps II.

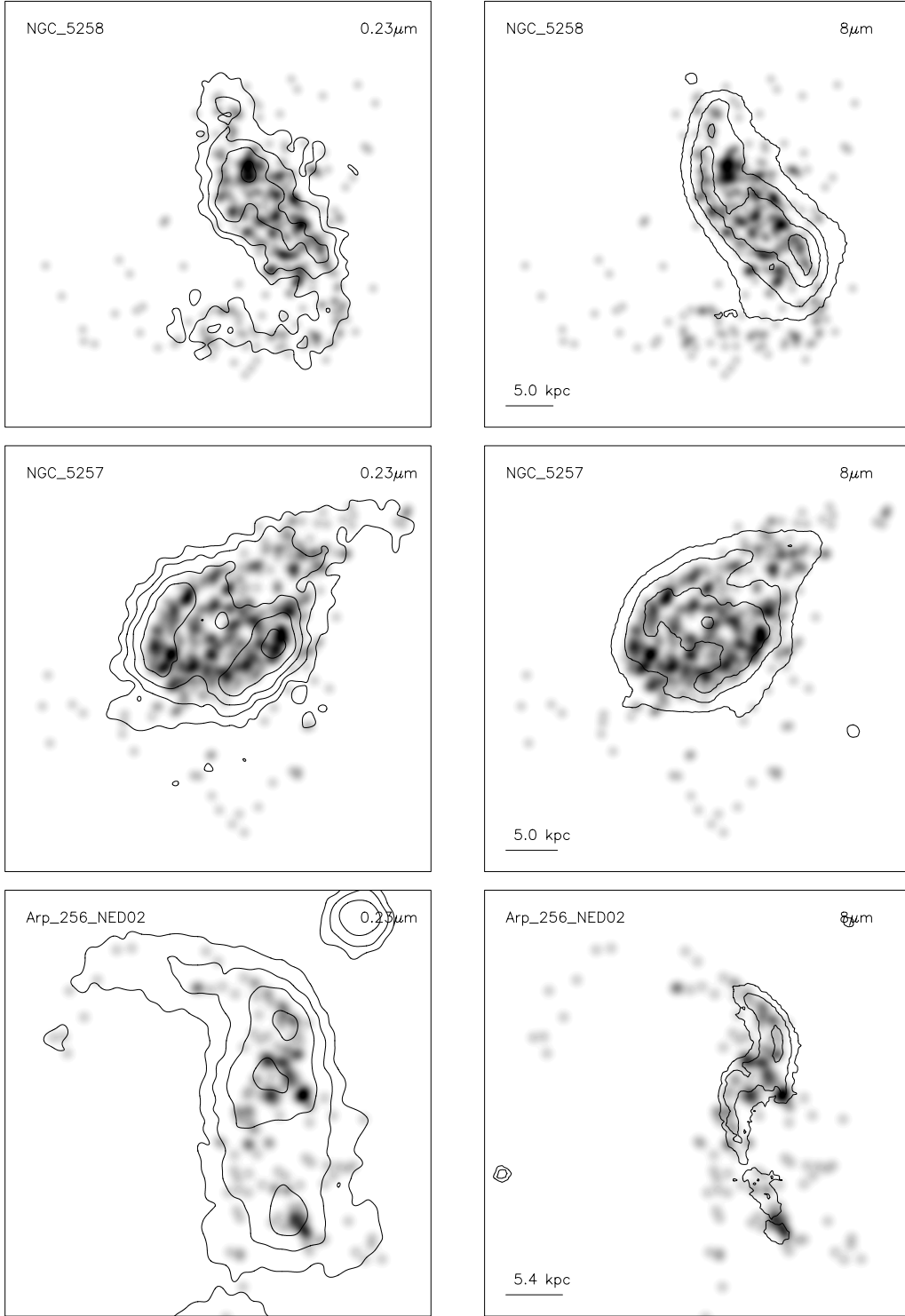


Figure 27: *GALEX* NUV $0.23\mu\text{m}$ contours (left column) and *Spitzer* IRAC $8\mu\text{m}$ contours superposed on grey-scale SC density maps III.

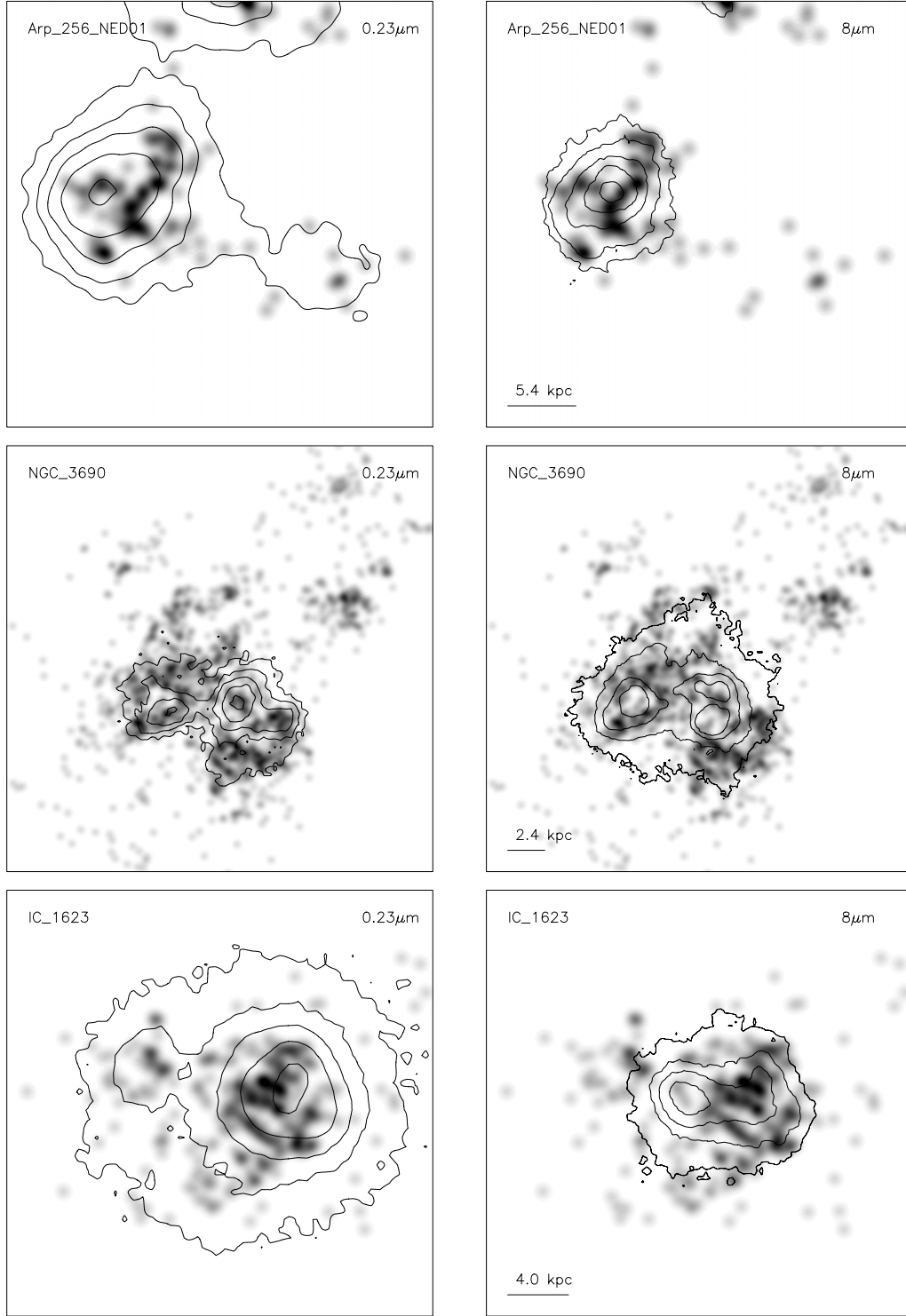


Figure 27: *GALEX* NUV 0.23 μ m contours (left column) and *Spitzer* IRAC 8 μ m contours superposed on grey-scale SC density maps IV.

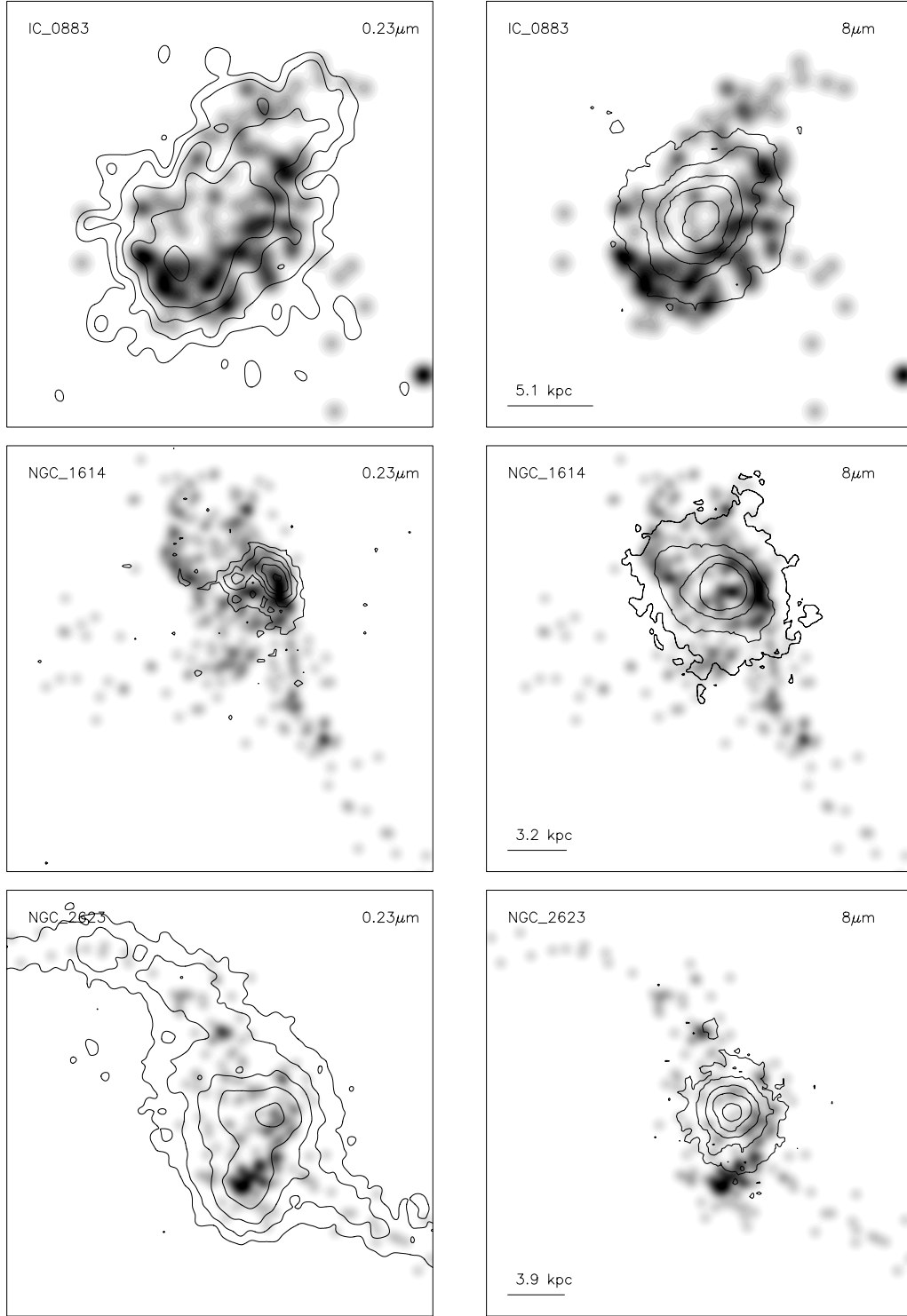


Figure 27: *GALEX* NUV 0.23 μ m contours (left column) and *Spitzer* IRAC 8 μ m contours superposed on grey-scale SC density maps V.

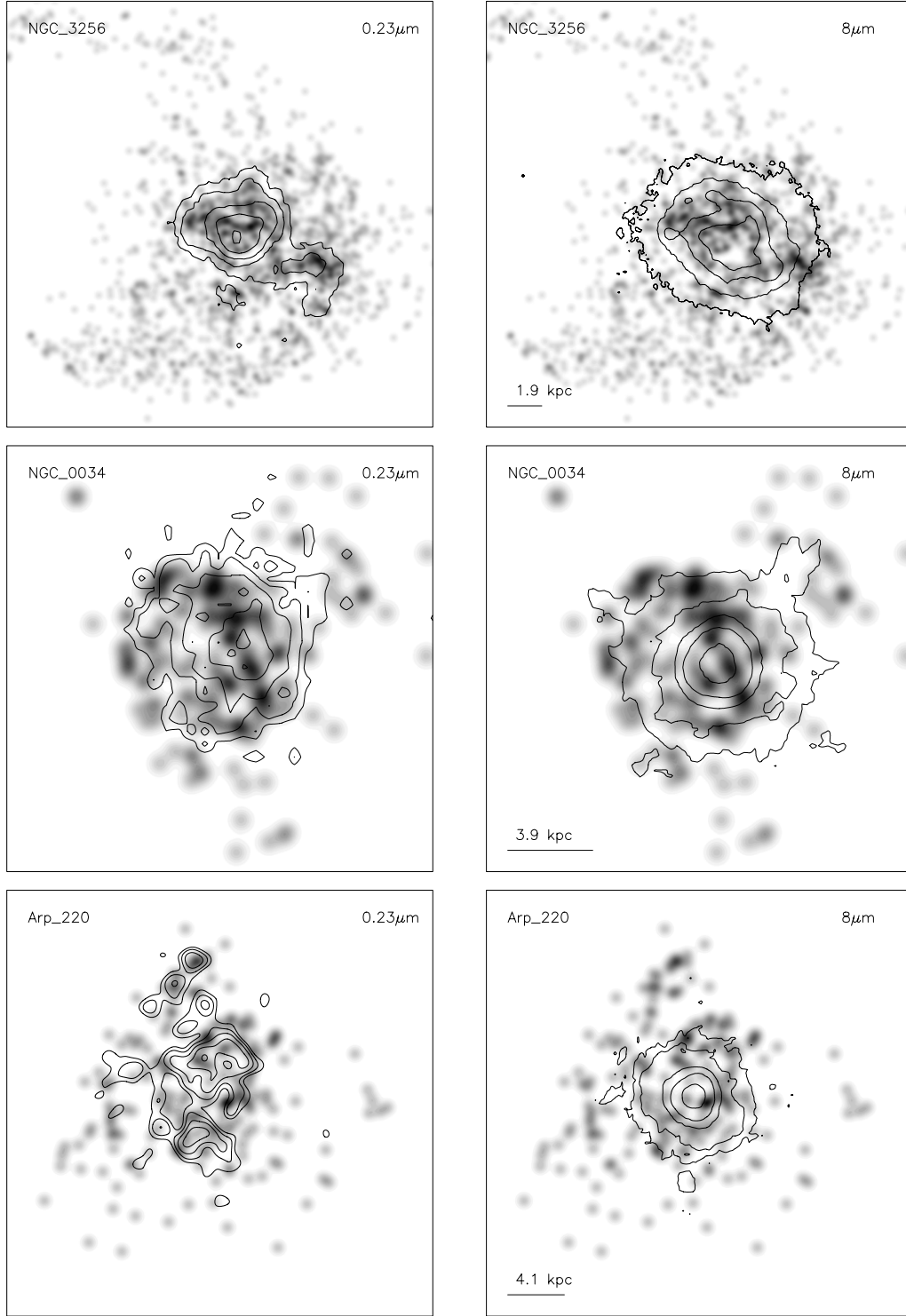


Figure 27: *GALEX* NUV 0.23 μ m contours (left column) and *Spitzer* IRAC 8 μ m contours superposed on grey-scale SC density maps VI.

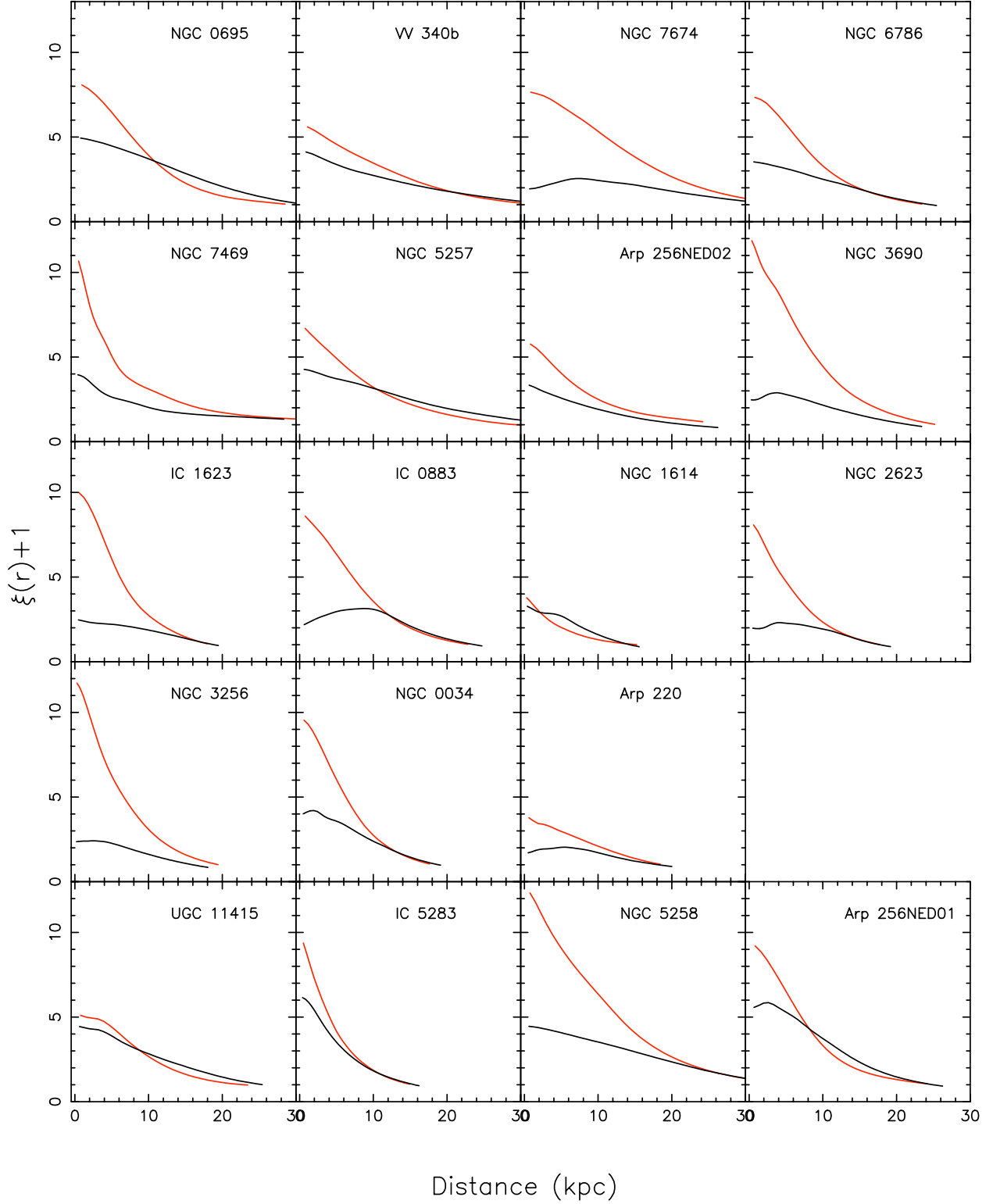


Figure 28: Cross-correlation functions of SC locations with *Spitzer* IRAC 8 μ m (black) and *GALEX* 0.23 μ m (red) fluxes. The bottom row shows the four galaxies that are members of galaxy pairs and have fewer detected clusters.